The Rapidly Oscillating Ap Star HR 1217

The Effect of a Magnetic Field on Pulsation

by

Christopher J. Cameron

B.Sc., Saint Mary's University, 2001

A THESIS SUBMITTED IN PARTIAL FULFILMENT OF
THE REQUIREMENTS FOR THE DEGREE OF

MASTER OF SCIENCE

in

THE FACULTY OF GRADUATE STUDIES

(Department of Physics and Astronomy)

We accept this thesis as conforming
to the required standard

THE UNIVERSITY OF BRITISH COLUMBIA

April 1, 2004

Library Authorization

In presenting this thesis in partial fulfillment of the requirements for an advanced degree at the University of British Columbia, I agree that the Library shall make it freely available for reference and study. I further agree that permission for extensive copying of this thesis for scholarly purposes may be granted by the head of my department or by his or her representatives. It is understood that copying or publication of this thesis for financial gain shall not be allowed without my written permission.

Christopher J. Cameron
Name of Author *(please print)*

21/04/2004
Date (dd/mm/yyyy)

Title of Thesis: The Oscillating Ap Star HR1217 : The Effect of a Magnetic Field on Pulsation

Degree: Master of Science Year: 2004

Department of Physics and Astronomy
The University of British Columbia
Vancouver, BC Canada

Abstract

The rapidly oscillating Ap (roAp) stars provide a unique opportunity to observe and test processes that until recently could only be studied in detail for the Sun. As a class, these stars possess extreme examples of chemical inhomogeneities through the effects of gravitational settling, mixing and radiative accelerations; magnetic fields that affect both the micro- and macroscopic physics that influence stellar structure; and high overtone pulsations. For the latter, we may use the tools developed for *asteroseismic* analysis: the inference of the internal structural properties of a star based on information from its pulsational instabilities.

One of the most studied of the roAp stars is HR 1217. The rapid variability of this star was first discovered by Kurtz (1982). Later, Kurtz et al. (1989) extended photometric observations of HR 1217 during a global campaign. They discovered six primary frequencies with periods near 6 minutes and a spacing pattern that is reminiscent of pulsations observed in the Sun.

This thesis presents a revised frequency analysis of photometric data on HR 1217 obtained during a Whole Earth Telescope (WET) campaign in late 2000. In particular, we identify a new frequency at 2788.94 μHz with a characteristic second-order p-mode spacing of 2.63 μHz from another frequency previously reported by Kurtz et al. (2002). Evolutionary and pulsational models of A stars are also presented with a discussion of how a magnetic field can perturb the acoustic frequencies. To accomplish this, the variational method used by Cunha & Gough (2000) is adapted to calculate magnetic perturbations to the acoustic modes calculated from our evolutionary models. These perturbations are used to explain the unexpected frequency spacing observed in HR 1217.

Contents

List of Tables

List of Figures

Acknowledgements

I'd like to begin by thanking my supervisor Jaymie Matthews. Over the past few years he has exposed me to many exciting scientific and educational opportunities. Of course there were other non-scientific; but equally educational, experiences as well. His guidance and patience has made this work possible. Thanks Jaymie. Many Thanks to Margarida Cunha for helping me understand some of the finer points of stellar pulsation theory and for being the second reader of this thesis. I don't think I've ever seen so many exclamation marks used in comments before. Thanks Margarida! I would also like to thank David Guenther for the use of his stellar evolution and pulsation software and for continuing to encourage and show interest in my work. To Don Kurtz, thank you for your comments throughout this work.

I would like to thank Steve Kawaler and Reed Riddle for helping me get acquainted with QED and to The Whole Earth Telescope collaboration for collecting, and giving me access to, such great data. Also, thanks to Gerald Handler for his comments on my earlier data reduction.

Special thanks to Mom, Dad, Cheryl, and Jennifer. Without you none of this would have been possible. Your support over the years has helped me in both my personal and academic life. Thank you.

I'd like to thank my friends at home and at UBC for helping make this process a fun one. Finally, I can't overlook Dr. Mark P.F. Huber for listening to my rants over the last year and for handing in this thesis while I was away.

Chapter 1

Introduction

1.1 Ap Stars and Chemical Abundances

In the Ap [1] nomenclature, the A represents the spectral class and the p stands for spectroscopically peculiar. The A classification can be somewhat misleading since the group also includes spectral types ranging from late B to early F with a temperature range of $14000 \gtrsim T_{eff} \gtrsim 7000\ K$. Peculiarities in these stars are observed as spectral line strength anomalies that are significantly different from the majority of other stars and are interpreted as abundance enhancements or depletions on the surface of the star.

Near the main sequence there exists a variety of chemically peculiar stars. Each group is defined by a specific temperature range, magnetic field strength, spectral line anomalies, and their pulsational properties. As an example, the hotter Ap stars with temperatures in the range of 10000 - 14000 K, can exhibit either Si or Hg and Mn peculiarities in their spectra. The difference here is the Ap Si stars exhibit a magnetic field while the Ap HgMn stars generally do not.

We can divide the Ap stars in two general categories based on their temperature and the observed abundances. The cooler stars with $T_{eff} \lesssim 10000\ K$ are classified as Ap SrCrEu stars and show very strong line strengths for the rare earth elements[2] Sr, Cr, and Eu. In addition, these stars generally have weak O lines. The hotter Ap stars with

[1] An alternate classification scheme for these stars is provided by Preston (1974). Under this scheme, the Ap stars discussed above are classified as CP2: magnetic Ap and Bp stars; including the He weak and He strong stars. In this thesis I will use the Ap nomenclature because it is more widely used in North America and because the nomenclature for the variable stars follow that of the Ap classification.

[2] elements La to Er

$T_{eff} \gtrsim 10000\ K$ show strong Si lines and are known as Ap Si stars. These stars sometimes show strong Ca lines as well as some enhancement in the lines of the iron peak elements[3]. Both hot and cool Ap stars seem to have weak He lines, if they are present at all. As a comparison, these peculiar line strengths correspond to photospheric overabundances up to 10^5 times the solar value and under abundances down to 10^{-2} times solar value. An overview of the Ap class of stars is provided by Wolff (1983) and Kurtz & Martinez (2000).

1.2 Magnetic Fields and the Ap Stars

Of the stars located near the upper main sequence, magnetic fields are measured only in the chemically peculiar ones. In the case of the Ap stars, the fields appear to be global and predominately dipolar with strengths that range from approximately 0.3 kG to 30 kG (Landstreet, 1992a). These magnetic fields seem to be intricately connected to the chemical peculiarities and the variability of these stars; both of which will be discussed later in this chapter. A general discussion of magnetic fields in stars is given by Mathys (1989) and Landstreet (1992a; 1992b; and 1993).

1.2.1 Ap Spectra and the Zeeman Effect

The perturbations to stellar spectra produced by line transitions of an atom in the presence of a magnetic field are described by the Zeeman effect. If an atom is not in the presence of a magnetic field there exists a set of discrete energy transitions that can occur as electrons change their energy levels. There is also coupling between an electron's spin and orbital angular momentum; known as LS coupling, that add to give rise to a larger number of possible energy states available to the electron. If the total angular momentum from the LS coupling is represented by J, then in the presence of a magnetic field there becomes $2J + 1$ available states for the electron. Each of these magnetic substates are

[3]elements Sc to Ni

represented by the integer quantum number m.

If the difference in magnetic substates is $\Delta m = 0$, then they are referred to as π components. If $\Delta m = \pm 1$, then the substates are known as σ components. The π component is symmetrically spread around the unperturbed wavelength, while the σ components have wavelengths that are on either side of the unperturbed wavelength. The spacing of the σ components is proportional to the magnetic field strength for fields with strengths up to a few tens of *kiloGauss*. The relation between the spacing of the π and σ components is given by (cf. Landstreet 1992b)

$$\Delta\lambda = \lambda^2 eB/4\pi mc^2 \tag{1.1}$$

where λ is the unsplit wavelength, B is the magnetic field, and e/m and c are the charge-to-mass ratio of the electron and the speed of light, respectively. This relation assumes that the Landé factor; calculated from the spin quantum numbers, is equal to one.

Even if the Zeeman components of a line are not fully resolved, as is almost always the case, the π and σ components tend to broaden the spectral line. If this broadening can be measured the effective field strength may be estimated. However, there are other effects that compete to broaden a spectral line such as thermal and Doppler broadening and micro- and macroscopic turbulence. The Zeeman broadening dominates for a small subset of stars with $B \gtrsim 10$ kG and projected velocities $v \sin(i) \lesssim 10$ km/s (Landstreet, 1992b).

1.2.2 Some Observable Magnetic Quantities

The sensitivity to the magnetic field varies from line to line. By observing lines from different elements, one can deduce the magnetic field strength by comparing the widths of these lines to each other. In this way, the Zeeman components can provide a measure of the magnetic field strength integrated over the stellar disc. This quantity is known as the mean field modulus and may be denoted as $< B >$. For example, Mathys et al. (1997) present measures of the magnetic field modulus for 40 Ap stars.

The spectral lines influenced by a magnetic field also possess interesting polarization properties. Information gained form the polarization of spectral lines can further be used to set limits on magnetic field geometry. If a spectral line is observed in both left and right-circularly polarized (LCP and RCP respectively) light, the contribution to the spectral line from each of the σ components is different. The difference in the position of the mean wavelength of the line in RCP and LCP light provides a measurement of the line-of-sight component of the magnetic field averaged over the stellar disc. This measurement is known as the mean longitudinal field strength and is represented by B_l. For most Ap stars, B_l and its variation with rotation of the star are the only magnetic observations available because they are relatively easy to obtain (Landstreet, 1993). This is because the measurement is most sensitive to modest fields with simple structures and no *a priori* information about the line profile is needed. In fact, the variation in B_l with rotation phase ϕ is periodic and is given by the simple analytic expression

$$B_l(\phi) \approx 0.4 B_p \left(\cos\beta\cos i + \sin\beta\sin i\cos\phi\right) \tag{1.2}$$

where B_p is the polar field strength; assumed to be a centred dipole, i is the angle between the rotation axis and the line of sight, and the magnetic pole is inclined to the rotation axis of the star by the angle β.

This expression may be derived from oblique rotator model of Stibbs (1950) and assumes a limb darkening coefficient of unity. The geometry of the oblique rotator is shown in Figure 1.1. As the star rotates, the angle from the magnetic field pole to the line of sight changes. Thus, the change in the aspect of the magnetic field leads to a modulation of B_l with the rotation of the star. If there is a strong field ($\gtrsim 1$ kG) we may also obtain information about its geometry from the transverse field component. The π component of a Zeeman triplet will usually saturate before the σ components. The integrated line profile will then leave a net linear polarization (e.g., Leroy et al., 1993). From this net linear polarization one can, in some cases, obtain unique values for i, β and B_p defined in Equation 1.2. This characteristic of the Zeeman components is known as broadband linear polarization.

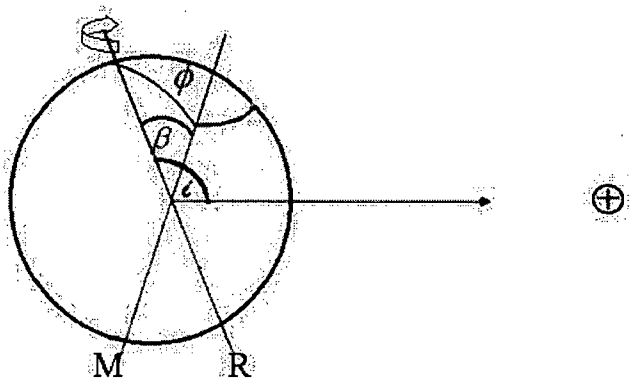

Figure 1.1: A schematic diagram showing the oblique rotator model geometry. The rotation axis and dipole magnetic axis are labeled R and M respectively. The line of sight to Earth is toward the right. Angles ϕ, β and i are defined in Section 1.2.2.

There are other techniques for extracting magnetic field information from spectra. The moment technique, for example, fits spectral lines measured with different polarizations (i.e., different Stokes parameters) with line moments defined by $(\lambda - \lambda_0)^{n+1}$. Here, λ and λ_0 are the integral over the line profile and the centroid of the wavelength respectively (see Mathys 1989). The moments of different Stokes parameters yield information about the field geometry. For instance, the first moment of the difference between the intensity in LCP and RCP (Stokes V) light recovers the mean longitudinal field (Mathys, 1988).

1.3 Diffusion in Ap Stars

In the context of Ap stars, the separation of elements as a means to explain the observed abundance patches was first studied as early as the late 1960s and early 1970s (e.g., Michaud, 1970). In principle, any element that is heavier than the surrounding (mainly Hydrogen) mixture will sink under the influence of gravity. Exceptions occur for elements that have absorption lines at the wavelengths near the local flux maximum. In these cases, the elements may be levitated upward toward the stellar surface if the radiative forces are greater than the gravitational force. Once the elements reach an equilibrium position between gravitational and radiative forces they may accumulate in sufficient amounts and cause abundance anomalies at these locations. Rare Earth elements, such as Sr, may accumulate at the surface of Ap stars in this way. General reviews of diffusion theory may be found in Vauclair & Vauclair (1982) and Michaud & Proffitt (1993).

The process of element separation described above is, however, a fragile one. If there are turbulent or convective velocities in the upper atmospheres of these stars that exceed the diffusion velocities of a few cm/s, the abundance anomalies will simply be mixed away (Michaud, 1976). While the main sequence A stars do not have large convective zones, the A giants do. This explains why the A-type giants loose their abundance peculiarities.

It should also be noted that diffusion time scales are on the order of $\approx 10^6$ yrs; a small fraction of the evolutionary timescale of a near solar-mass star. Thus, chemical separation may occur early in the evolution of these stars. Diffusion theory predicts a the thin layer of abundance anomalies at the surface of these stars. As noted by Kurtz & Martinez (2000), if the observed abundances of the rare Earth elements in Ap stars (over abundances of $\approx 10^4$ solar values) were representative of the interior metal content of these stars, they would contain nearly all of these elements in the Universe. Since Ap stars represent approximately one in a hundred thousand stars, this can't possibly be the case.

In order for the diffusion mechanism in these stars to be efficient, there must be a stabilizing mechanism against turbulence as discussed above. It is believed that the

magnetic field provides this stabilizing mechanism for these stars. It also has the added effect of causing horizontally distributed abundances on the stellar surface near regions of horizontal magnetic field (Michaud et al., 1981). This occurs when ions of an element are levitated to depths where the magnetic field becomes important compared to the radiative and gravitational forces. These ions are then distributed both vertically and horizontally at the stellar surface.

Magnetic fields can de-saturate some lines of an element through the Zeeman effect. This results from the Zeeman split lines being excited at slightly different frequencies than the same lines produced when no magnetic field is present. When a magnetic field is induced, these lines will no longer have the optimal widths and energies for radiative forces to overcome gravity. Therefore, some elements will become less susceptible to radiative accelerations when there are magnetic influences. The polarization of the Zeeman components also affects the horizontal acceleration of elements; adding to the distribution of elements observed for the Ap stars (Babel & Michaud, 1991, and Michaud, 1996).

1.4 Stellar Seismology and the Ap Stars

Rapid variability [4] of star light was first observed in the Sun. Leighton et al. (1962) found that spatially incoherent wave patterns exist on the surface of the Sun with periods near 5 minutes. Ulrich (1970), Leibacher & Stein (1971) were the first to interpret these oscillations as sound waves produced in the solar interior that resonate in acoustic cavities generated by changes in the local sound speed. These sound waves produce standing wave patterns as they propagate around the interior of the sun within these acoustic cavities.

Since these early beginnings, millions of p-modes have been observed in the Sun. The name $p-mode$ comes from the fact that pressure is the restoring force for the sound waves that are responsible for the observed oscillations. These p-modes have proved to be a powerful tool for studying the internal properties of the Sun through *helioseismology*.

[4] The term rapid is in comparison to other *classic* pulsators, such as Cepheid Variables, that can have oscillation periods of months.

The field of helioseismology is akin to studying internal properties of the Earth using seismology. A few examples of successful inferences on the solar interior made from helioseismology include an estimate of the internal rotation rate, the depth of the solar convective zone, constraints on element diffusion, and the run of sound speed. A recent review of helioseismology is provided by Christensen-Dalsgaard (2002).

Until the late 1970s, observations of stars had not shown p-modes with periods and frequency spacing similar to those observed in the Sun. This changed when Kurtz (1978, 1982) discovered the rapidly oscillating Ap stars. These stars exhibit rapid variability in their light curves with periods between 5 and 15 minutes and semi-amplitudes under approximately 8 *milli*magnitudes through a Johnson B filter. To date, there are 32 known roAp stars: Kurtz & Martinez (2000) report 31 and the most recent, HD 12098, is reported by Girish et al. (2001). Some of these stars are multi-periodic and exhibit frequency patterns similar to those observed in the Sun. The best example of this is the *star* of this thesis, HR 1217 (see Section 1.5). Some detailed reviews of roAp stars are provided by Kurtz (1990), Matthews (1991) and Kurtz & Martinez (2000).

In general, the Ap stars show three types of variability. These include spectral line strength, magnetic field strength, and photometric (integrated light) variations. The photometric variations can further be sub-divided into long-term (LT) variations and rapid oscillations (the roAp stars). Each of these forms of variability seem to be interconnected through the complex geometry of the magnetic field, abundance patterns, stellar rotation and inclination of the star to the observer. I will begin with a discussion of nonradial oscillations and their relevance to the roAp stars. The connection between the magnetic, spectral, LT and rapid variations and the geometry that links them will then be discussed.

1.4.1 Nonradial Oscillations

Nonradial oscillations are discussed in detail by Unno et al. (1989). A brief introduction to areas of particular relevance to the roAp stars is presented below.

To first order, a slowly rotating, non-magnetic star is spherically symmetric. Perturbations to this spherical symmetry can be described by spherical harmonics, $Y_l^m(\theta, \phi)$. Here θ and ϕ are the usual angular coordinates of the spherical coordinate system. The study of oscillations in stars can be described as small perturbations to physical variables within the star such as pressure or density or in radial displacements ξ_r. In general, we may expand radial displacements in terms of spherical harmonics as

$$\xi_r = \sum_{n,\ell,m} \xi_{r,n\ell}(r) Y_l^m(\theta, \phi) exp(i\sigma_{n\ell} t) \tag{1.3}$$

where the n is the radial order of the oscillations and corresponds to the number of radial nodes (zeroes) in the eigenfunction $\xi_{r,n\ell}$, $\sigma_{n\ell}$ is the eigenfrequency of the oscillations, and t is time.

The spherical harmonic provides the angular description of the modes through the indices ℓ and m. The index ℓ is commonly called the degree of the mode and divides the surface into regions oscillating in opposite phase. If $\ell = 0$, the oscillation mode is radial; or more precisely, spherically symmetric. The index m is the azimuthal order of the mode and represents the number of longitudinal nodes on a sphere. Physically, the order m can be related to the phase velocity of a wave through

$$\left(\frac{\partial \phi}{\partial t}\right)_{phase} = -\frac{\sigma}{m} \tag{1.4}$$

The sign of m indicates the direction in which the wave travels. A standing wave in the longitudinal direction can be formed by the superposition of two waves traveling in opposite directions since the background state is, to first order, spherically symmetric.

In terms of quantization of the indices, m may take integer values from $-\ell$ to $+\ell$ and ℓ is a nonnegative integer. If $m = 0$ all nodal lines on a sphere are lines of latitude, while if $m = \ell$, they are all lines of longitude. These are known as zonal and sectoral modes respectively. If m takes on values between these extremes, the modes are known as tesseral modes and of the ℓ nodal lines, $\ell - |m|$ of which are lines of latitude. Examples are drawn schematically[5] in Figure 1.2 for the cases $\ell = 3$ and $m = 0$ to 3. Note that

[5]Image taken from the Delta Scuti Network homepage: http://www.deltascuti.net/DeltaScutiWeb/index1.html

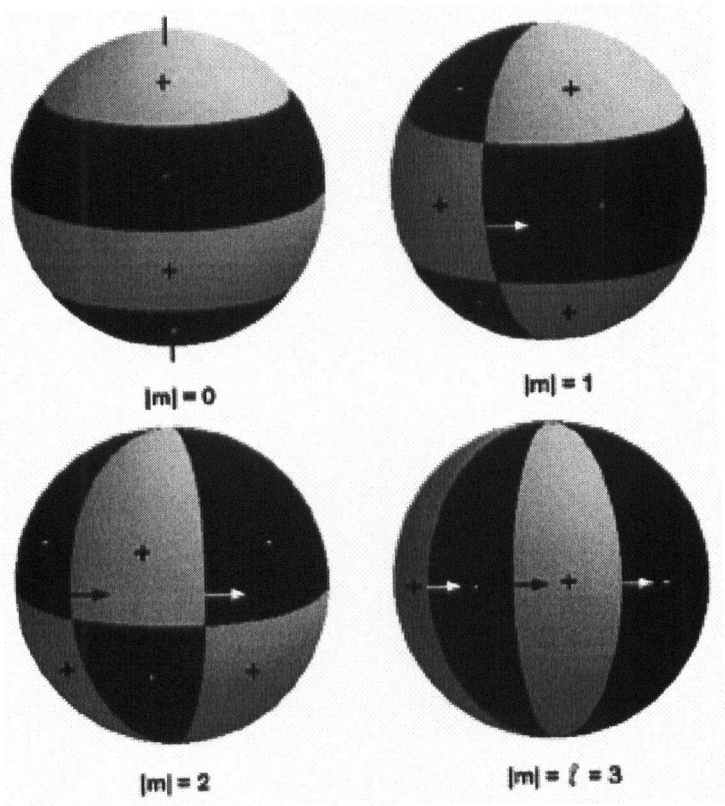

Figure 1.2: A schematic representation of different spherical harmonic modes. At the top left $\ell = 3$ and $m = 0$ and at the lower right $\ell = 3$ and $m = 3$. The top right and lower left modes represent $\ell = 3$ and $m = 1$ and 2, respectively. The blue (-) and yellow (+) represent regions that oscillate opposite in phase. Note there are $\ell - |m|$ lines of latitude. This image was taken from the Delta Scuti Network homepage.

both $\xi_{r,n\ell}$ and $\sigma_{n\ell}$ in Equation 1.3 are independent of m. This results in a degeneracy that may be lifted due to perturbations from slow rotation or magnetic field. For example slow, uniform, rotation causes frequencies to split according to the equation

$$\sigma^{rot}_{n,\ell,m} = -m\,(1 - C_{n,\ell})\,\Omega \tag{1.5}$$

where Ω is the angular rotation frequency of the star measured in the rotating frame

and $C_{n,\ell}$ is known as the Ledoux constant (Ledoux, 1951). The Ledoux constant is model dependent and is of the order $1/\xi_r$. Now each frequency may be described in an inertial reference frame by the unperturbed frequency σ from Equation 1.3 plus $\sigma^{rot}_{n,\ell,m}$ from Equation 1.5.

In the case of the roAp stars, the strong magnetic field produces pressures that are greater than the local gas pressure near the stellar surface. A traditional perturbation approach in describing the effect of a magnetic field on a pulsation mode is no longer valid. Individual oscillation modes cannot be described by a single set of n, ℓ, and m values. Instead, each mode must be expanded in an infinite sum of spherical harmonics to account for the coupling between the magnetic field and pulsation geometry (e.g., Dziembowski & Goode, 1996, Bigot et al., 2000, and Cunha & Gough, 2000). The effects of the strong magnetic field on the *normal* modes (i.e., those calculated in the case of no magnetic field or rotation) will be discussed in Section 3.3 in terms of a variational approach used by Cunha & Gough (2000).

1.4.2 High-Overtone Pulsation and Frequency Spacing

Oscillation frequencies of a few *milli*Hertz[6] (mHz) are consistent with p-mode frequencies in non-degenerate stars described by large n values. Currently, photometric observations of pulsating stars yield only the contributions of ℓ modes with small values. This is because the contribution from modes with $\ell \gtrsim 3$ gets smoothed out when the light from a stellar disc is integrated. The high overtones of such low-degree pulsations have asymptotic behavior that may be exploited for stars like the roAp stars.

If a spherically symmetric star pulsates adiabatically with p-modes of $n \gg \ell$, we may use the asymptotic theory of Tassoul (1980, 1990) to describe the frequencies by

$$\nu_{n,\ell} \approx \Delta\nu\,(n + \ell/2 + \epsilon) + \Upsilon \tag{1.6}$$

where ϵ is a constant, and Υ is a structurally dependent quantity that is an order of magnitude smaller than the first term. It is convenient to introduce the frequency ν

[6] A period of 5 *minutes* corresponds to a frequency of 3.3 mHz

since it is usually found in the observational literature on pulsating stars. The relation between the angular frequency defined in equation 1.3 and that of Equation 1.6 is simply $\nu = \sigma/(2\pi)$.

The factor $\Delta\nu$ in Equation 1.6 will be used extensively in this thesis. It is related to the time it takes sound to cross the diameter of the star and is usually referred to as the large spacing. This frequency is written in terms of the sound speed c through

$$\Delta\nu = \left[2\int_0^R dr/c\right]^{-1} \tag{1.7}$$

where R is the radius of the star. Since this quantity is approximately related to the mean density of the star, it may be written in terms of the stellar mass M, and radius via the relation

$$\Delta\nu = (0.205 \pm 0.011)\left(\frac{GM}{R^3}\right)^{1/2} \text{ Hz} \tag{1.8}$$

where G is the gravitational constant. The numerical factor arises from model calculations performed by Gabriel et al. (1985). Matthews et al. (1999) rewrote Equation 1.8 in terms of the stars effective temperature T_{eff}, and luminosity L, to give

$$\Delta\nu = (6.64 \pm 0.36) \times 10^{-16} M^{1/2} T_{eff}^3 L^{-3/4} \text{ Hz} \tag{1.9}$$

with L and M in solar units and T_{eff} in degrees Kelvin.

It should be noted that there is an ambiguity in the interpretation of the observed frequency spacing depending on the ℓ values. If the modes have orders that differ from each other by one and ℓ values that alternate between even *and* odd values, Equation 1.6 yields a frequency spacing of approximately $\Delta\nu/2$. If however, consecutive ℓ values are either all even *or* odd, the frequencies will be spaced by about $\Delta\nu$; the large spacing.

There is also a second order spacing defined by $\delta^{(2)} = \nu(n,\ell) - \nu(n-1,\ell+2)$. By writing Υ from Equation 1.6 in terms of the sound speed, this spacing yields

$$\delta^{(2)} \propto \Delta\nu \int_0^R \frac{1}{r}\frac{dc}{dr}dr \tag{1.10}$$

The details leading to this equation may be found in the work of Tassoul (1990).

This spacing is referred to as the small spacing. Close to the center of a star, the leading contribution to Equation 1.10 comes from the $1/r$ factor in the integrand. Thus, this spacing may be used to infer properties of the interiors of stars (e.g., Provost, 1984, and Guenther & Demarque 1997). For the roAp stars, however, the diagnostic power of $\delta^{(2)}$ may be limited because the magnetic perturbations to the frequencies may be of the same order, or larger than, the small spacing (Dziembowski & Goode, 1996).

1.4.3 The Oblique Pulsator Model

The LT variability mentioned in Section 1.4 is shown for HR 1217 along with the variation of its magnetic field in Figure 1.3. It is clearly shown that the mean light variation of the star is in phase with the magnetic field. The modulation of the magnetic field is described well by the oblique *rotator* model of Stibbs (see Section 1.2.2). Kurtz (1982) suggested that the LT variability and rapid variations may be modulated in a similar way through what he called the oblique *pulsator* model. In this model, the pulsation axis of the star is aligned with the magnetic axis of the star; both of which are inclined to the rotation axis. As the star rotates the aspect of the pulsation and magnetic axis vary; leading to modulation with the rotation of the star. The geometry is the same as in Figure 1.1, but now the magnetic axis and pulsation axis are one in the same.

Consider an axisymmetric ($m = 0$) pulsation mode with frequency σ. Kurtz (1982) showed that in the geometry of the oblique pulsator, the luminosity variation with rotation may be expressed as

$$\frac{\Delta L}{L} \propto P_\ell^m(\cos\alpha)\ \cos\left[\sigma t + \varphi_p\right] \tag{1.11}$$

where P_ℓ^m is the associated Legendre polynomial, φ_p is an arbitrary phase, and the angle α is the varying angle between the magnetic field axis and the line of sight. This angle has the same functional dependence as in the oblique rotator model of Equation 1.2. In the case of a dipole mode ($\ell = 1$), the Legendre polynomial is equal to $\cos\alpha$ and Equation 1.11 may be expanded as

$$\frac{\Delta L}{L} \approx A_0 \cos\left(\sigma t + \varphi_p\right) + A_1 \left[\cos\left(\{\sigma + \Omega\}t + \varphi_p\right) + \cos\left(\{\sigma - \Omega\}t + \varphi_p\right)\right] \tag{1.12}$$

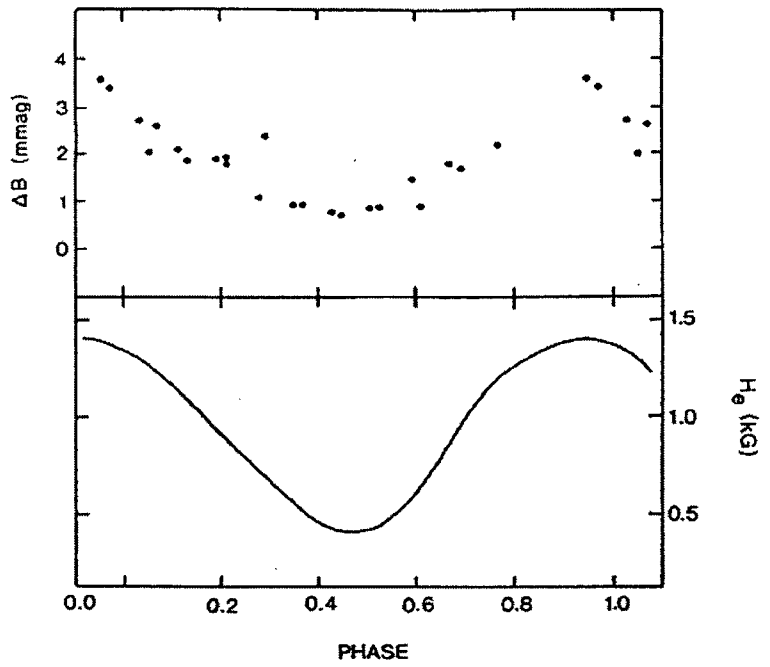

Figure 1.3: The variation in the mean light of HR 1217 through the B filter as a function of the rotation phase of the star (upper panel). The magnetic field variation defined by B_l in Section 1.2.2 as a function of rotation phase is shown in the lower panel. Pulsation data and magnetic field data were taken from Kurtz (1982) and Preston (1972) respectively. This figure was obtained from Matthews (1991).

The amplitudes are given by $A_0 = \cos i \cos \beta$ and $A_1 = (\sin i \sin \beta)/2$.

From the above relations, we see that a single dipole mode is split into a triplet exactly spaced by the rotation period of the star. In general, this model predicts that a mode with degree ℓ is split into $2\ell + 1$ frequencies. The roAp stars do exhibit such fine structure in their frequencies.

Frequencies may also be split by rotation through Equation 1.5. These frequencies are not exactly spaced by the rotation frequency of the star because of the Ledoux constant. Calculations of the Ledoux constant for A star models by Shibahashi & Takata (1993) suggest a value of $C_{n,\ell} \approx 10^{-3}$. A stringent observational constraint is provided by Kurtz et al. (1997) from the frequency spacing of the roAp star HR 3831. They place an upper limit of 10^{-6} on $C_{n,\ell}$ at the 3σ confidence level. The coincidence of magnetic and pulsation phase along with the above constraint are strong indications that the observed fine structure in the frequency spectrum of the roAp stars is not the result of rotationally perturbed m-modes.

A shortcoming of this simple model put forth by Kurtz (1982) is in the amplitude asymmetry observed between split frequencies. From Equation 1.12, we see that the split frequencies should have the same amplitude. This is not the case for the Ap stars. This problem is avoided if one takes into account the effects of both rotation and magnetic field on the frequencies through the Coriolis and Lorentz forces. This correction by Dziembowski & Goode (1985) correctly predicts both the rotationally split frequencies and the amplitude asymmetries.

The most recent contribution to the oblique rotator model comes from Bigot & Dziembowski (2002). They used a non-perturbative approach to show that the centrifugal force is important in determining the frequency shifts while the Coriolis force is dominant in determining the amplitude asymmetries. These authors also show that the pulsation, rotation, and magnetic axis are all inclined to each other.

1.5 The roAp Star HR 1217

The focus of thesis is the Ap star HR 1217; a.k.a HD 24712 or DO Eri. This was one of the first Ap stars to be identified as a roAp star (Kurtz, 1982) and has since become one of the most studied. Recently, high-quality data has provided information about the abundance, magnetic and photometric characteristics of HR 1217. The most recent photometric data is presented in Chapter 2 of this work. A review of some of the other

recent observations of HR 1217 is presented in this section.

As introduced in Section 1.1, the spectral anomalies in Ap stars are believed to be the result of abundance enhancements on the surface of the star. The first thorough abundance analysis HR 1217 was performed by Ryabchikova et al. (1997). Their results are consistent with the idea that the abundance enhancements on the surfaces of these stars are patchy. In particular they find the mean chemical abundances vary with the magnetic and rotational phase of the star. Since the abundances are believed to be concentrated near the magnetic poles, this spectral variation may be described by the oblique rotator model discussed in Section 1.2.2. When compared to the Sun, the rare earth elements are the most overabundant. With the exception of Mg, they also show the largest change over the $\approx$ 12 day rotation period of this star. The iron peak elements, on the other hand, are under abundant. The exception in this case being in Co, which is overabundant.

Using the techniques outlined in Section 1.2, Bagnulo et al. (1995) were able to model the magnetic field geometry for HR 1217. Their results yield values of 137°, 150°, and 3.9 kG for i, β and B_p respectively. Estimated uncertainties on the above angular measurements are $\approx 2-3°$ and the uncertainly of the polar field strength is $\approx$ 5%. The mean longitudinal field, B_l, for HR 1217 varies between $\approx$ 0.5 and 1.5 kG (Preston, 1972). This is illustrated in the lower panel of Figure 1.3. Agreement between theory and observations of the magnetic field for Ap stars is currently among the best in the case of HR 1217 (Bagnulo et al., 1995, and Bagnulo 1998).

The frequency spacing of HR 1217 is a perfect illustration of the difficulties that arise in identifying oscillation modes. In 1986, a global observation campaign headed by Don Kurtz and Jaymie Matthews collected photometric data for HR 1217 (Kurtz et al., 1989). Their goal was to achieve as much continuous coverage of the star as possible so that gaps in their data would not affect their frequency analysis. They achieved a 29% duty cycle with 325 hrs of data spanning a 46-day period. A schematic diagram of the principal frequencies that they identified is found in Figure 1.4.

As discussed in Section 1.4.2, there exists an ambiguity in identifying $\Delta\nu$ from the

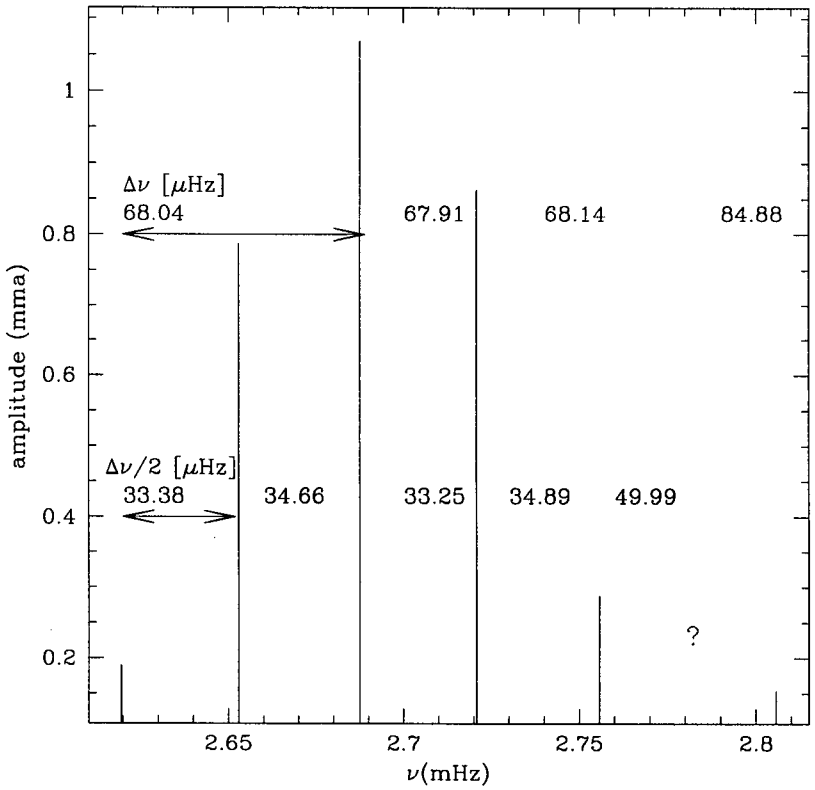

Figure 1.4: Above is a schematic diagram of the frequencies found from the 1986 observations of HR 1217 (Kurtz et al., 1989). The axis are amplitude in *milli*magnitudes and frequencies in mHz. The two possible values of either $\Delta\nu$ of ≈ 68 μHz (blue) or $\Delta\nu/2$ of ≈ 34 μHz (black) are shown. Note the *strange* spacing of 49.99 and 84.88 μHz indicating a possible *missing* frequency at the red label ?.

observed frequency spacing. Both $\Delta\nu$ and $\Delta\nu/2$ are presented in Figure 1.4. If the modes are alternating between even and odd ℓ values we would expect to see a $\Delta\nu$ of $\approx$ 68 μHz. In fact, the alternating spacing of 33 and 34 μHz add to this conclusion. If the

modes were all even or odd, we would expect that the spacing between adjacent modes in Figure 1.4 would remain the same. The possibility that the modes are all of the same degree cannot be ruled out. What is not shown in Figure 1.4 is the fine structure spacing around all but the first frequency (read from the left). Each of the frequencies, 2 through 6, are actually triplets with frequency spacing of approximately 0.9 μHz; the rotational frequency of the star. The origin of these splittings was discussed in Section 1.4.3. Suffice it to say, the unexpected frequency spacing between the last two frequencies in Figure 1.4 does not help determine if we are observing the large spacing or half of the large spacing.

It was only in the past few years; almost a decade after Kurtz et al. (1989) released their results, that the spacing controversy seemed to be resolved. Using Equation 1.9, Matthews et al. (1999) were able to calculate a parallax for HR 1217 based on an inferred large spacing of 68 μHz. Their predicted parallax of $\pi = 19.23 \pm 0.54$ *mas* was shown to be consistent with the recent *Hipparcos* parallax of $\pi = 20.41 \pm 0.84$ *mas*. Thus, a $\Delta\nu/2$ of 34 μHz seems to have been ruled out by an observation made independently from asteroseismic analysis.

Another recent success in the interpretation of the frequency spacing of HR 1217 was provided by Cunha (2001). She predicted that magnetic damping could be the cause of the missing frequency in the 1986 data set. She also showed that some frequencies may be shifted by approximately 10-20 μHz because of magnetic field effects (Cunha & Gough 2000, and Cunha 2001). In 2000, HR 1217 was selected to be observed in another global campaign (see Chapter 2). A preliminary data reduction for this data set did find a new frequency at approximately 2.79 mHz (Kurtz et al., 2002); adding further evidence that the magnetic field and the oscillations in roAp stars are interconnected.

1.6 An Overview of this Thesis

Progress in the study of the Ap and roAp stars has been steadily increasing over the past few years with the development of new observational and theoretical tools. In this thesis I attempt to tie together the most recent photometric observations of the roAp star HR

1217 with the latest grid of A star evolutionary and pulsation models.

In Chapter 2 I outline the reduction and frequency analysis of the photometric data on HR 1217 obtained by the Whole Earth Telescope collaboration in late 2000. An introduction to the global observation concept and data acquisition is presented in Sections 2.1 and 2.2, respectively. The reduction procedures applied to the raw time-series data and the frequency analysis follows in Sections 2.3 and 2.4. The results of the analysis is then presented in Section 2.5 and compared to results obtained using a variety of data weighting schemes in Section 2.6.

Theoretical evolutionary and pulsation models are presented in Chapter 3. Although the main focus of this thesis is HR 1217, the evolutionary models calculated for this work cover a large enough parameter space to be relevant to other roAp stars. Specific improvements to the pulsation models (see Sections 3.2 through 3.3.1) include both non-adiabatic (energy gains and loses through radiative processes) and magnetic effects.

A final discussion comparing the results of the data analysis and the stellar models is presented in the final chapter of this work.

Chapter 2

Data & Analysis

2.1 The Whole Earth Telescope

The Whole Earth Telescope (WET) is a collaboration of astronomers and facilities from around the world whose collective goal is to obtain high-quality, continuous, time-series photometry of variable stars. Originally, WET was organized to study variable, degenerate stars. Its goals were expanded to include types of variables such as δ Scuti, roAp, cataclysmics, and sub-dwarf B stars.

The main advantage of a global campaign over single-site observations is the reduction of data gaps in a given set of time series measurements. Such gaps are common with single-site observations because any particular star is only visible for a certain fraction of the night. In a global campaign, observatories are distributed in longitude, so one site can start observations when another site has finished (see Figure 2.1). In principle, continuous coverage of a chosen target can be obtained. Of course, weather and/or equipment problems may also lead to a loss of data. The effect of these missing data is seen as aliasing in frequency analysis of variable stars. The gaps produce additional peaks in the Fourier spectrum of the data, making identification of a real oscillation frequency difficult.

The more facilities that participate in a WET run, the greater the possibility for longer observing time on a target. This increases the frequency resolution of the data and helps identify fine structure in the Fourier spectrum. This fine structure is crucial for mode identification, rotational information, and in the case of the roAp stars, information about the magnetic field. For reviews of WET see Winget (1993), Kawaler et al. (1995)

and references therein.

2.2 Observing HR 1217 with WET

High-speed photometry is the preferred technique for observing roAp stars. This technique involves a continual monitoring of the star, with no observations of comparison stars. By doing this, the observations are non-differential. A constant change between observing a target star and a comparison star results in a loss of data on the rapid light variations exhibited by roAp stars. The use of CCDs for differentially observing roAp stars is also problematic because it is usually difficult to find a bright comparison star in a small CCD field. Continuous viewing of a target star relies heavily on precise auto-guiding and properly balanced instruments. Otherwise, a star that is centred in the diaphragm can drift; causing either a loss of light or light contamination from nearby stars. If such drifts are periodic, spurious frequencies may appear in the data.

Since HR 1217 is a bright star; with a magnitude of $B \approx 6.3$, background light is not a major problem. Thus, isolating the star in a diaphragm with a diameter less than 20 arcseconds will not significantly reduce the ratio of sky-light to star-light. The principal source of noise in the frequency range of interest is scintillation (short-period sky transparency variations). The rapid oscillations of roAp stars; with periods of approximately 5 minutes, are not affected by sky variations that occur with periods of a half-hour or more. A good review of the general technique for observing roAp stars with WET is provided by Kurtz & Martinez (2000).

In late 2000, the Whole Earth Telescope launched its twentieth extended coverage campaign, XCOV20 [1]. HR 1217 was included as one of the primary targets of this campaign, which ran from Nov. 6 to Dec. 11. During XCOV20, a variety of telescopes and instruments were used. The telescope apertures ranged from 0.6 m to 2.1 m and instruments included one-, two- and three-channel photo-electric photometers. In particular,

[1]Information on XCOV20 may be found on the World Wide Web at: http://wet.iitap.iastate.edu/xcov20/

observations at CTIO [2] used a two-channel photometer, while observations at BAO [3], Naini Tal [4], Teide [5], Mauna Kea[6], and McDonald [7] used three-channel photometers. The single-channel photometers were used at SAAO [8], Perth [9], and SSO [10]. Each of these sites are shown on the map in Figure 2.1. The three-channel photometers and sky monitoring procedures are described by Kleinman et al. (1996). Observations with one- and two-channel photometers sampled the sky a number of times for each run, while the three-channel photometers were able to continuously monitor the sky. Each site observed the target using a Johnson B filter with 10 sec integration times. Since HR 1217 is a bright star, larger telescopes required neutral density filters to keep count rates below 10^6 s^{-1} in order to avoid saturating, or damaging, the phototubes. Photoelectric photometers currently provide a higher level of precision than CCD photometers when count rates are this high. Comparison stars were not specified for the multi-channel photometric observations. The selection of these stars was at the discretion of each individual observer.

A complete log for all HR 1217 observations can be found in Table A.1[11] of Appendix A. This log includes the observatories that participated, the dates of participation and the telescope that was used. Kurtz et al. (2003) review the XCOV20 observing run with emphasis on HR 1217. The need for high-precision data results in some runs being selected for the final data analysis while others had to be discarded. Runs were not used if they exhibited noise levels that were too high for the sub-millimagnitude precision required to identify low-amplitude frequencies in the data. Data selection and further detail on reduction procedures are outlined in the following sections of this chapter.

[2]Cerro Tololo Inter-American Observatory, Chile
[3]Beijing Astronomical Observatory, China
[4]Uttar Pradesh State Observatory, Naini Tal Manora Peak, India
[5]Observatorio del Teide (Tenerife), Spain
[6]Mauna Kea Observatory, Hawaii, U.S.A
[7]McDonald Observatory, Texas, U.S.A.
[8]South African Astronomical Observatory, South Africa
[9]Perth Observatory, Australia
[10]Sliding Spring Observatory, Australia
[11]This data log was adapted from the one on the XCOV20 website

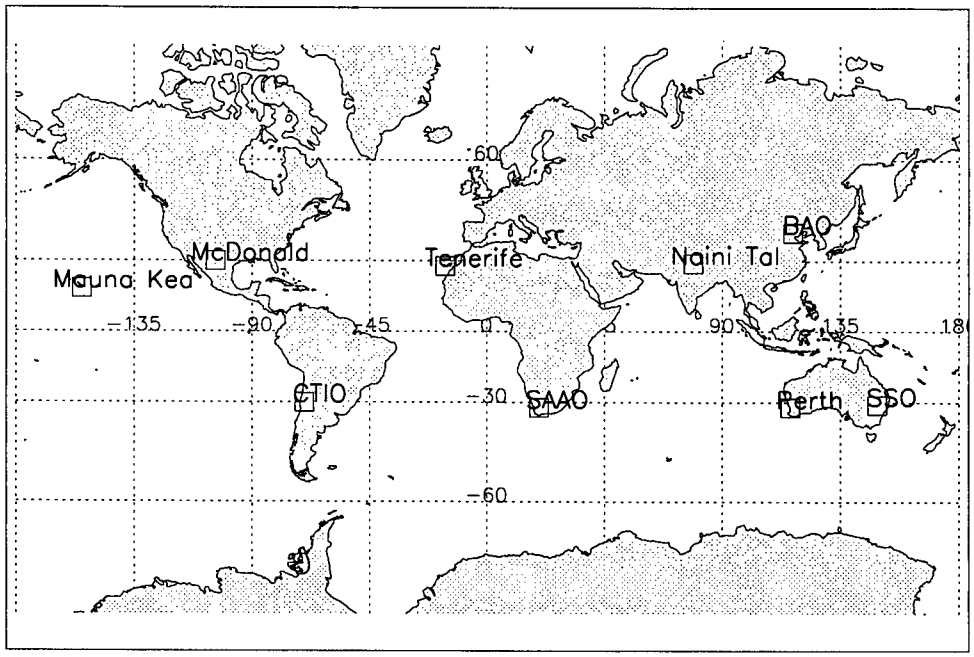

Figure 2.1: A map of the observatories that participated in the observations of HR 1217 during XCOV20. Further information about the locations may be found in Section 2.2, and in Table A.1

2.3 Preparing the Light Curves

Each individual run was reduced following the procedures outlined by Nather et al. (1990). The standard reduction software for WET is called *QED*. This software performs various photometric reduction tasks such as: deadtime corrections, sky interpolation and subtraction for multiple channels, sky extinction corrections, and polynomial fitting of light curves. It is important to use a standard reduction package to reduce each run so that numerical artifacts from the use of multiple programs do not appear. This uniform reduction also allows for easy comparison between individually reduced runs. The reference manual for *QED* was written by R.E. Nather in 2000 and can be found on the World Wide Web[12]. An overview of the reduction procedure for an individual run is described below.

[12]http://bullwinkle.as.utexas.edu/~wet/contents.htm

QED begins by reading a file containing the star name, the observatory, the instrument used, the integration time used, default extinction coefficients and the raw counts as a function of time from the beginning of the run. The data is displayed on the screen so the user can identify bad data by eye. The selection of bad data is subjective, and the person performing this initial step uses individual observing logs to help identify such points. Typically, bad data points include those collected while clouds pass in front of the star, or points that have counts inconsistent with the rest of the run due to the star drifting in the diaphragm. The sky measurements are obtained by observing the sky; i.e., a measurement while there is no star is in the diaphragm. These sky measurements are marked where indicated in the observing logs.

The deadtime corrections and the sky subtractions are then performed on the data. The deadtime is the recovery time after a photon hit when the photomulitplier tube and the preamp are unable to register another pulse. Thus, this correction takes into account the time lost between measurements. Each of the channels has a deadtime correction applied and the default deadtime constants for each instrument are used. The deadtime correction to the counts is given by $C_t = C_0/(1 - C_0 t_d)$, where C_0 is the original count, C_t is the corrected count, and t_d is the deadtime constant. These constants can be changed in *QED* if measurements are available. Typically, constants are on the order of 50 nanoseconds. Once the deadtime correction is applied, a linear trend interpolated from the sky measurements is subtracted from the stellar data.

As a star is observed throughout the night, its measured brightness changes due to varying airmass. The airmass is simply the thickness of the atmosphere as a function of the zenith angle z. This change in brightness is known as the atmospheric extinction X and it is related to the zenith angle by (Hiltner, 1962)

$$X = sec(z) - 0.0018167(sec(z)-1) - 0.002875(sec(z)-1)^2 - 0.0008083(sec(z)-1)^3 \quad (2.1)$$

Once the atmospheric extinction is calculated, the counts are corrected using the equation $log_{10}(C_s/C_i) = k_{ex}X/2.5$. In this relation, C_i and C_s correspond to the instrumental counts and the corrected counts respectively. The extinction coefficient is given

by k_{ex} and is adjusted in order to remove as much of the extinction trend as is possible. Thus, if the extinction correction perfectly subtracts brightness variations caused by airmass, the light curve would have no long-term trend. For light curves where the extinction correction doesn't remove such long term trends completely, polynomials of varying degree were subtracted from the curve. The degree of the polynomial never exceeds 3, and in most cases, a parabolic or linear fit was sufficient.

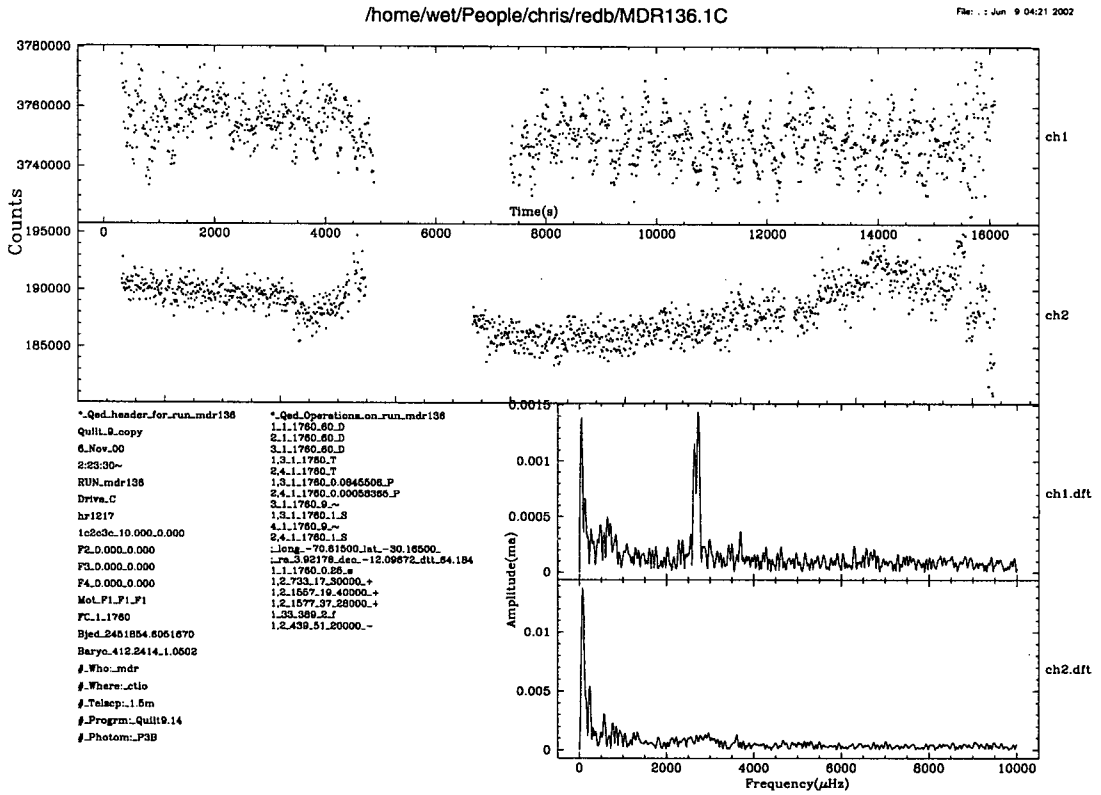

Figure 2.2: The end result of the *QED* reduction for run mdr136 at CTIO. The top panels show the channel 1 (top) and 2 data and the lower panels show the Fourier transforms of each. Again, channel 1 is the top Fourier plot. The reduction details from the *QED* output are printed on the Figure.

The results of the above reduction procedures using *QED* are shown in Figure 2.2 for the run mdr136 (see Table A.1). A two-channel photometer was used and each of the reduced channels can be seen in the top two panels of the Figure. The Fourier transforms

of each of the channels is shown in the lower two panels. These Fourier plots show power at low frequencies from remaining long-term trends in the data.

Small heliocentric corrections to the times caused by changes in the Earth's position with respect to the star due to its orbital motion had to be taken into account. As a final step after the *QED* reduction, the time data for each run are placed in the same inertial frame and the counts are normalized about the mean count. A suitable reference frame for all of the times is the barycenter of the Solar System. Thus, each run has its times corrected with reference to the barycenter of the Solar System and listed since a time T_0. For XCOV20, $T_0 = 2451854.5$ barycentric Julian Date (BJED). The final result is then binned in 40 sec bins to increase signal to noise and to decrease computational time during the frequency analysis. This data then goes through a selection procedure described in the following section.

2.3.1 Run Selection

Before frequency analysis could begin, runs with the best signal-to-noise had to be selected. First, low-frequency noise was removed by fitting and subtracting sinusoids with frequencies below approximately 1 mHz. The frequencies and amplitudes were selected using the software *Period*98 [13] (Sperl, M. 1998). More details on this software package can be found in Section 2.4. Low-frequency noise in the data is caused by long-term sky variations and other instrumental drifts. Such frequencies should have ideally been removed by the extinction correction and a low-order polynomial fit; however, amplitudes with periods greater than a half-hour do remain in some runs. The removal of such frequencies does not affect the frequencies above 2 mHz that are important in roAp star studies.

The Fourier spectrum of each run was examined and those that had a signal-to-noise greater than approximately three at the frequency with the largest amplitude were selected. Figure 2.3 shows examples of a selected run and a rejected one. The noise level

[13] http://www.astro.univie.ac.at/~dsn/dsn/Period98/current

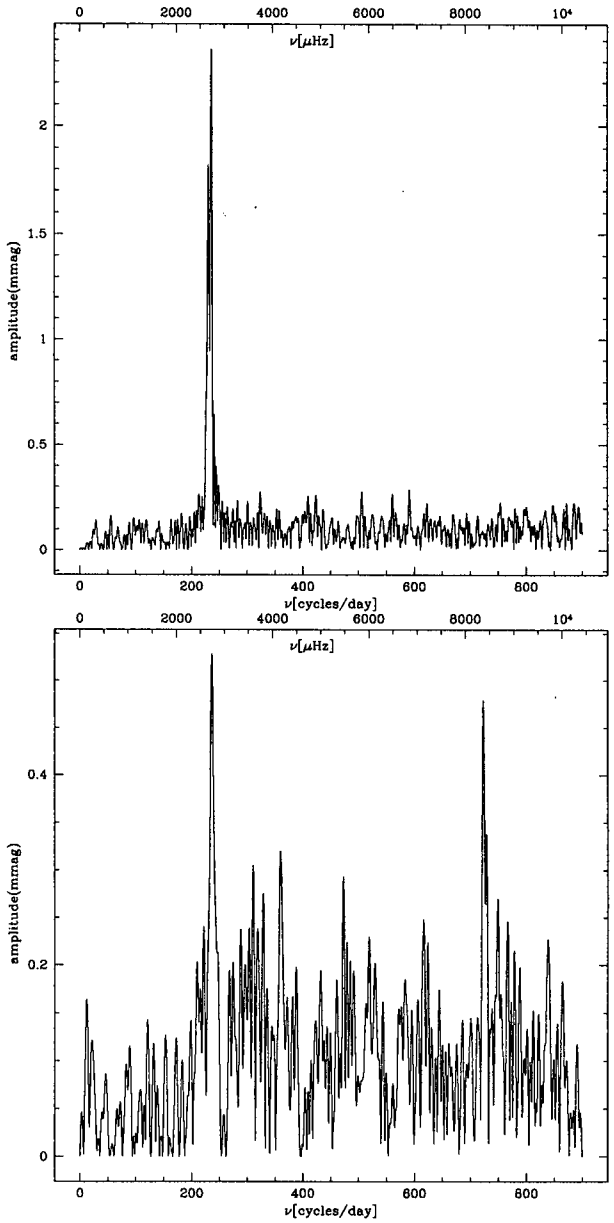

Figure 2.3: A Fourier spectrum of data from the runs no2900q1 (top) and joy-002 (bottom). It is clear that the amplitude and noise levels for the no2900q1 are much better than those in the joy-002 run. There is also a large frequency at approximately 720 cycles/day (8.3 mHz) in the joy-002 run caused by a periodic drive error in the telescope.

and amplitude of the main frequency at approximately 2.7 mHz is clearly different for both runs. Although the amplitudes of roAp oscillations can vary over the rotation cycle of the star, the low signal-to-noise in the joy-002 (bottom plot in Figure 2.3) run makes it unacceptable for further frequency analysis.

After bad runs were eliminated, the remaining data consists of 330.5 hrs of photometry over a period of 35 days, as plotted at a compressed scale in Figure 2.4. This covers slightly less than three rotation cycles of HR 1217, which has a rotation period of approximately 12.5 days. The resulting duty cycle for the entire run is 33%.

2.4 Frequency Analysis

All frequency analysis was performed using the software package *Period*98 (Sperl, 1998). This package uses a nonlinear least squares fitting method to calculate the amplitudes, frequencies, and phases that minimize the residuals of a given fit to the data. The fitting function is a sinusoid of the form

$$f = Z + \sum_i A_i \sin[2\pi(\nu_i + \phi_i)] \tag{2.2}$$

where Z is a zero-point offset that takes into account any linear trends in the data. A_i and ϕ_i are the amplitude and phase of the i^{th} frequency ν_i, respectively.

Period98 does not rely on prewhitening to calculate a frequency solution for the light curve. Prewhitening is the process where by a periodic function is removed from the data and the residuals are used for the next step in the reduction procedure. By doing this, each frequency depends on the previously determined frequencies through the residuals. This process is used to determine which frequencies are included in the fit. The frequency with the largest amplitude in the Fourier spectrum is identified and used as a guess frequency for the least squares calculation. The residuals from this fit are then used to identify the next highest frequency. At each step, all identified frequencies, amplitudes and phases are improved via the least squares calculation. This process of parameter identification and improvement continues until the amplitudes in the Fourier

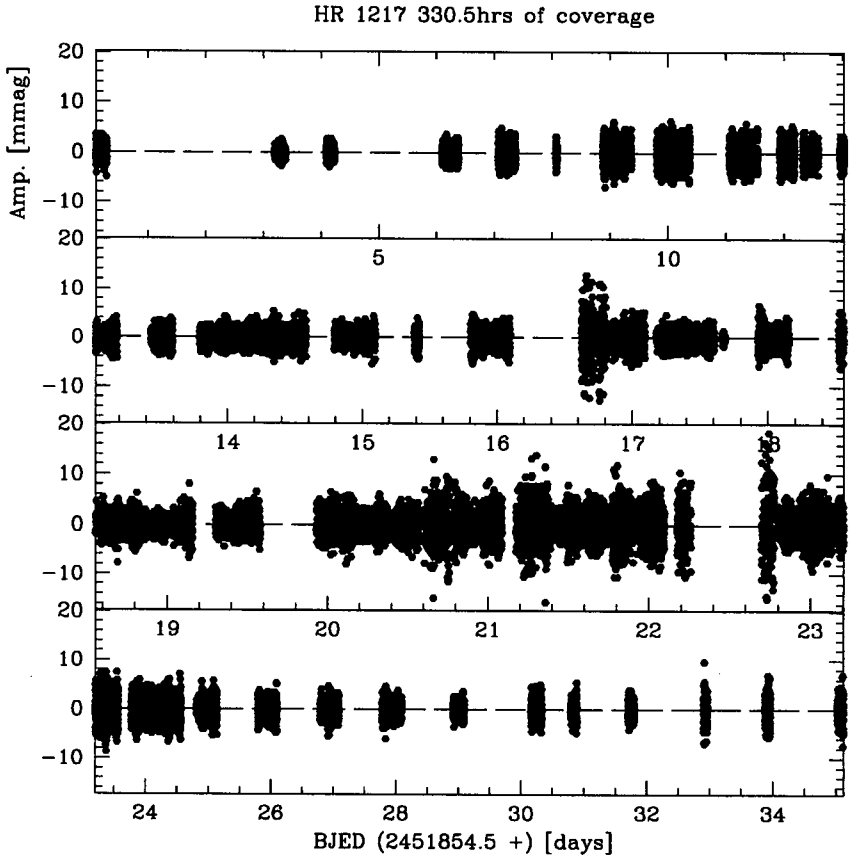

Figure 2.4: The final light curve obtained after the QED reduction and the barycentric corrections have been taken into account. The light curve shows 330.5 hrs of data which corresponds to a duty cycle of approximately 33%. The amplitudes are measured in units of millimagnitude.

spectrum are at the level of the noise.

A moving average technique is used to estimate the noise level in the Fourier spectrum. *Period98* calculates the average of the amplitudes in the Fourier spectrum in a given frequency bin and then moves along to the next frequency bin. If the noise was white (frequency independent), one could simply model it with a Gaussian centered on the frequency with the highest amplitude. However, WET data obtained from different instruments, under varying seeing conditions, contribute differently to the noise of the

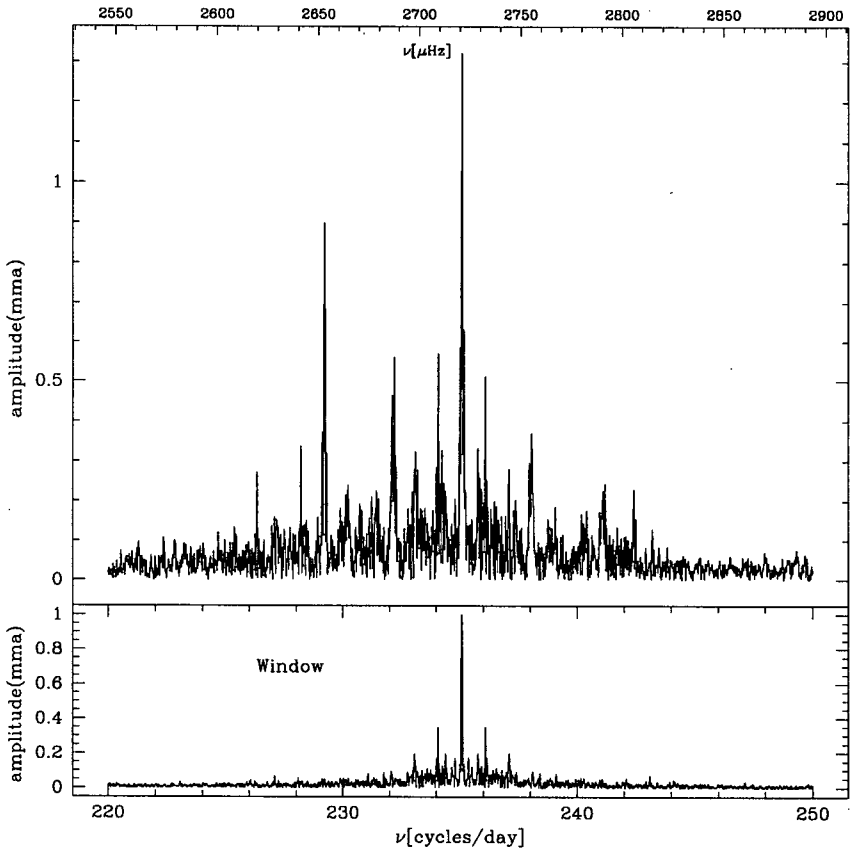

Figure 2.5: The Fourier spectrum of the entire run shown in Figure 2.4. The lower panel shows the window function for this data. The window was calculated from the Fourier transform of a sinusoid with the largest amplitude frequency identified in the data and sampled at the same times as the data set.

data set. Therefore, if the box size is chosen appropriately, the average of the frequencies in each box represents the noise spectrum well.

The first search of Fourier space was performed in the range from 0 mHz to the Nyquist frequency of 12.5 mHz. All power in the Fourier spectrum was identified between 2.5 mHz and 2.9 mHz as was found in earlier observations (e.g., Kurtz & Seeman, 1983, and Kurtz et al., 1989). In order to speed the Fourier calculations the latter frequency range was explored and sampled at 1×10^{-5} mHz intervals. The results of the analysis

will be presented in Sections 2.5 and 2.6. The noise of the spectrum was calculated at intervals of 3×10^{-3} mHz using a frequency bin size of 23 μHz (2 cycles/day). This bin size was chosen so that only the noise near the frequency being considered was used in the calculation. .

2.5 The Unweighted Data Results

The results of the above reduction procedures for the unweighted data set are shown in Table 2.1. Presented are 21 frequencies consisting of 8 primary frequencies and their rotational splittings. Frequencies labeled ν_1 through ν_5 and ν_7 are consistent with those identified by Kurtz et al. (1989) in the 1986 campaign. This analysis also recovers the *new* frequency of 2791.48 μHz that was predicted by Cunha (2001) and reported by Kurtz et al. (2002) (see Section 1.5). This frequency is labeled $\nu_6(old)$ for this data set. In addition, a previously unknown frequency is reported in this work at 2788.94 μHz. This frequency fits the alternating spacing pattern of 34.5 and 33.5 μHz and is labeled as $\nu_6(new)$ in Table 2.1. The spacing between $\nu_6(new)$ and $\nu_6(old)$ is 2.63 μHz and the spacing between $\nu_6(old)$ and ν_7 is approximately 15 μHz.

This new frequency was not previously identified by Kurtz et al. (2002) because they examined a smaller subset of the data. Including more data (i.e., extending the time coverage) increases the frequency resolution because the discrete Fourier transform is weighted exponentially by the number of data points. Thus, increasing the length of a data set produces shaper spectral features. A numerical analysis by Loumos & Deeming (1978) also showed the spectral resolution Δf of a data set of length ΔT is given approximately by $\Delta f = 1.5/\Delta T$. An application of this relation for uncertainty estimates is given in Section 2.5.1.

A schematic amplitude spectra for these results is given in Figure 2.6.

Table 2.1: Results of the frequency analysis of the unweighted data. The frequencies, amplitudes and the phases are shown. The rotational spacings $\delta\nu$ and the infered large spacings, $\Delta\nu$, are also shown. $\nu_6(old)$ was the sixth frequency found previously by Kurtz et al. (2002) and $\nu_6(new)$ is a new frequency identified in this study.

ν_n	ν (mHz)	Amp.(mma)	ϕ	$\delta\nu$(mHz)	$\Delta\nu$(mHz)
ν_1	2.61953721	0.247873599	0.061262411		
+	2.62052628	0.101942968	0.19455008	9.8907E-04	ν_2-ν_1
					0.03340692
-	2.6519788	0.239812675	0.006703652	9.6533E-04	
ν_2	2.65294413	0.793304662	0.145744578		
+	2.65389542	0.181838918	0.300326255	9.5129E-04	ν_3-ν_2
					0.03454836
-	2.68644247	0.332793541	0.200445295	1.0500E-03	
ν_3	2.68749249	0.554168633	0.11110511		
+	2.68841904	0.215781733	0.336983675	9.2655E-04	ν_4-ν_3
					0.03343462
-	2.72006539	0.408958037	0.505309948	8.6172E-04	
ν_4	2.72092711	1.14018239	0.782933145		
+	2.72182605	0.436426134	0.015917406	8.9894E-04	ν_5-ν_4
					0.03440263
-	2.75432171	0.218422957	0.114667745	1.0080E-03	
ν_5	2.75532974	0.278092265	0.224817247		
+	2.75623738	0.119315631	0.489636487	9.0764E-04	ν_6 **(new)**-ν_5
					0.03360699
ν_6 **(new)**	2.78893673	0.126677281	0.606594168		
+	2.78996948	0.090747676	0.507306041	1.0327E-03	
-	2.7906266	0.130919596	0.197095448	9.4253E-04	ν_6 **(old)**-ν_6 **(new)**
ν_6 **(old)**	2.79156913	0.193687427	0.37786162		0.0026324
+	2.79213576	0.070257486	0.092062776	5.6663E-04	
					ν_7-ν_6 **(old)**
-	2.80562143	0.190737069	0.450445087		0.0149975
ν_7	2.80656663	0.120611222	0.485536548	9.4520E-04	

The average value of the fine frequency structure is 9.27×10^{-4} mHz with a standard

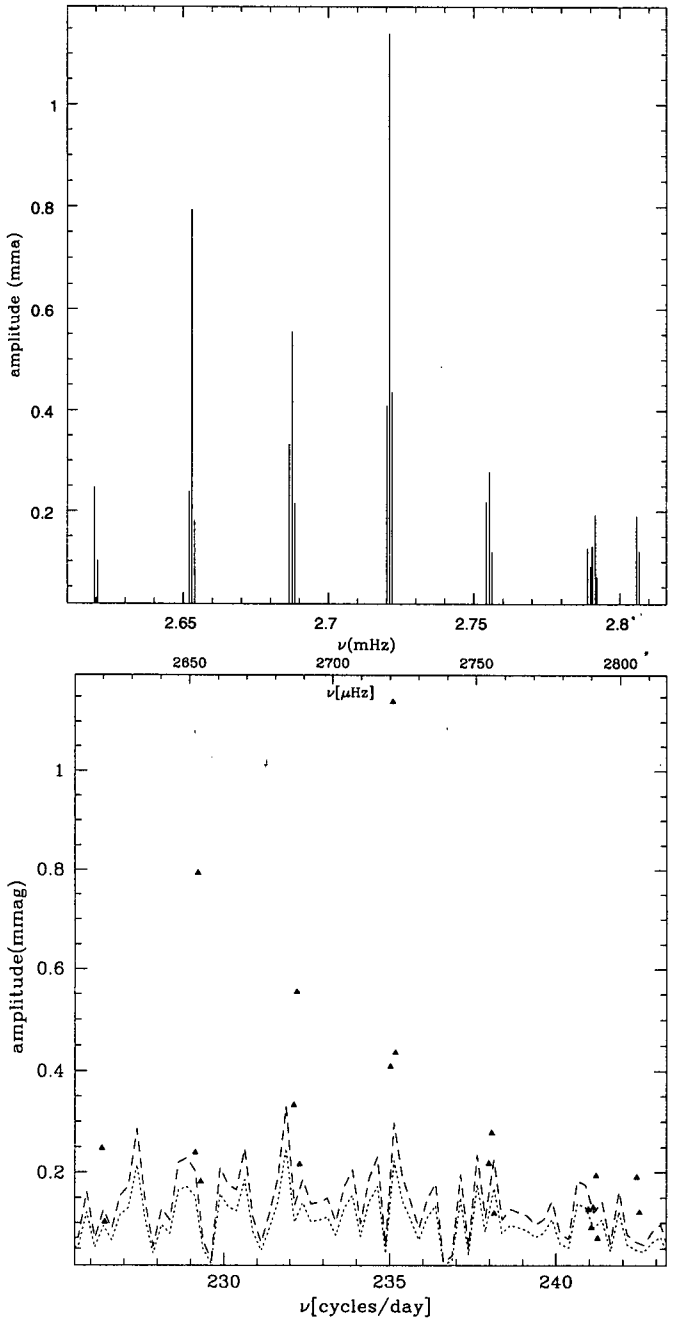

Figure 2.6: A schematic of the frequencies found from the unweighted data (top). The frequencies are listed in Table 2.1. On the bottom, the amplitudes of the frequencies and the noise level after all frequencies are prewhitened. The (- - -) line represent four times the noise level and the (. . .) line represents three times the noise level.

error on the mean of $\approx 1\%$. Assuming HR 1217 is an oblique rotator, the fine structure should be exactly spaced by the rotation frequency of the star. This would imply a rotation period of 12.5 days $\pm$ 1%; consistent with values of the rotation period derived in the literature. For example, Kurtz & Marang (1987) use photometry to deduce a period of 12.4572 ± 0.0003 days from the long term variability of HR 1217. Bagnulo et al. (1995) use linearly and circularly polarised light data and obtain a period of 12.4610 ± 0.0011 days from the magnetic field variations.

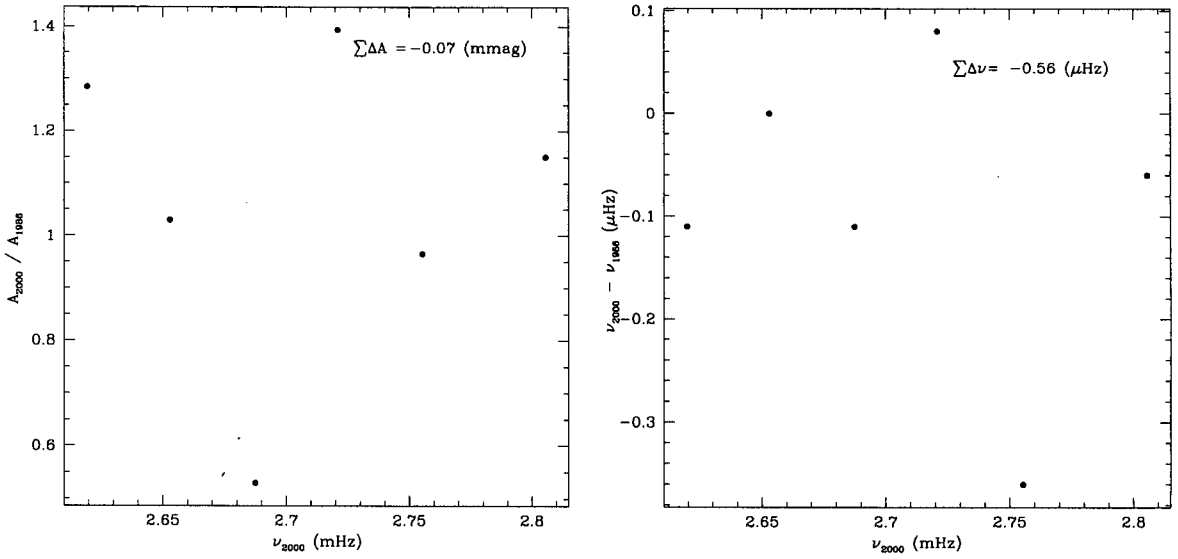

Figure 2.7: The ratio between the common amplitudes (top) and differences in frequencies (bottom) from this data set and the Kurtz et al. (1989) data set. The frequencies are consistent with each other while the amplitudes of the third and fourth frequency (read from the left) are clearly different. The net amplitude and frequency differences are shown in the upper right of each plot.

While the derived frequencies are consistent with the 1986 data, the amplitudes differ

significantly. Figure 2.7 compares the difference between the principle amplitudes and frequencies that were common to both this data set and the 1986 data. The amplitudes of frequencies ν_3 and ν_4 show the largest difference between the two data sets. They differ by approximately 60% and 40%, respectively. However, the net amplitude difference between the 6 frequencies is small, at -0.070 ± 0.192 mmag.

As each of the frequencies was identified and prewhitened, the standard deviation of the residuals was calculated. Frequencies were removed until the standard deviation of the residuals approached a constant value. These results may be found in Figure 2.8. After the twenty-first frequency was removed, the standard deviation of the residuals is improved by less than a 0.1%. Estimates of the uncertainty and significance of the derived frequencies will be discussed in the next section.

2.5.1 Estimating Uncertainties and Significance

Uncertainty estimates for the frequency analysis were carried out in three different ways. The first is that used by Kurtz & Wegner (1979) to estimate the frequency resolution of two closely spaced frequencies. They state that the Gaussian standard deviation associated with each frequency uncertainty is approximately one-sixth that of the frequency resolution estimated by Loumos & Deeming (1978). This may be calculated using

$$\Delta f = \frac{1}{4\Delta T} \tag{2.3}$$

where ΔT is the length of the observing run. Using this method, the frequency uncertainty is estimated as $\Delta f \approx 8 \times 10^{-5}$ mHz for $\Delta T = 35.12$ days.

The second method is closely related to the first and estimates the number of independent frequencies from the full-width-half-maximum (FWHM) of the main peak in the Fourier Spectrum (Alvarez et al., 1998). From Figure 2.9, the FWHM is estimated to be 6×10^{-4} mHz. This is approximately an order of magnitude above the uncertainty estimate from Equation 2.3.

The third technique estimates the uncertainty in phase, amplitude and frequency. This method assumes the times are certain and the counts are subject to random noise.

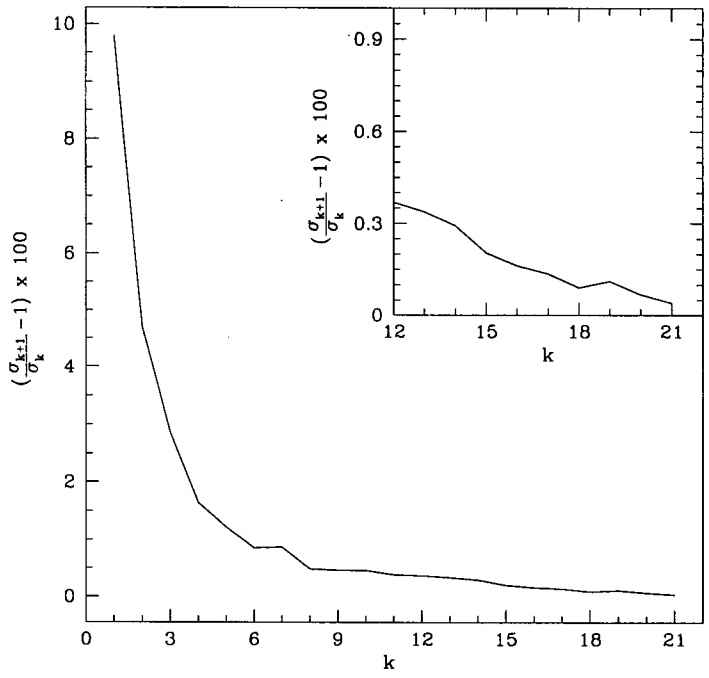

Figure 2.8: Improvement of the standard deviations of the residuals as each of the k frequencies are removed. Each of the frequencies are listed in Table 2.1. The frequencies are prewhitened in order of decreasing amplitude. The inset is a blow-up of the standard deviation for the low amplitude frequency improvements.

Assuming cross-terms between frequencies are small (i.e., all frequencies may be considered independent from each other), Montgomery & O'Donoghue (1999) and Breger et al. (1999) derive analytic equations for the uncertainty of the amplitude, phase and frequency for a least squares fit. These equations are, respectively,

$$\sigma_a = (2/N)^{1/2}\sigma(m) \tag{2.4}$$

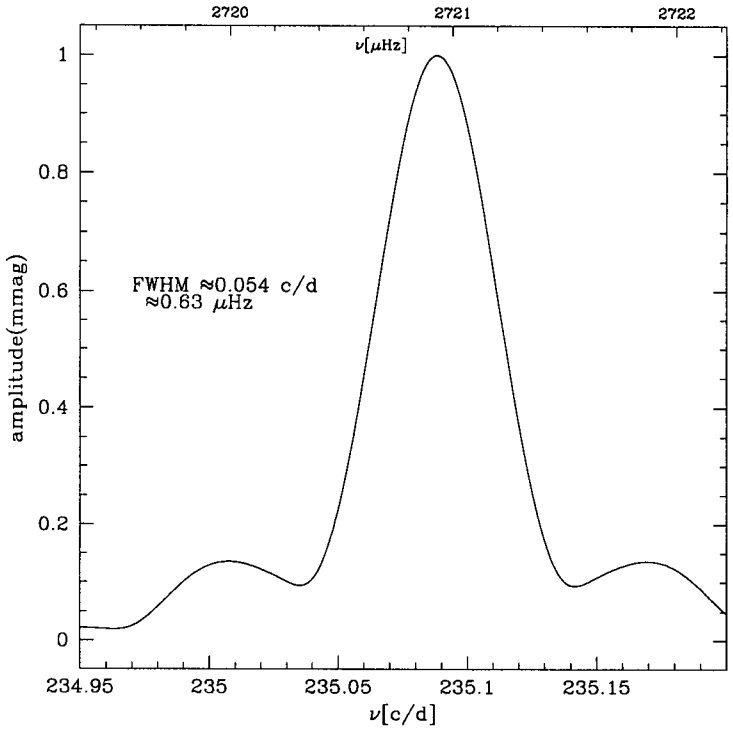

Figure 2.9: The FWHM of the main frequency in the unweighted data. This is used as an estimate for the uncertainty of the frequencies derived from the reduction of the unweighted data.

$$\sigma_\phi = (2/N)^{1/2} \frac{\sigma(m)}{a} \tag{2.5}$$

$$\sigma_\nu = (6/N)^{1/2} \frac{\sigma(m)}{\pi a T} \tag{2.6}$$

The amplitude being considered is represented by a, the length of the run is T, the number of data points N, and the root-mean-square of the residuals is $\sigma(m)$. These equations are applied to the residuals of the sinusoid fit as each frequency is prewhitened. The error estimates for this procedure are listed in Table 2.2.

According to Montgomery & O'Donoghue (1999), if the random noise is correlated with time, the uncertainties could be underestimated. They urge that these values only be taken as a lower limit of the uncertainty and suggest that the actual result may be an

order of magnitude higher.

If this is the case, and all of the uncertainties in Table 2.2 are increased by an order of magnitude, they would be consistent with the previous uncertainty estimates for this data. Kurtz et al. (2002) derive uncertainties formally from their least squares analysis during a preliminary data reduction. They obtain a frequency uncertainty that is $\approx 10^{-5}$ mHz. Given the above information, a conservative estimate on the frequency uncertainties would be 1×10^{-4} mHz.

Table 2.2: Uncertainty estimate for the unweighted data using Equations 2.4, 2.5, and 2.6. These values are taken as lower limits only.

ν_n	σ_ν (mHz)	σ_a(mma)	σ_ϕ	$\sigma_{\delta\nu}$(mHz)	$\sigma_{\Delta\nu}$(mHz)
ν_1	2.49E-06	0.0141	0.0054		
+	2.42E-06	0.0137	0.0052	4.91E-06	ν_2-ν_1
					5.16E-06
-	2.44E-06	0.0140	0.0053	5.11E-06	
ν_2	2.67E-06	0.0153	0.0058		
+	2.40E-06	0.0138	0.0052	5.07E-06	ν_3-ν_2
					5.23E-06
-	2.44E-06	0.0142	0.0053	5.00E-06	
ν_3	2.56E-06	0.0148	0.0055		
+	2.39E-06	0.0139	0.0052	4.95E-06	ν_4-ν_3
					5.29E-06
-	2.46E-06	0.0144	0.0053	5.18E-06	
ν_4	2.73E-06	0.0160	0.0059		
+	2.48E-06	0.0146	0.0054	5.21E-06	ν_5-ν_4
					5.13E-06
-	2.34E-06	0.0139	0.0051	4.74E-06	
ν_5	2.40E-06	0.0143	0.0052		
+	2.30E-06	0.0137	0.0050	4.70E-06	ν_6 (new)-ν_5
					4.68E-06
ν_6 **(new)**	2.28E-06	0.0137	0.0049	4.55E-06	
+	2.27E-06	0.0137	0.0049		
-	2.28E-06	0.0137	0.0049	4.61E-06	ν_6 (old)-ν_6 (new)
ν_6 **(old)**	2.33E-06	0.0140	0.0050		4.61E-06
+	2.27E-06	0.0137	0.0049	4.60E-06	

continued on next page

Table 2.2: *continued*

ν_n	σ_ν (mHz)	σ_a(mma)	σ_ϕ	$\sigma_{\delta\nu}$(mHz)	$\sigma_{\Delta\nu}$(mHz)
					ν_7-ν_6 (old)
-	2.28E-06	0.0138	0.0049	4.54E-06	4.59E-06
ν_7	2.26E-06	0.0137	0.0049		

Estimates for the signal to noise at which a frequency may confidently be identified are calculated by Kuschnig et al. (1997). Kuschnig used amplitude spectra with simulated noise in conjunction with the Hubble Space Telescope's Fine Guidance Sensor guide star data to show that a signal to noise of 3.6 would produce a 99% confidence level for frequency identification, while a signal to noise of 4.0 would produce a 99.9% confidence level. These levels are consistent with those suggested by Breger et al. (1993) and those discussed by Alvarez et al. (1998), and Breger et al. (1999). Those authors also state that this method is equivalent to the Scargle false alarm probability test (Scargle, 1982) which assigns a confidence level for an identified frequency assuming white noise. Following these authors, a significant confidence level for a frequency identification is obtained where the amplitude of the frequency is at least 3.5 times the noise (see Figure 2.6).

2.6 The Weighted Data Results

The data collected during a WET campaign has noise characteristics that are a combination of noise from each individual observing run. In order to obtain the best signal to noise, one must consider either removing some of the data, or weighting the data. Removing data may not be the most desirable alternative since gaps in the light curve produce aliases in the Fourier spectrum. This, in turn, confuses frequency identification. It is also important to note that the Fourier transform is weighted by the number of points considered. Thus, lowering the number of points by removing data will also increase the noise in the calculated spectrum. In this thesis, different weighting schemes will be considered in an attempt to produce the best frequency solution for the HR 1217

data. Two weighting schemes discussed in Handler (2003) will be described, as well as the modifications to these methods used in this work to analyze the HR 1217 data.

The first weighting scheme is sigma-cutoff weighting. In this method, each data point is weighted based on the residuals from a given fit. Each weight is assigned by the relations

$$\begin{aligned} w_i &= 1 & if \quad \sigma_i \leq K\sigma_{res} \\ w_i &= (K\sigma_{res}/\sigma_i)^x & if \quad \sigma_i > K\sigma_{res} \end{aligned} \tag{2.7}$$

where K and x are free parameters, σ_i is the rms residual of the i^{th} point and σ_{res} is the average standard deviation of the residuals.

For example, Rodríguez et al. (2003) choose values of $K = 1.0$ and $x = 2.0$. *Period98* uses this method to assign weights to data; however, K and x are fixed at 1 and 2, respectively, and it is up to the user to choose the cut-off amplitude σ_{res}. Frandsen et al. (2001) use this function of *Period98* as one of the weighting schemes in their paper. Both they and Handler (2003) caution that the value of σ_{res} should be chosen wisely. If it is not, bad data that falls within the cut-off could be given full weight, or good data could be given low weight. This method is also limited by its dependence on a predetermined solution to calculate residuals.

Another method of data weighting described in Handler (2003) is light curve variance weighting. In this method, the data are boxcar smoothed to remove the point-to-point differences in intensity. The inverse of the smoothing function is then used to assign weights to the data. By doing this, night-to-night variations in the data can be taken into account. The free parameters in this method would be the size of the time bin being considered and the exponent by which you weight the data; i.e., the x in Equation 2.7. The main disadvantage of this method is that the smoothing function can be greatly affected by outlying points. This may, in turn, result in an improper weight assignment.

In this study, four weighting methods based on the above schemes were tested. Each weighting procedure is summarized as:

method 1 : The *Period98* weighting scheme is used with a variety of cutoff

amplitudes σ_{res}.

method 2 : The data weights are assigned using Equation 2.7 with the average standard error of the residuals from a fit. This fit is obtained from the results of the unweighted data analysis (see Section 2.5). When Equation 2.7 is applied to data, the free parameters are varied to explore their effect on the final solution.

method 3 : The average standard error of the residuals to a fit are calculated at various time bins before Equation 2.7 is applied. This method is similar to applying weights from a smoothing filter in that the change in the noise from time bin to time bin is taken into account.

method 4 : The weights are calculated and applied using Equation 2.7 as each new frequency is added. By doing this, we don't rely on residuals from a final fit to the data. This method attempts to overcome the dependence on a predetermined solution by considering the weight to be a parameter that changes with each step in the frequency analysis.

Each of the results obtained from the above weighting schemes are compared to the results from the unweighted data through a statistic χ^2_{comp} defined by

$$\chi^2_{comp} = \frac{\sum_{i=1}^{N}(f_i - f_{fit})^2/(\sigma_i)}{\sum_{j=1}^{N}(f_j - f_{fit0})^2/(\sigma_{j0})} \tag{2.8}$$

where values with the subscript 0 refers to those obtained from the unweighted data, f represents an observed time-series data point, f_{fit} is a point calculated using Equation 2.2, and the standard error of the residuals from the fit for a given data bin are represented by σ.

Models with various time bins and cut-off amplitudes were considered. Some of the models considered modes to be triplets, quintets, or an alternating combination of both. Other models were constructed assuming that the frequencies are split by exactly the rotation period of the star. In the latter case, frequencies were adjusted after each least squares iteration to be split with a frequency of 9.2897×10^{-4} mHz; the average of the

measurements by Bagnulo et al. (1995) and Kurtz & Marang (1987). The frequencies, amplitudes and phases were then improved using *Period*98. All models are summarized in Table 2.3.

Table 2.3: A summary of the weighting parameters for the 34 different frequency solutions explored. The parameters are defined in Equation 2.7. The column labeled *method* refers to the weighting methods described in Section 2.6. The *points/bin* column is the number of data points per time bin. If *method* 1 is used, the cutoff amplitude is presented instead of the number of data points per bin. See the *comments* column for specific reduction details.

model #	**K**	**x**	**points/bin or $\sigma_{res}[mmag]$**	**method method = 1**	**comment**
1	1.0	1.0	500	2	The number of points in each time bin are varied; as are the weighting factor K and exponent x.
2	1.0	1.0	200	2	
3	1.0	1.0	800	2	
4	1.0	1.0	1100	2	
5	2.0	1.0	500	2	
6	2.0	1.0	800	2	
7	2.0	1.0	1100	2	
8	1.0	2.0	200	2	
9	2.0	2.0	200	2	
9	1.0	1.0	100	4	New weights are calculated as each new frequency is identified.
10	1.0	1.0	100	4	
11	2.0	1.0	100	4	
12	-	-	no weight	1	Calculate a solution where frequencies alternate between triplets and quintuplets. The ν_6 and ν_7 frequencies are described by triplets in this solution.
13	2.0	1.0	5	1	See model 12 comment (New Weight).
14	2.0	1.0	1	1	See model 12 comment (New Weight).

continued on next page

Table 2.3: *continued*

model #	K	x	points/bin or $\sigma_{res}[mmag]$	method method = 1	comment
15	2.0	1.0	0.8	1	See model 12 comment (New Weight).
16	-	-	no weight	1	Calculate a solution where all frequencies are triplets.
17	2.0	1.0	5	1	See model 16 comment (New Weight).
18	2.0	1.0	2	1	See model 16 comment (New Weight).
19	2.0	1.0	1	1	See model 16 comment (New Weight).
20	-	-	no weight	1	Calculate a solution with all frequencies as quintuplets except for the triplet ν_6 frequencies.
21	-	-	no weight	1	Calculate a solution where all frequencies are triplets and attemp to force $\nu_6(new)$ to be a quintuplet.
22	-	-	no weight	1	Adjust $\nu_6(new)$ to be a quintuplet.
23	2.0	1.0	1	1	See model 21 comment (New Weight).
24	2.0	1.0	5	1	See model 21 comment (New Weight).
25	-	-	no weight	1	Calculate a solution where the unweighted frequenies are adjusted to be exactly rotationally split.
26	2.0	1.0	5	1	See model 25 comment (New Weight).
27	2.0	1.0	1	1	See model 25 comment (New Weight).
28	2.0	1.0	0.8	1	See model 25 comment (New Weight).
29	-	-	no weight	1	Take the solution from model 20 and continually remove frequencies that have amplitudes below 0.06 mmag. Then recalculate the solution with the omitted frequencies.
30	-	-	no weight	1	Adjust frequencies to be exactly rotationally split.
31	2.0	1.0	5	1	Weight model 30 solution.
32	2.0	1.0	1	1	Weight model 30 solution.
33	-	-	no weight	1	The unweighted data is forced to be rotationally split; however, the amplitudes, frequencies and phases are not improved using *Period*98.
34	-	-	no weight	1	See comment 33. Now the amplitudes and phases are improved using *Period*98.

All models are compared to the unweighted data through Equation 2.8. The results

are shown in Figure 2.10. A lower χ^2_{comp} statistic implies lower residuals for the fit. In all cases explored, the improvement in the residuals was less than 1%. An altered version of the unweighted data was used to test the sensitivity of the χ^2_{comp} statistic to a poor fit. In this case; model number 33, the unweighted data had its fine structure spaced exactly by the rotation period of the star while the amplitudes and phases were not altered. The results indicate a χ^2_{comp} that is approximately 5% worse than in the other models. Model numbers 25 and 34 should be compared to model 33. Both of these models force the frequencies of the fine splitting for the unweighted data to be the rotational frequency of the star. The exception in model 25 is that the frequencies, amplitudes and phases were then improved using *Period*98. For model 34, only the amplitudes and phases were then improved using *Period*98.

The lowest peaks in Figure 2.10 correspond to models 14, 18, 27 and 32. Schematic amplitude diagrams showing the weighted noise are presented in Figures 2.11 and 2.12. In all cases considered, ν_7 shows only a significant doublet structure. Each of the other frequencies show, at least, significant triplet structure. Complete data tables for these 4 models are given in Appendix C.

In the other cases, a standard error was computed for models with the same frequencies, but with different weight parameters. The results show that the frequencies only vary by approximately 10^{-6} while the amplitudes differ by less than a half of a percent. Changing the parameter space for the data weights has little effect on the outcome of the data. The computed standard errors for all cases are also presented in Appendix C.

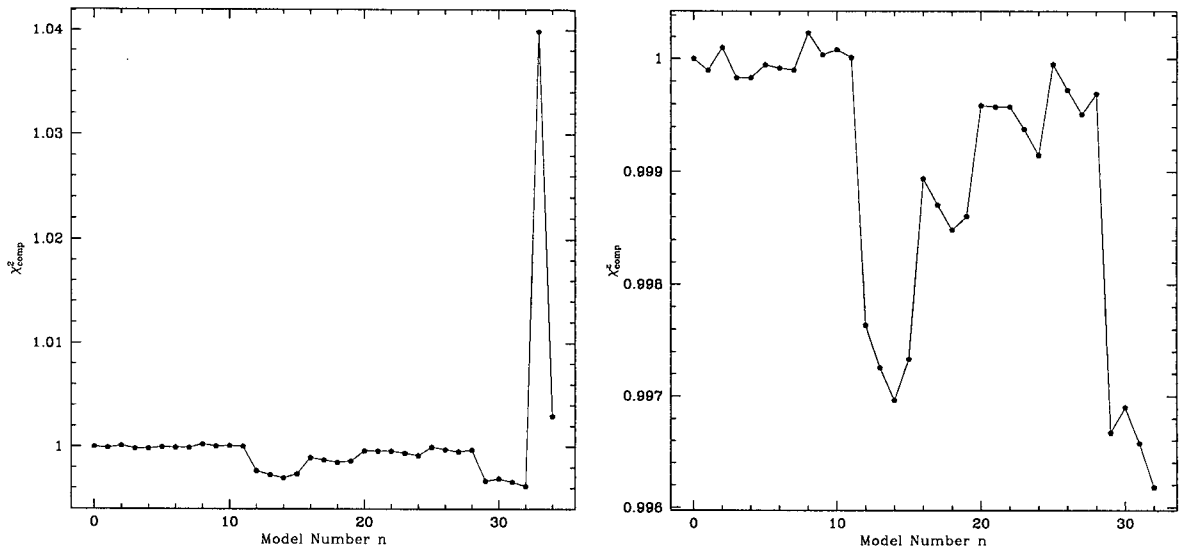

Figure 2.10: A comparison between the weighted and unweighted models using Equation 2.8. The plot at the top shows the statistic for the 34 models described in Table 2.3. The right plot is an expanded view of the first 32 models. In all cases, the models vary from the unweighted model by no more than 5%.

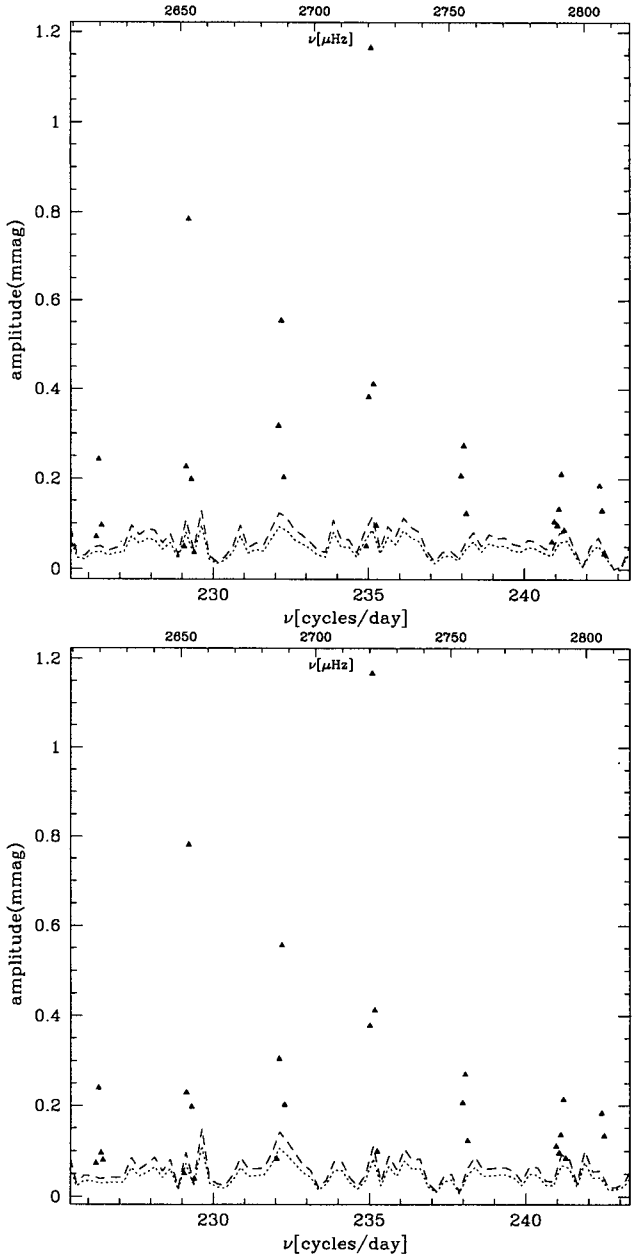

Figure 2.11: Schematic amplitude diagrams for models 14 (top) and 32 (bottom). The (- - -) line represent four times the noise level and the (. . .) line represents three times the noise level. The noise is calculated from the weighted residuals.

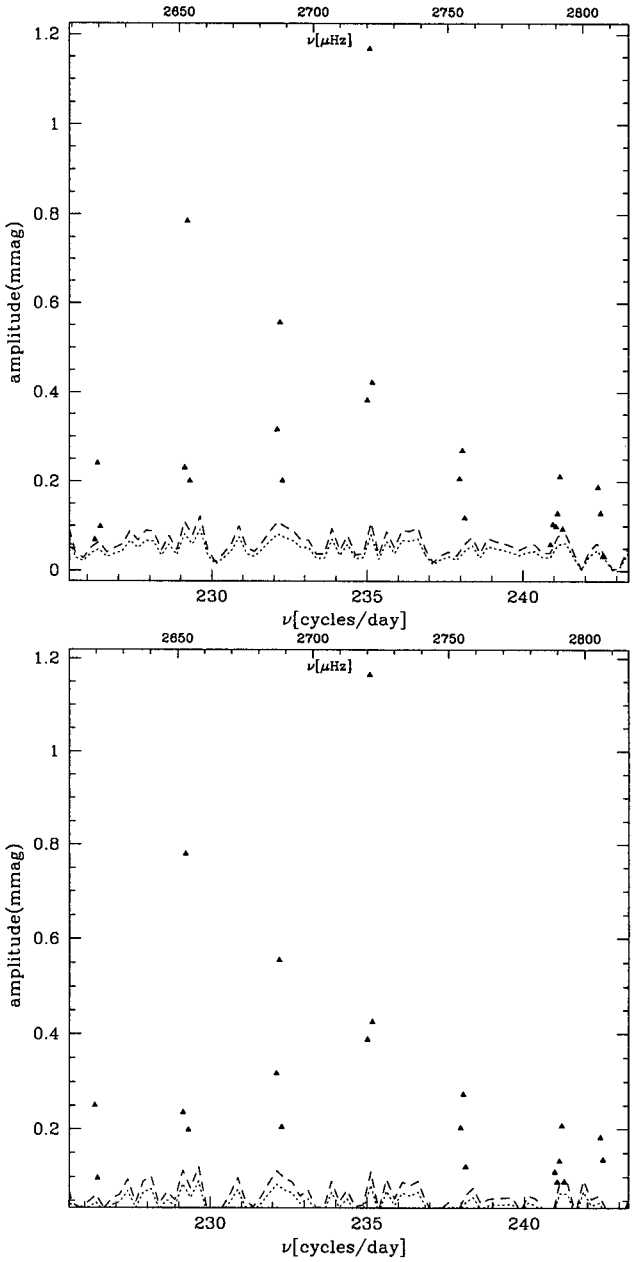

Figure 2.12: Schematic amplitude diagrams for models 18 (top) and 27 (bottom). The (- - -) line represent four times the noise level and the (. . .) line represents three times the noise level. The noise is calculated from the weighted residuals.

Chapter 3

Stellar Evolution and Pulsation Models

A grid of evolutionary and pulsation models of A type stars is calculated exploring a variety of parameters. The effect of a magnetic field on the resulting pulsation frequencies is also estimated for these models. In this chapter, the procedures for calculating the models are discussed and the results of the calculations are introduced.

3.1 Stellar Evolution Models

The stellar evolution models were calculated using the Yale Stellar Evolution Code with Rotation (YREC7) in its non-rotating configuration (Guenther et al., 1992). YREC7 solves the mechanical, conservation, and energy transport equations of stellar structure using the Henyey relaxation scheme (Henyey et al., 1964). A detailed discussion of the equations of stellar structure can be found in the text of Kippenhahn & Weigert (1994).

The density of a stellar model is related to the other material functions; i.e., the temperature and pressure obtained from the stellar structure equations, through the equation of state (EOS). YREC7 interpolates between OPAL EOS tables (Rogers 1986, and Rogers, Swenson, & Iglesias, 1996) with different compositions in order to obtain the appropriate densities for a particular model. The opacity routines needed to solve the energy transport equations of stellar structure are interpolated from two separate tables. If the temperature of a mass shell in a given model is greater than 6000 K, the OPAL opacity tables are utilized (Iglesias & Rogers, 1996). If the temperature of a shell is less than 15000 K, the low-temperature (molecular) opacity tables of Alexander & Ferguson

(1994) are used to obtain the opacity. In regions of the model where these temperatures overlap, a linear ramp function is used to link the two opacity tables. All tables are calculated for a solar elemental abundances (Grevesse et al., 1996).

From this structural information, the nuclear reaction network; e.g., the proton-proton or carbon-nitrogen-oxygen chains, is calculated for each model shell to determine the energy generated via nuclear burning using the nuclear cross sections of Bahcall et al. (2001). The new interior elemental abundances are calculated from this process and another model is evolved from this complete model to a later time step.

In this study, models are evolved from the zero age main sequence (ZAMS) to the approach of the base of the red giant branch (see Figure 3.1). Each model generated has approximately 3000 shells evenly distributed among the interior, envelope and the atmosphere. The model interior represents the inner $\approx 99\%$ of the model by mass while the envelope makes up the other 1%. The overlying atmosphere is calculated assuming a frequency independent temperature-optical depth ($T - \tau$) relation; known as the Eddington gray approximation.

3.1.1 The Parameter Space

To begin to specify a stellar model, the mass, luminosity, effective temperature and composition of the star are required. In most cases, there are spectroscopic observations that yield information about the effective temperature and the heavy metal (elements with atomic numbers greater than 2) content. The luminosity is also estimated from photometric observations, or apparent magnitude and parallax measurements; while the mass is only tightly constrained if the star belongs to a binary from which a confident orbital geometry may be derived. There is also the potential to use asteroseismic observations to further constrain the evolutionary status of a star through parameters like the large spacing $\Delta\nu$ (see Equation 1.7). Even if a stellar modeler had information on all these observable quantities, the standard treatment of convective energy transport adds another free parameter known as the mixing length parameter α (Böhm-Vitense,

1958). This parameter sets the number of pressure scale-heights a convective element rises before releasing its heat to the surrounding plasma.

Recently, Cunha et al. (2003) examined a set of stellar models for HR 1217 in hopes of determining its evolutionary status. Their results are complimentary to those of this thesis and there is an overlap in the choice of parameters to explore.

The effective temperature of HR 1217 is estimated from two sources. Ryabchikova et al. (1997) use their spectral synthesis code to estimate an effective temperature of $T_{eff} = 7250$; without a quoted uncertainty. The other estimate of the T_{eff} comes from the Strömgren photometry of Moon & Dworetsky (1985). Matthews et al. (1999) used this photometry to estimate an effective temperature of 7400 $\pm$ 100 K. In this work, we combine these to results to obtain $T_{eff} = 7400^{+100}_{-200}$ K. This is identical to the constraints on effective temperature used by Cunha et al. (2003).

The mass of HR 1217 is estimated from previous A star models to be approximately $2.0 \pm 0.5 M_{\odot}$ (e.g., Shibahashi & Saio, 1985, and Matthews et al., 1999). A tighter constraint for the mass of HR 1217 of $1.8 \pm 0.3 M_{\odot}$ is derived by Wade (1997) assuming it is a rigid rotator. In this study, the masses were varied from 1.3 to $1.8 M_{\odot}$ in $0.5 M_{\odot}$ steps.

The luminosity of HR 1217 is also estimated using two different approaches. The first is from the observed large spacing of $\approx$ 68 μHz. Using Equation 1.9 with the above estimates on T_{eff}, the mass, and the large spacing, a asteroseismic luminosity is calculated to be $8.2^{+1.6}_{-1.5} L_{\odot}$. If we observe half the large spacing of $\approx$ 34 μHz, the luminosity is estimated to be $20.7^{+4.0}_{-3.8} L_{\odot}$. The second method is a direct calculation of the stars luminosity from the *Hipparcos* parallax. Matthews et al. (1999) derive a luminosity of $7.8 \pm 0.7 L_{\odot}$ from the *Hipparcos* parallax; consistent with a $\Delta\nu \approx 68$ μHz.

The metallicity of HR 1217 is estimated from the spectroscopy of Ryabchikova et al. (1997), which indicates $[Fe/H] \approx 0.32 \pm 16\%$. Assuming Fe is a tracer of the interior metal content of a star, a heavy metal mass fraction of $Z = 0.008$ can be estimated from the relations

$$X + Y + Z = 1, \tag{3.1}$$

$$\left(\frac{Z}{X}\right)_{\star} = \left(\frac{Z}{X}\right)_{\odot} 10^{[Fe/H]}, \tag{3.2}$$

and

$$\frac{\Delta Y}{\Delta Z} = \frac{(Y_{\star} - Y_p)}{(Z_{\star} - Z_{\odot})} \tag{3.3}$$

where X and Y are the mass fractions of hydrogen and helium and $\Delta Y/\Delta Z$ is the Galactic enrichment parameter. The subscripts p, $\star$ and $\odot$ denote primordial, stellar and solar values, respectively. To complete the calculation, values of $(Z/X)_{\odot} = 0.0244$ (Grevesse et al., 1996), $Y_p = 2.232 \pm 0.003$ (Olive & Steigman, 1995), and $\Delta Y/\Delta Z = 2.5$ (Bressan et al., 1994) were adopted.

A difficulty arises for the Ap stars in that their inferred metal content from spectra dramatically changes over the magnetic phase of the star. Ryabchikova et al. (1997) give values of metallicity for both maximum and minimum magnetic phases. If it is (naively) assumed that the average of all of the metals for each of the magnetic maximum and minimum phases represent the interior heavy metal content of HR 1217, one can calculate from Equations 3.1 - 3.3, a Z that varies between 0.019 and 0.024. Thus, the inferred interior Z for HR 1217 can vary over a large range depending on how the surface metallicity is used. It should be noted that there is no reason to believe that the surface metal content of the Ap stars is representative of the interior metal content. However, for completeness, $Z = 0.008$ to 0.022 in steps of 0.002 is used for the evolutionary models; along with an estimated hydrogen mass fraction of $X = 0.700$ to 0.740 in steps of 0.020. The large extent of the parameter space in composition encompasses the uncertainties from the observed $(Z/X)_{\odot}$, Y_p, $\Delta Y/\Delta Z$, and [Fe/H] above.

Finally, mixing length parameters of $\alpha = 1.4,\ 1.6$, and 1.8 are used in the model grid. If a star possesses a convective envelope, α may be used to set the adiabatic temperature gradient at the base of the convective zone. Since the radius is a function of luminosity and T_{eff}, varying α will slightly change the radius of the model (Guenther et al., 1992). Since the envelopes of A stars are essentially radiative, any structural changes from the different values of α are small when compared to the total parameter space being considered.

3.1.2 Model Properties

To get an indication of the parameter space explored, the extremes of mass and composition are plotted on the theoretical Hertzsprung-Russel (HR) diagram in Figure 3.1. Shown are the error boxes calculated from the *Hipparcos* luminosity, and both the asteroseismic luminosities. It is clear that the errorbars for the asteroseismic luminosity calculated from a $\Delta\nu/2 \approx 34$ μHz are only crossed by high mass models with Z values that are greater than the solar value of $Z \approx 0.02$. It is also evident that the change in the heavy metal content of the models produces the largest change in the position of the model on the HR diagram. There were approximately 10^5 stellar models generated for the model grid. Detailed models (containing information necessary for the pulsation analysis) were output in age steps of 0.05 Gyr from the ZAMS, decreasing the number of models by an order of magnitude. Of those models, 569 fall within the *Hipparcos* luminosity error box (HLEB). The majority of these models have a mass of $\approx 1.6 M_{\odot}$ and a metallicity range from Z $\approx$ 0.014 to Z $\approx$ 0.020. A full listing of all of these models can be found in Table B.1 of Appendix B.

It is also interesting to look at the convective properties of the calculated models since convection has an influence on both the evolutionary status and pulsational properties of a star, as well as implications for the surface chemical inhomogeneities of Ap stars. Figure 3.2 shows the evolution of both the convective core mass and the convective envelope mass for the models shown in the HR diagram (Figure 3.1). Models with higher Z and X have convective cores that last longer than those with the lower Z and X mass fractions. In general, a model with a given mass that has a higher metal content will take longer to reach the same evolutionary state as a model with a lower metal content. The same is true for models with a larger hydrogen mass fraction; although to a lesser extent. In essence, the models with the lower Z content contain more nuclear fuel; increasing energy production in the nuclear burning core. For a given Z, the models with a higher X have less efficient energy transport in the interior because of their smaller convective cores.

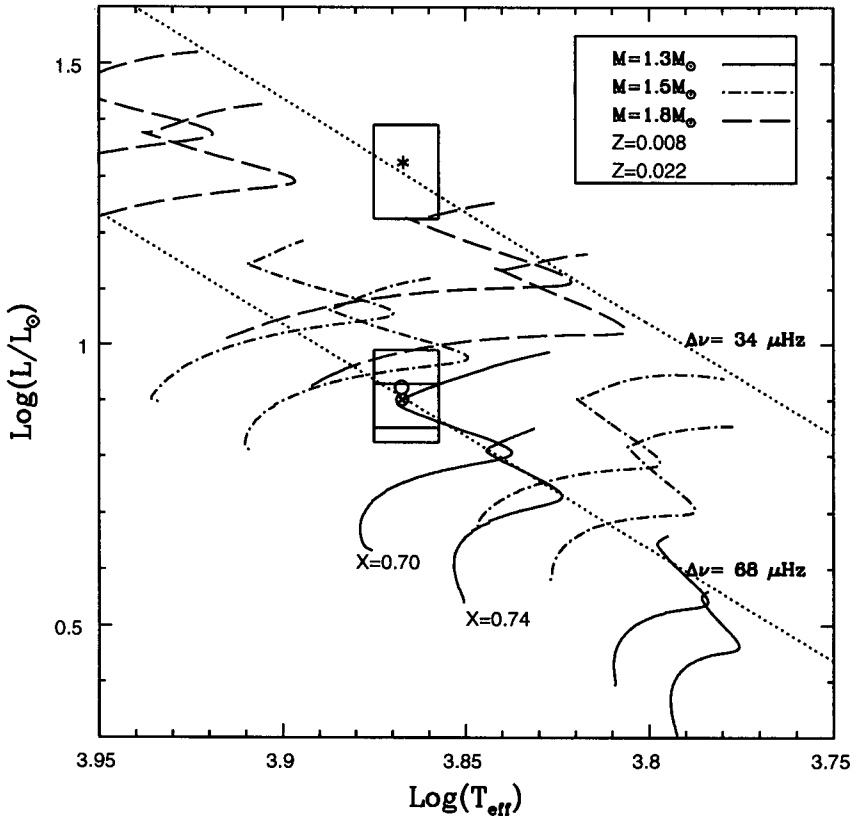

Figure 3.1: A theoretical HR diagram showing the extremes of the parameter space. The inner red error box around ⊗ represents the *Hipparcos* luminosity while the error boxes around the symbols o and $*$ represent the luminosities calculated from a $\Delta\nu$ of 68 μHz and $\Delta\nu/2$ 34 μHz. Also shown are two lines of constant $\Delta\nu$. The metallicity has the greatest effect of the evolutionary status of the stellar model: shifting the tracks toward the lower right for lower Z values.

The mass of the convective envelope is insignificant in these models. In fact, it is only a few of the models shown in Figure 3.2 that envelope convection is a large fraction of the envelope mass ($\approx$ 1% of the model mass). These models may be more efficient at mixing away patches of chemical inhomogeneities; ruling out low mass and high Z models as candidates Ap stars.

For evolutionary models that fall within the HLEB, the spread in $\Delta\nu$ is small. This

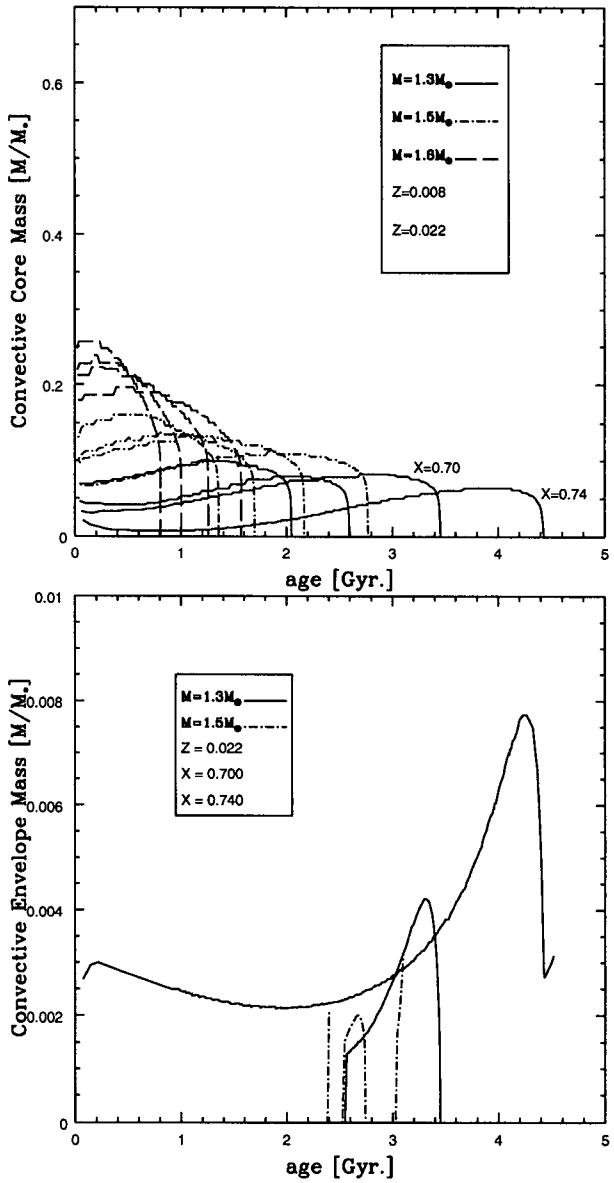

Figure 3.2: The convective core mass (top) and the convective envelope mass (below) as a function of age for the models shown in Figure 3.1. The masses are normalized to the mass of the star. The envelope represents approximately the outer 5% of the model radius.

is illustrated in Figure 3.3. The error bars in Figure 3.3 represent the maximum and minimum values of $\Delta\nu$ and X/Z for a given mass. The only models that do not reproduce

the observed $\Delta\nu$ of 68 μHz are the low Z, $1.3M_{\odot}$ models. Once again, the models that seem to best reproduce the observed large spacing are those with a mass of 1.5 to $1.6M_{\odot}$ and a composition of (X, Z) $\approx$ (0.700, 0.017). It should be noted that the large spacings presented in this plot are calculated directly from the integral definition in Equation 1.7, and not from the spacing of the calculated oscillation frequencies. Spacings calculated using these two methods differ from each other by a few μHz; due to the integral averaging of the sound speed and nonadiabatic effects.

Also shown on the right in Figure 3.3 is the spread in age for each of the models that fall in the HLEB. As is expected, the models with the lowest mass and the highest X/Z ratio are the oldest.

3.2 Pulsation Models

The pulsation calculations are carried out using the nonadiabatic pulsation package of David Guenther; JIG8 (Guenther, 1994). JIG8 solves the six linearized, nonadiabatic equations of nonradial stellar oscillations using the Henyey relaxation method (Henyey et al., 1964). These six complex partial differential equations describe the radial dependence of the vertical and horizontal displacement vectors, the Lagrangian perturbations to the entropy and the radiative luminosity, as well as the Eulerian perturbations to the gravitational potential and its radial derivative. The time dependence of the perturbed quantities is periodic through the function $exp(i\omega t)$; where the ω is the complex eigenfrequency. A complete introduction to both the adiabatic and nonadiabatic, nonradial oscillation equations can be found in Unno et al. (1989).

The nonadiabatic equations are solved using the Eddington approximation (Saio & Cox, 1980). Radiative losses and gains are taken into account through the radiative flux in the entropy equation

$$T\frac{ds}{dt} = \epsilon - \frac{\nabla \cdot \mathbf{F}}{\rho} \tag{3.4}$$

where T, s, t, and ρ are the temperature, entropy, time, and the density, respectively. The vector $\mathbf{F}$ is the sum of the radiative and convective fluxes. If the perturbations to

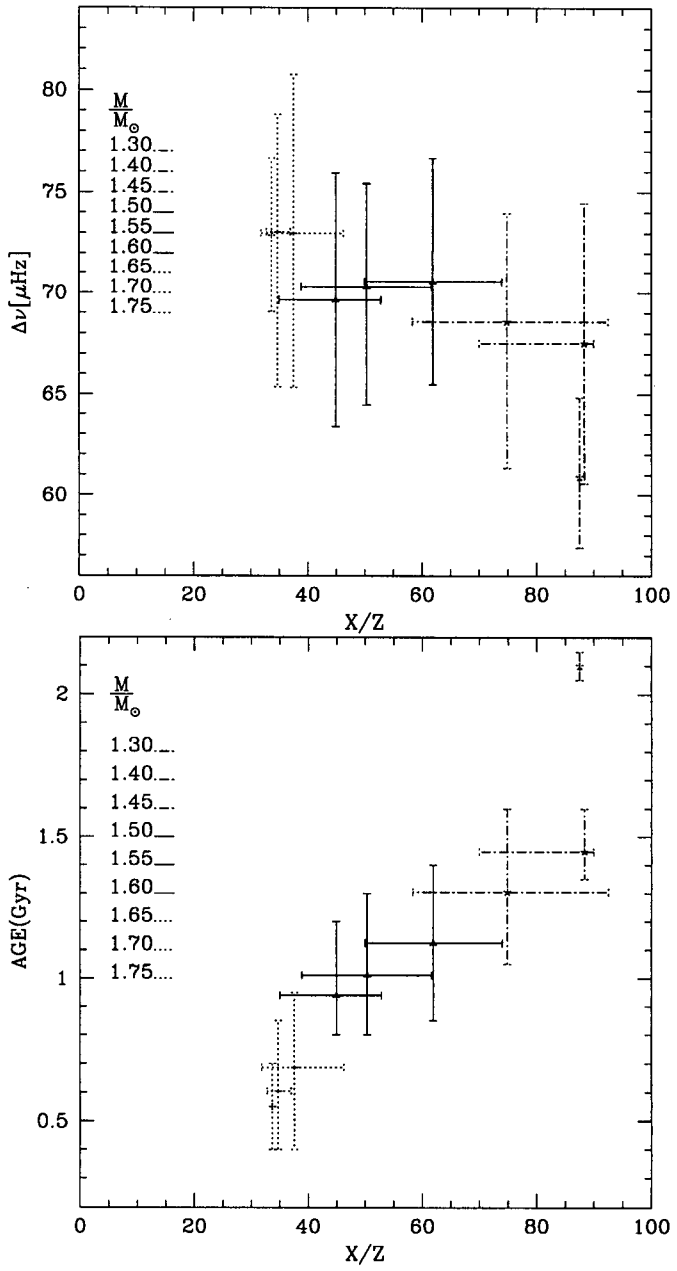

Figure 3.3: The variation of $\Delta\nu$ in μHz (top) and the model age in Gyr (bottom) as a function of the ratio X/Z for models that fall within the *Hipparcos* errorbars. The errorbars on the plot represent the maximum and minimum values for each mass.

the divergence of the convective flux are ignored, **F** becomes; in the Eddington approximation,

$$\mathbf{F}_{rad} = -\frac{4\pi}{3\kappa\rho}\nabla\left[\frac{ac}{4\pi}T^4 + \frac{1}{4\pi\kappa}T\frac{ds}{dt}\right] \tag{3.5}$$

where c is the speed of light, a is the radiation density constant, and κ is the opacity.

The process by which JIG8 obtains the eigenfunctions and frequencies involves five steps outlined by Guenther (1994). After an initial guess of the oscillation frequency and a degree ℓ of the mode, the inner turning point r_t is approximated from the run of sound speed c_s in the model using the relation $c_s(r_t)/r_t = \omega/\sqrt{\ell(\ell+1)}$. The innermost shell is set at radius where the wave number is 10^{-8} times smaller then the value of inner turning point. The adiabatic oscillation equations are solved with the outer mechanical boundary condition removed; providing a discriminant to obtain an initial guess for the adiabatic eigenfunctions (see Unno et al., 1989). Once this initial guess is obtained, the complete linearized adiabatic equations are solved through the relaxation method.

Next, the nonadiabatic oscillation equations are solved with the outer mechanical boundary condition removed using the real eigenfrequency obtained from the adiabatic calculations. An initial guess for the imaginary part of the nonadiabatic frequency is then calculated from the work and kinetic energy integrals by use of the relation $W(R_\odot)/w_k = -4\pi\eta$. Here, η is known as the growth rate of the mode and it is the ratio between the imaginary and real parts of the oscillation frequency. The work and kinetic energy of the mode are given, respectively by

$$W(r) = -4\pi^2 r^2 \mathrm{Im}\left(\delta \mathrm{p}^* \xi_\mathrm{r}\right) \tag{3.6}$$

and

$$w_k = \frac{1}{2}\omega_{ad}^2 \int_0^M \mid \delta\mathbf{r} \mid^2 dm \tag{3.7}$$

where δp^* is the Lagrangian pressure variation, and ξ_r is the vertical part of the radial displacement, $\delta\mathbf{r}$.

Finally, the eigenfunctions and eigenfrequencies obtained in the latter step are used to calculate the solution to the full linearized nonadiabatic nonradial oscillation equations using the Henyey method.

3.2.1 Model Frequencies

Since photometric stellar pulsation observations do not give disc-resolved information, the most important diagnostic of stellar structure comes from the frequency spacing described in Sections 1.4.2 and 1.5. In particular, the large spacing $\Delta\nu$ gives information about the mean density of the star and the second order spacing $\delta^{(2)}$ provides information about the mean molecular weight near the stellar core; i.e., age information. In this section, we present the pulsation results for all stellar models that lie within the HLEB.

The matching of model frequencies to observed frequencies is a subjective process since there are usually more modes excited in models than are observed. The model that reproduces the observed oscillation spectrum of a star is not unique. Recently, however, Guenther & Brown (2004) have developed a method to improve the matching of models to observations. Their method involves minimizing a χ^2 statistic between a large grid of model frequencies and an observed spectrum. Once their model grid is expanded to a more diverse parameter space, this method promises to be a much more quantitative method of mode identification.

The complexity resulting in the large number of oscillation modes excited in a set of stellar models is illustrated in Figure 3.4. The plot of $\Delta\nu$ vs. ν is known as an echelle diagram. An echelle diagram shows ridges of power for a given set of oscillation frequencies. For example, lines of common ℓ run vertically on the diagram, while the higher order p-mode frequencies (larger n values) are sorted horizontally.

In Figure 3.4, the nonadiabatic frequencies and large spacing are plotted for all of the $1.5M_{\odot}$ models with hydrogen mass fraction of 0.700 and metal mass fractions of 0.012 and 0.014. The calculated frequencies alternate between even and odd ℓ values as the order of the modes is increased. The vertical dotted lines are frequencies identified in this study for HR 1217 (see Section 2.5). Selecting the proper stellar model, and even the correct degree of the mode, is very difficult. In fact, even though there are more modes excited for the Z = 0.014 models, there are a significant number of modes calculated from the Z = 0.012 models near $\Delta\nu \approx$ 68 μHz.

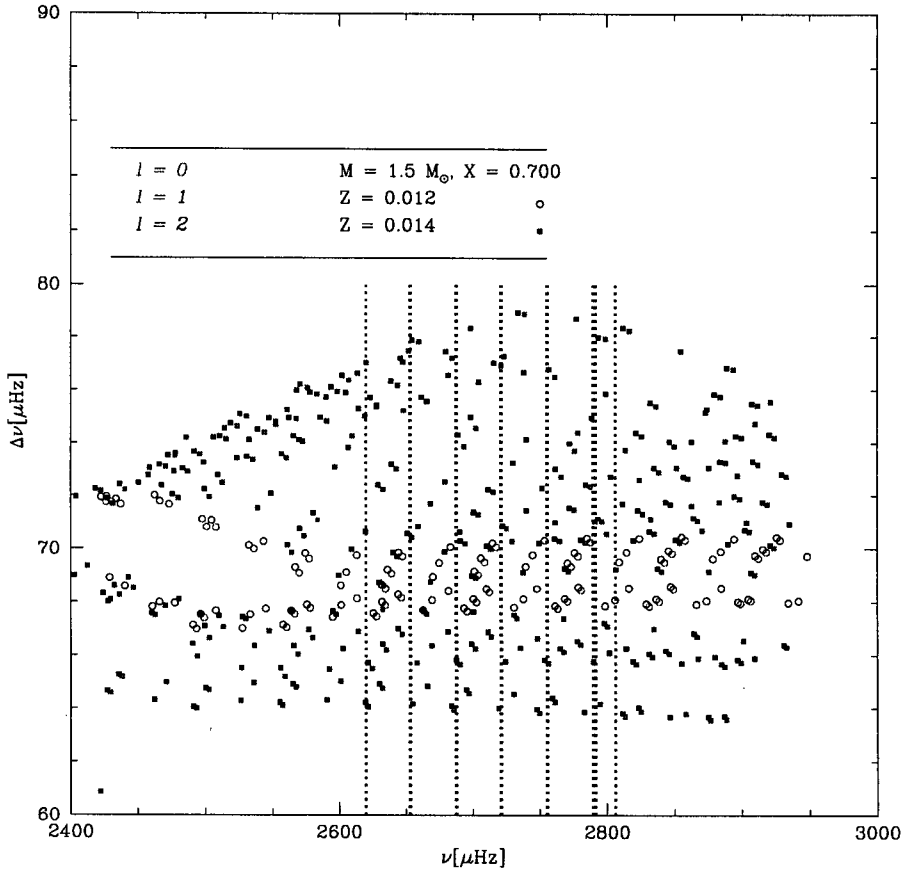

Figure 3.4: An echelle diagram for the $1.5M_{\odot}$ models with X = 0.700, Z = 0.012 and Z = 0.014. The vertical black lines are the frequencies identified for HR 1217 in Section 2.5. Note the modes alternate between both even and odd degrees.

The dependence of the frequency spacing on age and composition is shown in Figure 3.5. The echelle left diagram in this figure show $1.6M_{\odot}$ models with different compositions and ages. The model with Z = 0.016, X = 0.720 and an age of 1.05 Gyr comes closest

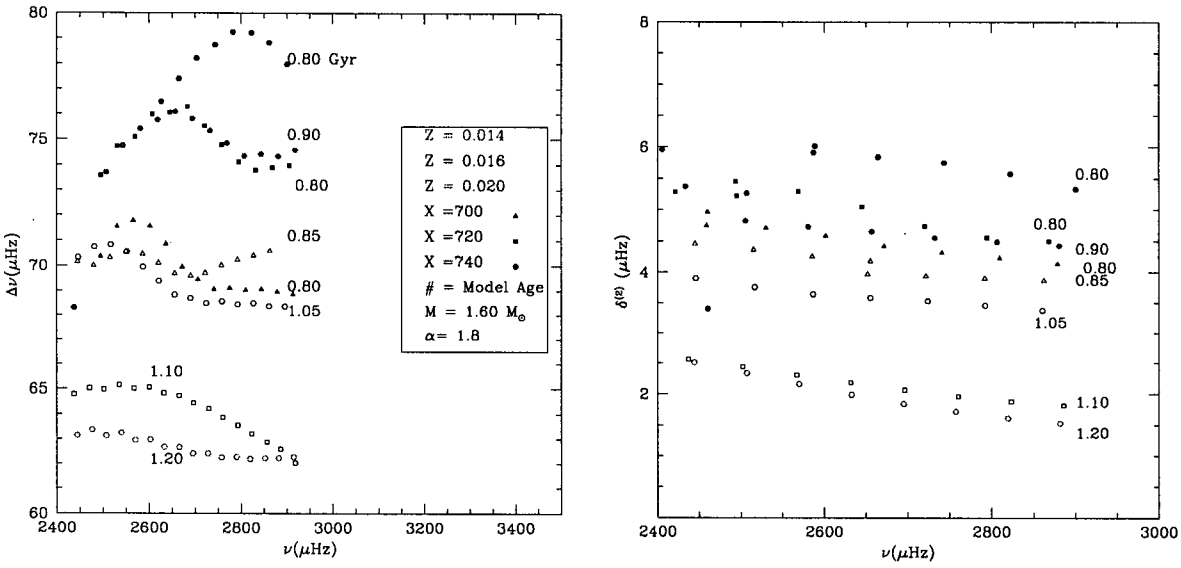

Figure 3.5: On the left, an echelle diagram for $1.6M_{\odot}$ models. These models were selected based on the diversity of the composition and age of the models for this mass. The plot below shows the second order spacing $\delta^{(2)}$ as a function of frequency. The number labels on the plot indicate the models age; where the open symbols are the younger models. The legend for the plot on the left applies to both plots.

to the 68 μHz; however, the younger models with a solar Z of 0.020 and a lower X = 0.700 are also close. The older models show a decrease in the large spacing; indicating an increasing stellar radius (decrease in mean density) as the star evolves through the error box.

The plot on the right in Figure 3.5 shows the second order spacing as a function of frequency. It should be noted that this is less than about 10 μHz for all of the pulsation models calculated for this thesis. This diagnostic diagram shows the same general features

as those in an echelle diagram; however, the models with a small spacing of ≈ 3 μHz may be important for the interpretation of the frequency analysis of Sections 2.5 and 2.6.

Table 3.1: Ten models selected from the 569 that fall within the *Hipparcos* luminosity error bars. These models sample a range of age, composition , mass and mixing length. The full model listing may be found in Appendix A.

Model #	$M_{\odot}$	**Log(T_{eff})**	**Log(L/$L_{\odot}$)**	**Age(Gyrs)**	$\Delta\nu(\mu Hz)$	**X**	**Z**	α
1	1.3	3.86815	0.897607	2.05	64.6873	0.7	0.008	1.6
2	1.3	3.85765	0.928366	2.15	57.6018	0.7	0.008	1.8
3	1.4	3.85757	0.851844	1.4	67.8035	0.7	0.01	1.8
4	1.4	3.86471	0.867916	1.5	68.8062	0.72	0.008	1.8
5	1.5	3.8739	0.865959	0.85	75.6791	0.7	0.014	1.4
6	1.5	3.86287	0.882933	1.2	68.4562	0.72	0.012	1.4
7	1.6	3.86042	0.880244	0.8	70.1876	0.7	0.02	1.8
8	1.6	3.87367	0.900453	0.9	73.6316	0.74	0.014	1.8
9	1.7	3.8715	0.90147	0.5	74.71	0.72	0.022	1.8
10	1.7	3.86716	0.888114	0.6	74.3194	0.74	0.02	1.8

Table 3.1 selects ten models with a range in mass, age, composition and mixing length parameter from the 569 models that fall within the HLEB. Both echelle diagrams and $\delta^{(2)}$ vs. ν diagrams are shown for each of these models in Figures 3.6 and 3.7, respectively.

The echelle diagrams of Figure 3.6 show the same general trends as discussed earlier. The interesting thing to note is that models 6 - 10 slowly increase in $\Delta\nu$. This is caused by both the younger age of the more massive models, as well as, their lower mean densities. The models with the second order spacing of 3 μHz are also either older, or have a mass less than $\approx 1.5 M_{\odot}$.

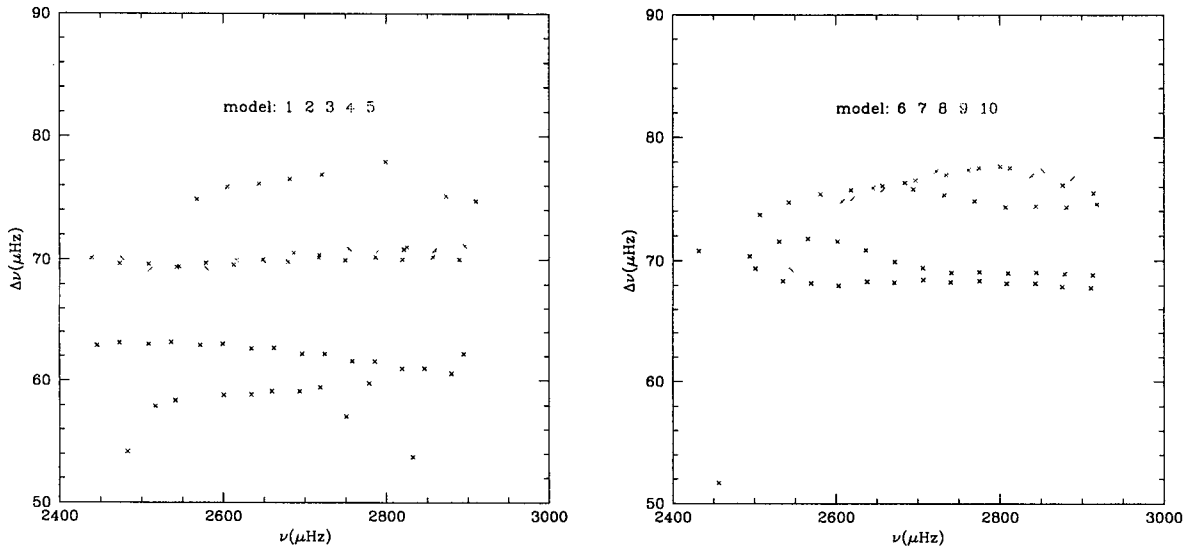

Figure 3.6: Echelle diagrams for the models listed in Table 3.1. The model number is listed at the top of the diagram.

3.3 Magnetic Effects

The effects of the magnetic field on both the oscillation frequencies and the eigenfunctions have been described by a number of authors (e.g., Shibahashi & Takata, 1993, Dziembowski & Goode, 1996, Bigot et al., 2000, and Cunha & Gough, 2000). In the case of roAp stars, pressures induced by the magnetic field dominate over gas pressure near the surface of the star. The usual perturbation techniques for calculating the magnetic effects on stellar oscillations are no longer valid. However, there has been recent success in the interpretation of roAp oscillations in terms of a variational principle (Cunha, 2001). By only calculating the perturbed eigenmodes and not the eigenfunctions, the method of Cunha & Gough (2000) is an attractive alternative to a perturbation analysis of magneto-acoustic modes.

The work of Cunha & Gough (2000) follows from that of Campbell & Papaloizou

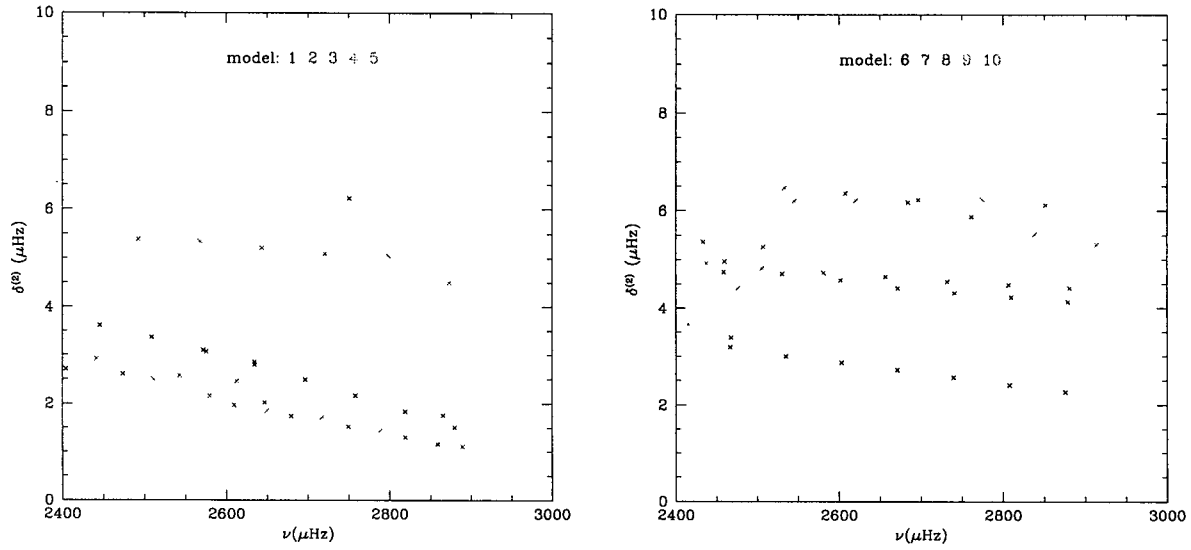

Figure 3.7: Second order spacing diagrams for the models listed in Table 3.1. The model number is listed at the top of the diagram.

(1986). These authors divide the star into a thin outer boundary layer and the interior. In the boundary layer, the Lorentz forces are comparable to; or larger than, the gas pressure, while in the interior the field is essentially force free.

Since the magnetic boundary layer is thin, a plane-parallel approximation may be used. It is also assumed that the effects of the magnetic field can be calculated locally at each latitude. In this case, the field only varies in the vertical direction and has components $\mathbf{B} = (B_x, 0, B_z)$. The magneto-acoustic waves are described using a horizontal wavenumber $\mathbf{k} = (k_x, k_y, 0)$. With this information, the adiabatic, magnetically non-diffusive, pulsation equations may then be written as (Campbell & Papaloizou, 1986, and Cunha & Gough, 2000)

$$-\omega^2 \rho u = i \mid \mathbf{k} \mid W + (\mathbf{B} \cdot \nabla)^2 \frac{u}{\mu_0} - \frac{k_x B_x}{\mu_0 \mid \mathbf{k} \mid} (\mathbf{B} \cdot \nabla)(\nabla \cdot \xi) \tag{3.8}$$

$$-\omega^2 \rho v = (\mathbf{B}\cdot\nabla)^2 \frac{v}{\mu_0} + \frac{k_y B_x}{\mu_0 \mid \mathbf{k} \mid} (\mathbf{B}\cdot\nabla)(\nabla\cdot\xi) \tag{3.9}$$

$$-\omega^2 \rho \xi_z = \frac{\partial W}{\partial z} - g\nabla\cdot(\rho\xi) - \frac{B_z}{\mu_0}[(\mathbf{B}\cdot\nabla)(\nabla\cdot\xi)] + (\mathbf{B}\cdot\nabla)^2 \frac{\xi_z}{\mu_0} \tag{3.10}$$

where

$$W = \xi\cdot\nabla p + \left(\gamma p + \frac{B^2}{\mu 0}\right)(\nabla\cdot\xi) - \frac{(\mathbf{B}\cdot\nabla)(\mathbf{B}\cdot\xi)}{\mu_0} \tag{3.11}$$

and

$$g = \frac{1}{\rho}\frac{dp}{dz} \tag{3.12}$$

In the above relations, the displacement vector ξ is decomposed into a vertical component $\xi_z = \xi \cdot \mathbf{e_z}$, a component that is perpendicular to the wavenumber $v = \xi\cdot(e_z \times \mathbf{k})/ \mid \mathbf{k} \mid$, and a component that is parallel to the wavenumber $u = (\xi \cdot \mathbf{k})/ \mid \mathbf{k} \mid$. The local gravitational acceleration is denoted by g and the first adiabatic exponent is γ. All other symbols have their usual meanings.

In the deep interior, a magneto-acoustic mode completely decouples into a pure Alfvénic mode and a pure acoustic mode. This was verified analytically by Roberts & Soward (1983) and numerically by Campbell & Papaloizou (1986). Thus, in the JWKB approximation, the magnetic modes in the interior may be described by the functions (cf. Cunha & Gough 2000)

$$(v_{mz}, u_{mz}) \backsim \rho^{-1/4}(C, D) exp\left[i\int_0^z \left(\frac{\mu_0\rho\omega^2}{B_z^2}\right)^2 dz - i\frac{k_x B_x z}{B_z}\right] + \rho^{-1/4}(C_+, D_+) exp\left[-i\int_0^z \left(\frac{\mu_0\rho\omega^2}{B_z^2}\right)^2 dz - i\frac{k_x B_x z}{B_z}\right] \tag{3.13}$$

where C, D, C_+, and D_+ are complex constants. The inward propagating Alfvén waves are expected to dissipate before they are reflected back toward the surface of the star (Roberts & Soward, 1983). With this in mind, the constants C_+ and D_+ in Equation 3.13 may then be set to zero to assure that no outwardly propagating magnetic waves occur in the interior.

In the interior, the vertical component of the uncoupled modes is essentially acoustic. The amplitude of this vertical mode may be represented asymptotically by (cf. Cunha

& Gough 2000)

$$\xi_z \backsim \frac{A\varkappa^{1/2}}{\rho^{1/2}} \cos\left(\int_z^{z^*} \varkappa dz + \delta_p\right) \tag{3.14}$$

were δ_p is a phase and $\varkappa$ is the vertical acoustic wavenumber. The coordinate z and z^* represent the depth in the boundary layer and the position of the base of the boundary layer, respectively.

The numerical solutions of the system of Equations 3.8 to 3.10 are matched to the asymptotic relations 3.13 and 3.14 at each latitude to obtain values for the magnetic phases δ_p. The purely acoustic case, i.e, $\mathbf{B} = 0$ in Equations 3.8 to 3.10, is also matched onto the asymptotic relations to obtain the unperturbed phases δ_{p0}. Phase shifts $\Delta\delta_p$ are then obtained from the difference between these 2 phases at each latitude.

With the above information, the variational method of Cunha & Gough (2000) can be used to estimate the first-order frequency shifts of the eigenmodes caused by a magnetic field. The frequency shifts may be calculated from

$$\frac{\Delta\omega}{\omega_0} \backsimeq -\frac{\overline{\Delta\delta_p}}{\omega_0^2 \int_{r_1}^{R^*} c_s^{-2} \varkappa_0^{-1} dr} \tag{3.15}$$

where the average of the phase shifts $\Delta\delta_p$ over a sphere is

$$\overline{\Delta\delta_p} = \frac{\int_0^\pi \Delta\delta_p (Y_\ell^m)^2 \sin\theta d\theta}{\int_0^\pi (Y_\ell^m)^2 \sin\theta d\theta} \tag{3.16}$$

The quantities with a subscript of zero are those expected in the case of no magnetic field. A complete description of the numerical procedure used to calculate the frequency shifts is outlined in the appendices of Cunha & Gough (2000).

3.3.1 The Frequency Perturbations

The perturbation to the acoustic oscillations are calculated using an adapted version of the code used by Cunha & Gough (2000). This new version of the code was updated by Cunha (private communication, 2003) to read the output from the evolutionary models presented in Section 3.1. Frequency shifts were calculated for models 1 to 10 in Table 3.1 using Equation 3.15. The magnetic perturbations to frequencies from 900 to 3100

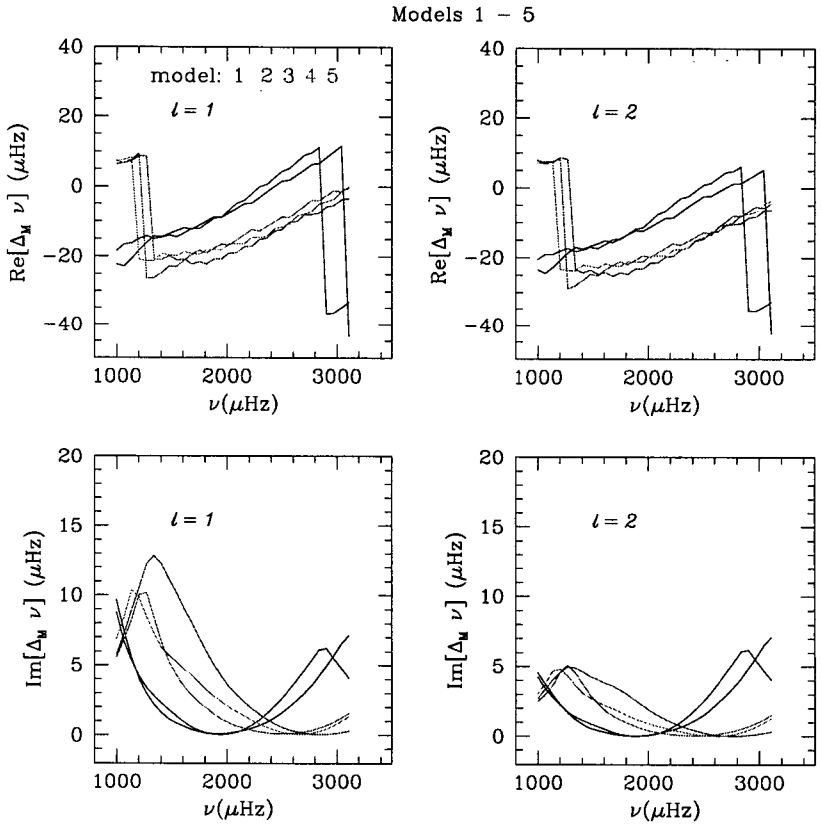

Figure 3.8: The magnetic perturbations calculated for models 1 to 5 using a variational principle. The upper plots show the real frequency shift for modes with degrees $\ell = 1$ (left) and $\ell = 2$ (right). The lower plots show the imaginary part of the frequency shifts for the same degrees.

μHz are shown in Figures 3.8 and 3.9 assuming a dipolar magnetic field with a polar strength of 4.0 kG. This frequency range and magnetic field strength is consistent with measurements of HR 1217 (see Section 1.5).

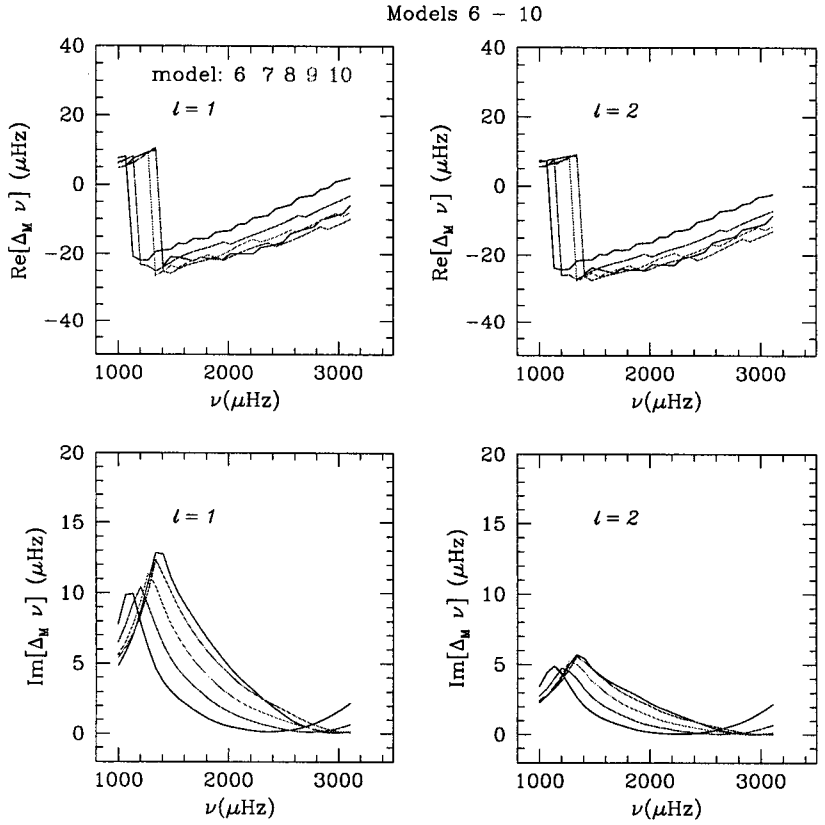

Figure 3.9: The magnetic perturbations calculated for models 6 to 10 using a variational principle. The upper plots show the real frequency shift for modes with degrees $\ell = 1$ (left) and $\ell = 2$ (right). The lower plots show the imaginary part of the frequency shifts for the same degrees.

Each of Figures 3.8 and 3.9 show the real and the imaginary frequency shifts for modes with a degree of $\ell = 1$ and 2. Note that there is very little difference in the real frequency shifts for modes of different degree. The imaginary part of the $\ell = 2$ modes

are; however, clearly lower. This was also shown for the case of a polytrope stellar model by Cunha & Gough (2000).

In general, if the imaginary part of the frequency is positive, the magneto-acoustic mode loses energy. The smaller amplitude of the imaginary part for the $\ell = 2$ modes suggest that they are much less susceptible to damping from the magnetic field. This effect depends on the geometry of the mode and the magnetic field. Cunha & Gough (2000) show that the maximum energy loss of a magneto-acoustic mode occurs approximately at the latitude where $B_z B_x$ is a maximum. This occurs at 45° for a dipolar magnetic field. Modes of higher degree ℓ decrease in amplitude as they approach the equator more quickly than modes of lower degree. When the phase shifts are averaged over a sphere, the net effect is a smaller imaginary frequency shift for modes of larger ℓ. Simply put, these modes have lower amplitudes near the latitude where the maximum of energy loss occurs. It is believed that the resulting frequency shifts are caused by energy loss through the coupling of inwardly propagating magnetic slow waves and the acoustic modes (Cunha & Gough, 2000).

The frequency jumps change very little between the models. This makes it difficult to use the magnetic perturbations as a discriminant between different evolutionary models. It is important to notice the frequency shifts between modes of different degrees are of the same order as the second-order spacing described in Section 3.2.1. This may hamper efforts to use an observed $\delta^{(2)}$ as a diagnostic of stellar structure (Dziembowski & Goode, 1996).

Chapter 4

Discussion and Conclusions

Early photometric observations on the roAp star HR 1217 (e.g., Kurtz et al., 1989) showed a pulsation pattern that was characteristic of high-order p-modes observed in the Sun (see Figure 1.4). The main differences between the solar oscillation spectrum and that of HR 1217 were the observed amplitudes and frequency spacings. In general, the amplitudes of the roAp stars are greater than the solar oscillation amplitudes. Frequency spacings suggest a $\Delta\nu$ of approximately 135 μHz for the sun (e.g., Aindow et al., 1988), while the inferred large spacing for HR 1217 is half this value at 68 μHz, consistent with a lower mean density of the Ap star. The data reduction presented in Chapter 2 for the XCOV20 campaign on HR 1217 yields results that are consistent with those obtained by (Kurtz et al., 1989) in the 1986 campaign. The two notable exceptions are the amplitudes of the oscillation modes (see Figure 2.7) and the new frequencies at 2788.94 and 2791.57 μHz (see Table 2.1). The latter of these new frequencies was also identified in a preliminary reduction of the XCOV20 data by Kurtz et al. (2002).

The amplitudes of the third and fourth frequencies identified in the 1986 data differ from those identified in this study (see Section 2.5) by $\approx$ 60% and 40% respectively. Although the amplitudes between the XCOV20 data and the 1986 data are clearly different, the net amplitude difference (defined by $\sum[A_{2000} - A_{1986}]$) is only -0.07 ± 0.192 mmag. This suggests there is an exchange of power (amplitude squared) between the observed modes while the net power is conserved. The exact mechanism governing the exchange of power between individual modes is not known. It is also interesting that the net frequency difference between the common frequencies identified in both data sets is only $\sum[\nu_{2000} - \nu_{1986}] = 0.56 \pm 0.96$ μHz. This corresponds to an average frequency

difference of 0.09 ± 0.96 μHz. The persistence of these observed frequencies suggests that the mode lifetimes in HR 1217 are stable over the 14 year time gap between observations. Mode selection and lifetime are particularly interesting in roAp stars. For example, the roAp star HR 3831 exhibits oscillation modes that are stable over 20 years of observations (Kurtz et al., 1997) while the roAp star HD 60435 shows some mode lifetimes of less than 7 days (Matthews et al., 1987). A long baseline for observations on other roAp stars would be invaluable to our understanding of mode excitation; which is still uncertain (e.g., Balmforth et al., 2001).

The frequency analysis presented in Sections 2.5 and 2.6 suggest that the amplitude limit at which frequencies can confidently be identified from the current time-series reduction has been reached. Once each of the 21 frequencies had been removed by the unweighted data analysis, the residuals improved by less than $\approx 0.1\%$ (see Figure 2.8). The improvement between the unweighted frequency analysis and each of the weighted frequency reductions presented in Section 2.6 is also less than 5% (see Figure 2.10). While the weighted noise levels in the Fourier spectra of Figures 2.11 and 2.12 are clearly lower than the noise of Figure 2.6, the general results are the same. It is not clear how the weighting of the frequencies affects the determination of the confidence levels discussed in Section 2.5.1. Regardless, almost all of the frequencies can be described by a triplet fine structure. The exception is the frequency ν_7. Even when ν_7 is forced to be fitted as a rotationally split triplet, the amplitude of one of the components is always less than 0.035 mmag (see Tables C.1 and C.2). This is always below the noise; even when it is weighted. A doublet structure is not predicted by the oblique pulsator model.

It should be noted that least-squares fits calculated using *Period*98 always converged close to the same amplitudes, frequencies and phases. This is illustrated in Tables C.5 through C.10 of Appendix C. The frequencies, amplitudes, and phases were averaged and a standard error of the mean was calculated for frequency solutions from Table 2.3 with the same identified frequencies. The standard error on the frequencies, amplitudes and phases are of the order 10^{-6} mHz, 10^{-2} mmag, and 10^{-2} radians. This is a testament to the robustness of *Period*98.

The absence of the frequency $\nu(old)$ (see Table 2.1) in the 1986 data is explained by Cunha (2001) as strong magnetic damping of the oscillation mode. The models presented in Section 3.3.1 (see Figures 3.8 and 3.9) are in agreement with her results for a polytrope stellar model. These models show an increase of damping toward the seventh frequency in Table 2.1 (2806.57 μHz). This may explain the observed spacing between frequencies 6 and 7 of $\approx$ 15 μHz; -20 μHz away from the expected value.

As discussed in Section 3.3.1, the magnetic damping of modes decreases with increasing degree (larger ℓ values). This is a consequence of the mode and magnetic field geometry as well as the weighting of the modes by the variational method. The modes with the larger ℓ values have smaller amplitudes near latitudes of maximum magnetic damping. The net damping of the higher degree modes is less when the average of the magnetic effects is calculated for all latitudes. Damping increases with increasing imaginary frequency shift. The imaginary shifts shown in Figures 3.8 and 3.9 are less for the $\ell = 2$ modes than the corresponding $\ell = 1$ modes.

The spacing between both of the new modes ($\nu(old)$ and $\nu(new)$) is approximately 2.63 μHz. This is consistent with the second-order frequency spacings calculated for the stellar models in Section 3.2.1 (see Figures 3.5 and 3.7). If this is a small spacing, Equation 1.10 shows; by definition, that the modes differ in degree by 2. Consider a single mode of low degree with an amplitude that is stabilized below observable levels through magnetic damping. If this mode exchanges power between itself and a mode of larger degree, the amplitude of the new mode may grow to observable levels because it is less damped by magneto-acoustic interactions. This conjecture is supported by the observation of two closely spaced modes in the XCOV20 data while there is no evidence for similar modes in the 1986 data set. However, this is difficult to predict empirically since the mechanisms for mode excitation and damping are still uncertain.

While the oblique pulsator models discussed in Section 1.4.3 are not used to predict the amplitude asymmetries observed in this work, a prediction of the models is tested using the fine frequency spacing of the XCOV20 data. The oblique pulsator model, in all its forms, predicts that the frequencies are exactly split by the rotation frequency of

the star. If the modes are described instead by traveling waves ($m \neq 0$) discussed in Section 1.4.1, one would expect departures from the exact spacing because of the Ledoux constant of Equation 1.5. By averaging the difference between the fine spacings $\delta\nu$ of Table 2.1 and the rotation frequency of 9.2897×10^{-4} mHz (the average rotation period derived from Bagnulo et al. (1995) and Kurtz & Marang (1987); see Section 2.6), the Ledoux constant is estimated to be $7.2 \times 10^{-5} \pm 11\%$. This is still 2 orders of magnitude lower than the value of $C_{n,\ell} \approx 10^{-3}$ calculated by Shibahashi & Takata (1993). It is also in agreement with the value of $C_{n,\ell} \lesssim 0.0006$ obtained by Kurtz et al. (1989) from the fine structure observed in the 1986 data set. Thus, it is unlikely that the observed rotational splitting is described by Equation 1.5.

The diagnostic power of a second-order spacing for the roAp stars has been questioned by some authors (e.g., Dziembowski & Goode, 1996, and Balmforth et al., 2001). The reason is that the magnetic perturbations between modes of differing degree is of the same order as the small spacings. However, it is still interesting to draw some conclusions from the calculated small spacings of Section 3.2.1 in light of the possible observed small spacing of 2.63 μHz between frequencies $\nu(old)$ and $\nu(new)$. In particular, the evolutionary models that reproduce the observed second-order spacing of 2.63 μHz have a mass of $\approx 1.6 M_{\odot}$ and a composition of (X, Z) $\approx$ (0.720, 0.017) (see Figures 3.5 and 3.7). If the calculated large spacing is also compared to the observed value of 68 μHz, the evolutionary model properties would be consistent with those from the small spacing estimates; i.e, a sub-solar Z, solar X, and a mass of approximately $1.6 M_{\odot}$ (see Figures 3.5 and 3.6). These results are also confirmed by the work of Cunha et al. (2003). However, no one oscillation model agrees unambiguously with the observed oscillation spectrum of HR 1217.

Models with a lower global metallicity confirm the results of Lebreton et al. (1999). It is usually assumed that stars in the solar neighborhood, like HR 1217, have a solar metallicity. Lebreton et al. (1999) calculate a metallicity range of $-1 < [Fe/H] < 0.3$ for a sample of stars with distances less than 30 pc. While there is no way to absolutely determine the interior metal content of any star from the observed surface abundances,

it is especially difficult for the Ap stars because of there peculiar spectral features. The old assumption of solar metallicity models for nearby stars may have to be revised.

The models that fall within the luminosity errorbox defined by the *Hipparcos* parallax with a mass less than $1.5M_{\odot}$ and a metallicity greater than solar exhibit large envelope convection. In the case of a $1.3M_{\odot}$ model with composition (X, Z) = (0.740, 0.022), the envelope is almost completely convective by the time it enters the defined errorbox. These models have left the main sequence and are approaching the base of the red giant branch. While small convective zones ($\ll 0.1\%\ M_{\star}$) exist in other models, the convective envelope models presented in Figure 3.2 can clearly be ruled out as Ap model candidates. The reason being that any surface inhomogeneities would be mixed away by the on-set of such deep surface convective zones.

Models presented in this study are a valuable asset for constraining the physics of Ap and roAp stars. Future improvements will include better approximations to the model atmospheres. Specifically, the use of an Eddington grey atmosphere in the model calculations predicts an isothermal acoustic cut-off frequency that is below the observed frequencies for HR 1217. Modifications to the T-τ relations for roAp stars have been used by Gautschy et al. (1998) and Audard et al. (1998). In the first case, a T-τ was artificially modified to cause a steeper temperature gradient near the stellar surface; mimicking the effect of a chromosphere. However, Audard et al. (1998) use model atmospheres with a surface composition specific to HR 1217 but with a global Z = 0.02. Both groups were successful in raising the acoustic cut-off so that the calculated frequencies and the observed frequencies were in agreement.

Model atmospheres have been calculated by Werner Weiss of the University of Vienna (private communication) for an HR 1217 surface composition (Ryabchikova et al., 1997) and we are currently adapting them so they can be used with YREC7. There are two improvements over the earlier work of Audard et al. (1998). First, the evolutionary models will not be restricted to a constant surface gravity. The effect this will have is expected to be small; however, it is consistent with an evolving sequence of stellar models. The second, and more important, is the addition of multiple compositions that

reflect the observed change in abundance patterns as HR 1217 rotates. Thus, a number of independent evolutionary tracks will be calculated allowing us to model the frequencies with an azimuthal dependence. These new models will then also be subject to the magnetic frequency perturbation analysis presented in Section 3.3.

The quality of photometric data of HR 1217 is also expected to improve in the near future since the MOST[1] (Walker et al., 2003, and Matthews et al., 2000) space seismology micro-satellite (aperture = 15 cm) was successfully launched on June 30, 2003. This project is Canada's first space telescope and its primary functions are asteroseismology and the detection of reflected light from exoplanets. MOST is already surpassing its expected performance and viewing targets with a photometric precision of $\approx$ a few parts-per-million in the frequency range relevant for roAp stars and with duty cycles of 99% (Matthews, private communication). As a comparison, the XCOV20 data covered a duty cycle of $\approx$ 33%; making it a highly successful ground based study, and reached a noise level of $\approx$ 0.1 mmag; almost 2 orders of magnitude greater than MOST.

In late 2004, MOST will observe HR 1217 for just over 3 weeks. This should be sufficient to cover 3 rotation periods of the star providing an adequate time-base for high frequency resolution. Since HR 1217 will be observed only 4 years after the XCOV20 observations, there could be interesting results on the mode lifetimes of the star. The new models presented in this thesis combined with improved observations from space should shed new light on the physics governing the structure and evolution of Ap and roAp stars.

[1]Microvariability & Oscillations of STars *or* Microvariabilité et Oscillations STellaire

Bibliography

Aindow, A., Elsworth, Y. P., Isaak, G. R., McLeod, C. P., New, R., & van der Raay, H. B. 1988, in Seismology of the Sun and Sun-like Stars, ESA SP-286, 157

Alexander, D. R. & Ferguson, J. W. 1994, ApJ, 437, 879

Alvarez, M., Hernandez, M. M., Michel, E., Jiang, S. Y., Belmonte, J. A., Chevreton, M., Massacrier, G., Liu, Y. Y., Li, Z. P., Goupil, M. J., Cortes, T. R., Mangeney, A., Dolez, N., Valtier, J. C., Vidal, I., Sperl, M., & Talon, S. 1998, A & A, 340, 149

Audard, N., Kupka, F., Morel, P., Provost, J., & Weiss, W. W. 1998, A & A, 335, 954

Böhm-Vitense, E. 1958, Zeitschrift fur Astrophysics, 46, 108

Babel, J. & Michaud, G. 1991, A & A, 241, 493

Bagnulo, S. 1998, Contributions of the Astronomical Observatory Skalnate Pleso, 27, 431

Bagnulo, S., Landi degl'Innocenti, E., Landolfi, M., & Leroy, J. L. 1995, A & A, 295, 459

Bahcall, J. N., Pinsonneault, M. H., & Basu, S. 2001, ApJ, 555, 990

Balmforth, N. J., Cunha, M. S., Dolez, N., Gough, D. O., & Vauclair, S. 2001, MNRAS, 323, 362

Bigot, L. & Dziembowski, W. 2002, A & A, 391, 235

Bigot, L., Provost, J., Berthomieu, G., Dziembowski, W. A., & Goode, P. R. 2000, A & A, 356, 218

Breger, M., Handler, G., Garrido, R., Audard, N., Zima, W., Paparó, M., Beichbuchner, F., Zhi-Ping, L., Shi-Yang, J., Zong-Li, L., Ai-Ying, Z., Pikall, H., Stankov, A., Guzik, J. A., Sperl, M., Krzesinski, J., Ogloza, W., Pajdosz, G., Zola, S., Thomassen, T., Solheim, J.-E., Serkowitsch, E., Reegen, P., Rumpf, T., Schmalwieser, A., & Montgomery, M. H. 1999, A & A, 349, 225

Breger, M., Stich, J., Garrido, R., Martin, B., Jiang, S. Y., Li, Z. P., Hube, D. P., Ostermann, W., Paparo, M., & Scheck, M. 1993, A & A, 271, 482

Bressan, A., Chiosi, C., & Fagotto, F. 1994, ApJS, 94, 63

Campbell, C. G. & Papaloizou, J. C. B. 1986, MNRAS, 220, 577

Christensen-Dalsgaard, J. 2002, Reviews of Modern Physics, 74, 1073

Cunha, M. S. 2001, MNRAS, 325, 373

Cunha, M. S., Fernandes, J. M. M. B., & Monteiro, M. J. P. F. G. 2003, MNRAS, 343, 831

Cunha, M. S. & Gough, D. 2000, MNRAS, 319, 1020

Dziembowski, W. & Goode, P. R. 1985, ApJ, 296, L27

Dziembowski, W. A. & Goode, P. R. 1996, ApJ, 458, 338

Frandsen, S., Pigulski, A., Nuspl, J., Breger, M., Belmonte, J. A., Dall, T. H., Arentoft, T., Sterken, C., Medupe, T., Gupta, S. K., Pinheiro, F. J. G., Monteiro, M. J. P. F. G., Barban, C., Chevreton, M., Michel, E., Benko, J. M., Barcza, S., Szabó, R., Kołaczkowski, Z., Kopacki, G., & Udovichenko, S. N. 2001, A & A, 376, 175

Gabriel, K., Noels, A., Scuflaire, R., & Mathys, G. 1985, A & A, 143, 206

Gautschy, A., Saio, H., & Harzenmoser, H. 1998, MNRAS, 301, 31

Girish, V., Seetha, S., Martinez, P., Joshi, S., Ashoka, B. N., Kurtz, D. W., Chaubey, U. S., Gupta, S. K., & Sagar, R. 2001, A & A, 380, 142

Grevesse, N., Noels, A., & Sauval, A. J. 1996, in ASP Conf. Ser. 99: Cosmic Abundances, 117

Guenther, D. B. 1994, ApJ, 422, 400

Guenther, D. B. & Brown, K. I. T. 2004, ApJ, 600, 419

Guenther, D. B. & Demarque, P. 1997, ApJ, 484, 937

Guenther, D. B., Demarque, P., Kim, Y.-C., & Pinsonneault, M. H. 1992, ApJ, 387, 372

Handler, G. 2003, Baltic Astronomy, 12, 253

Henyey, L. G., Forbes, J. E., & Gould, N. L. 1964, ApJ, 139, 306

Hiltner, W. A. 1962, Astronomical techniques. (Chicago, University Press [1962])

Iglesias, C. A. & Rogers, F. J. 1996, ApJ, 464, 943

Kawaler, S. D., O'Brien, M. S., Clemens, J. C., Nather, R. E., Winget, D. E., Watson, T. K., Yanagida, K., Dixson, J. S., Bradley, P. A., Wood, M. A., Sullivan, D. J., Kleinman, S. J., Meistas, E., Leibowitz, E. M., Moskalik, P., Zola, S., Pajdosz, G., Krzesinski, J., Solheim, J.-E., Bruvold, A., O'Donoghue, D., Katz, M., Vauclair, G., Dolez, N., Chevreton, M., Barstow, M. A., Kanaan, A., Kepler, S. O., Giovannini, O., Provencal, J. L., & Hansen, C. J. 1995, ApJ, 450, 350

Kippenhahn, R. & Weigert, A. 1994, Stellar Structure and Evolution (Stellar Structure and Evolution, XVI, 468 pp. 192 figs.. Springer-Verlag Berlin Heidelberg New York. Also Astronomy and Astrophysics Library)

Kleinman, S. J., Nather, R. E., & Phillips, T. 1996, PASP, 108, 356

Kurtz, D. & Wegner, G. 1979, ApJ, 232, 510

Kurtz, D. W. 1978, Informational Bulletin on Variable Stars, 1436, 1

—. 1982, MNRAS, 200, 807

—. 1990, ARA & A, 28, 607

Kurtz, D. W., Kawaler, S. D., Riddle, R. L., Reed, M. D., Cunha, M. S., Wood, M., Silvestri, N., Watson, T. K., Dolez, N., Moskalik, P., Zola, S., Pallier, E., Guzik, J. A., Metcalfe, T. S., Mukadam, A., Nather, R. E., Winget, D. E., Sullivan, D. J., Sullivan, T., Sekiguchi, K., Jiang, X. J., Shobbrook, R. R., Birch, P. V., Ashoka, B. N., Seetha, S., Joshi, S., Girish, V., O'Donoghue, D., Handler, G., Mueller, M., Gonzalez Perez, J. M., Solheim, J. E., Johannessen, F., Ulla, A., Kepler, S. O., Kanaan, A., da Costa, A., Fraga, L., Giovannini, O., Matthews, J. M., Cameron, C., Vauclair, G., Nitta, A., & Kleinman, S. J. 2003, Baltic Astronomy, 12, 105

Kurtz, D. W., Kawaler, S. D., Riddle, R. L., Reed, M. D., Cunha, M. S., Wood, M., Silvestri, N., Watson, T. K., Dolez, N., Moskalik, P., Zola, S., Pallier, E., Guzik, J. A., Metcalfe, T. S., Mukadam, A. S., Nather, R. E., Winget, D. E., Sullivan, D. J., Sullivan, T., Sekiguchi, K., Jiang, X., Shobbrook, R., Ashoka, B. N., Seetha, S., Joshi, S., O'Donoghue, D., Handler, G., Mueller, M., Gonzalez Perez, J. M., Solheim, J.-E., Johannessen, F., Ulla, A., Kepler, S. O., Kanaan, A., da Costa, A., Fraga, L., Giovannini, O., & Matthews, J. M. 2002, MNRAS, 330, L57

Kurtz, D. W. & Marang, F. 1987, MNRAS, 229, 285

Kurtz, D. W. & Martinez, P. 2000, Baltic Astronomy, 9, 253

Kurtz, D. W., Matthews, J. M., Martinez, P., Seeman, J., Cropper, M., Clemens, J. C., Kreidl, T. J., Sterken, C., Schneider, H., Weiss, W. W., Kawaler, S. D., & Kepler, S. O. 1989, MNRAS, 240, 881

Kurtz, D. W. & Seeman, J. 1983, MNRAS, 205, 11

Kurtz, D. W., van Wyk, F., Roberts, G., Marang, F., Handler, G., Medupe, R., & Kilkenny, D. 1997, MNRAS, 287, 69

Kuschnig, R., Weiss, W. W., Gruber, R., Bely, P. Y., & Jenkner, H. 1997, A & A, 328, 544

Landstreet, J. D. 1992a, A & AR, 4, 35

—. 1992b, Reviews of Modern Astronomy, 5, 105

Landstreet, J. D. 1993, in ASP Conf. Ser. 44: IAU Colloq. 138: Peculiar versus Normal Phenomena in A-type and Related Stars, 218

Lebreton, Y., Perrin, M. N., Cayrel, R., Baglin, A., & Fernandes, J. 1999, A & A, 350, 587

Ledoux, P. 1951, ApJ, 114, 373

Leibacher, J. W. & Stein, R. F. 1971, Astrophys. Lett., 7, 191

Leighton, R. B., Noyes, R. W., & Simon, G. W. 1962, ApJ, 135, 474

Leroy, J. L., Landstreet, J. D., Deglinnocenti, E. L., & Landolfi, M. 1993, in ASP Conf. Ser. 44: IAU Colloq. 138: Peculiar versus Normal Phenomena in A-type and Related Stars, 274

Loumos, G. L. & Deeming, T. J. 1978, Astrophys. and Space Science, 56, 285

Mathys, G. 1988, A & A, 189, 179

—. 1989, Fundamentals of Cosmic Physics, 13, 143

Mathys, G., Hubrig, S., Landstreet, J. D., Lanz, T., & Manfroid, J. 1997, A & AS, 123, 353

Matthews, J. M. 1991, PASP, 103, 5

Matthews, J. M., Kurtz, D. W., & Martinez, P. 1999, ApJ, 511, 422

Matthews, J. M., Kuschnig, R., Walker, G. A. H., Pazder, J., Johnson, R., Skaret, K., Shkolnik, E., Lanting, T., Morgan, J. P., & Sidhu, S. 2000, in ASP Conf. Ser. 203: IAU Colloq. 176: The Impact of Large-Scale Surveys on Pulsating Star Research, 74–75

Matthews, J. M., Wehlau, W. H., & Kurtz, D. W. 1987, ApJ, 313, 782

Michaud, G. 1970, ApJ, 160, 641

Michaud, G. 1976, in IAU Colloq. 32: Physics of Ap Stars, 81

Michaud, G. 1996, in IAU Symp. 176: Stellar Surface Structure, 321

Michaud, G., Charland, Y., & Megessier, C. 1981, A & A, 103, 244

Michaud, G. J. & Proffitt, C. R. 1993, in ASP Conf. Ser. 44: IAU Colloq. 138: Peculiar versus Normal Phenomena in A-type and Related Stars, 439

Montgomery, M.-H. & O'Donoghue, D. 1999, DSSN (Vienna), 13

Moon, T. T. & Dworetsky, M. M. 1985, MNRAS, 217, 305

Nather, R. E., Winget, D. E., Clemens, J. C., Hansen, C. J., & Hine, B. P. 1990, ApJ, 361, 309

Olive, K. A. & Steigman, G. 1995, ApJS, 97, 49

Preston, G. W. 1972, ApJ, 175, 465

—. 1974, ARA & A, 12, 257

Provost, J. 1984, in IAU Symp. 105: Observational Tests of the Stellar Evolution Theory, 47

Roberts, P. H. & Soward, A. M. 1983, MNRAS, 205, 1171

Rodríguez, E., Costa, V., Handler, G., & García, J. M. 2003, A & A, 399, 253

Rogers, F. J. 1986, ApJ, 310, 723

Rogers, F. J., Swenson, F. J., & Iglesias, C. A. 1996, ApJ, 456, 902

Ryabchikova, T. A., Landstreet, J. D., Gelbmann, M. J., Bolgova, G. T., Tsymbal, V. V., & Weiss, W. W. 1997, A & A, 327, 1137

Saio, H. & Cox, J. P. 1980, ApJ, 236, 549

Scargle, J. D. 1982, ApJ, 263, 835

Shibahashi, H. & Saio, H. 1985, PASJ, 37, 245

Shibahashi, H. & Takata, M. 1993, PASJ, 45, 617

Stibbs, D. W. N. 1950, MNRAS, 110, 395

Tassoul, M. 1980, ApJS, 43, 469

—. 1990, ApJ, 358, 313

Ulrich, R. K. 1970, ApJ, 162, 993

Unno, W., Osaki, Y., Ando, H., Saio, H., & Shibahashi, H. 1989, Nonradial oscillations of stars (Nonradial oscillations of stars, Tokyo: University of Tokyo Press, 1989, 2nd ed.)

Vauclair, S. & Vauclair, G. 1982, ARA & A, 20, 37

Wade, G. A. 1997, A & A, 325, 1063

Walker, G., Matthews, J., Kuschnig, R., Johnson, R., Rucinski, S., Pazder, J., Burley, G., Walker, A., Skaret, K., Zee, R., Grocott, S., Carroll, K., Sinclair, P., Sturgeon, D., & Harron, J. 2003, PASP, 115, 1023

Winget, D. E. 1993, in ASP Conf. Ser. 42: GONG 1992. Seismic Investigation of the Sun and Stars, 331

Wolff, S. C. 1983, The A-stars: Problems and perspectives. Monograph series on nonthermal phenomena in stellar atmospheres (The A-stars: Problems and perspectives. Monograph series on nonthermal phenomena in stellar atmospheres)

Appendix A

XCOV20 Observing Log

This appendix contains the observing log for HR 1217 during XCOV20. See the table caption for details.

Table A.1: A data log obtained during XCOV20. The log contains run names, telescopes used, the number of points collected, and comments from observers. The runs marked with a * are runs that were used in the frequency analysis. See Section 2.3.1 for selection criteria.

Run Name	Telescope	Date (UT)	Start Time (UT)	# of Points	Observer Comments
mdr136*	CTIO 1.5m	6-Nov-00	2:23:30	1760	2001 year in original data!
mdr137*	CTIO 1.5m	9-Nov-00	1:55:20	2524	vignetting present, re-reduced to correct(somewhat)
mdr138*	CTIO 1.5m	10-Nov-00	1:59:50	1756	sky in channel 2
mdr139*	CTIO 1.5m	12-Nov-00	2:16:00	2422	sky in CH2, dome problems in curve
mdr140*	CTIO 1.5m	13-Nov-00	1:34:30	2580	moon!
mdr141*	CTIO 1.5m	14-Nov-00	1:27:40	333	a few cycles between clouds
sa-od044*	SAAO 1.9m	14-Nov-00	21:03:00	1886	One channel - great run!
mdr142*	CTIO 1.5m	15-Nov-00	1:28:10	2645	very good run - look at those beats!
sa-od045*	SAAO 1.9m	15-Nov-00	19:20:00	2551	typical SAAO data - outstanding
teide01*	Teide 0.8m	16-Nov-00	0:42:10	1342	nice ch1
mdr143*	CTIO 1.5m	16-Nov-00	1:23:00	2732	another very good run
teideN03	Teide 0.8m	17-Nov-00	0:43:40	2164	entire run through clouds
mdr144*	CTIO 1.5m	17-Nov-00	1:18:20	2730	good run
no1700q2*	Hawaii 0.6m	17-Nov-00	7:28:00	1375	good night for first half
no1700q3*	Hawaii 0.6m	17-Nov-00	12:34:20	196	good second half of night!
teideN04*	Teide 0.8m	17-Nov-00	22:09:10	4366	5-sec integrations no sky at beginning before moon

continued on next page

Table A.1: *continued*

Run Name	Telescope	Date (UT)	Start Time (UT)	# of Points	Observer Comments
no1800q1*	Hawaii 0.6m	18-Nov-00	7:22:30	2360	nice run - some clouds
sa-od047*	SAAO 1.9m	18-Nov-00	23:29:00	798	short but sweet
teiden05*	Teide 0.8m	18-Nov-00	22:53:20	3892/2	reduction problems
no1900q2*	Hawaii 0.6m	19-Nov-00	10:14:20	1423	Nice run! subtracted 8066 cts from ch3
sa-od048*	SAAO 1.9m	19-Nov-00	18:55:00	2611	some dome glitches and 1% drop in counts - reason unknown
teideN06*	Teide 0.8m	19-Nov-00	22:05:30	4419	5 sec integrations...nice set
asm-0079*	McDonald 2.1m	20-Nov-00	3:58:40	2115	poor data
no2000q1*	Hawaii 0.6m	20-Nov-00	7:37:00	2249	low amp part of rotation cycle
pvb1118	Bickley 0.6m	18-Nov-00	12:28:31	2220	Single channel data from Perth
pvb1119	Bickley 0.6m	19-Nov-00	12:15:13	1495	
sa-od049*	SAAO 1.9m	20-Nov-00	18:51:00	2651	Darragh's Last Stand - Good night - no fit applied and 17pt. sky chunk so wrote in two chunks
pvb1120	Bickley 0.6m	20-Nov-00	12:19:12	2454	
asm-0081*	McDonald 2.1m	21-Nov-00	9:06:10	349	not used
pvb1121	Bickley 0.6m	21-Nov-00	12:49:17	2320	curious peaks at 200,250, 400, 1200 s...
sa-m0002*	SAAO 0.75m	21-Nov-00	19:08:00	106	counts 9 million at 10 sec int. times
sa-m0003*	SAAO 0.75m	21-Nov-00	19:26:50	4857	5sec integrations - counts 4 million per point
jxj-0121*	BAO 0.85m	22-Nov-00	14:47:50	1538	transparency variations - not used
sa-m0004*	SAAO 0.75m	22-Nov-00	18:28:20	5524	5 sec integrations - some intermittent clouds
joy-002	McDonald 2.1m	23-Nov-00	3:59:50	1958	Transparency variations (?)
teideN08*	Teide 0.8m	22-Nov-00	22:07:20	1364	5 sec integrations, humidity at end
no2300q1*	Hawaii 0.6m	23-Nov-00	7:15:50	1751	Intervening clouds
sa-m0005	SAAO 0.75m	23-Nov-00	18:11:50	892	
sso1123a*	SSO	23-Nov-00	12:42:28	467	not used: clouds, timing in question
sso1123b*	SSO	23-Nov-00	13:49:19	191	not used: clouds, timing in question
joy-005	McDonald 82"	24-Nov-00	4:08:30	2161	not used
teiden10*	tenerife 80cm	23-Nov-00	22:05:40	3943	
pvb1123*	Bickley 0.6m	23-Nov-00	12:15:41	1298	
sa0m0006*	SAAO 0.75m	24-Nov-00	18:18:00	5646	Periodicity in the sky at
teiden11*	Tenerife	25-Nov-00	2:03:30	1229	Huge seeing but good data nonetheless

continued on next page

Table A.1: *continued*

Run Name	Telescope	Date (UT)	Start Time (UT)	# of Points	Observer Comments
pvb1124*	Perth	24-Nov-00	12:18:40	2494	good first part
joy-009	McDonald 2.1m	25-Nov-00	4:22:50	1567	clouds - not used
jxj-0122	BAO 0.85m	25-Nov-00	15:41:20	563	clouds - not used
no2500q1*	Hawaii 0.6m	25-Nov-00	7:03:10	2457	very good run
teiden12*	tenerife 80cm	25-Nov-00	22:09:20	4040	long, good run
joy-012*	McDonald 2.1m	26-Nov-00	3:55:50	1497	good data
jxj-0123	BAO 0.85m	26-Nov-00	13:00:00	329	
no2600q2*	Hawaii 0.6m	26-Nov-00	6:59:30	2370	another nice run
jxj-0124*	BAO 0.85m	26-Nov-00	14:14:50	1536	strong transparency variations
sa-m0007*	SAAO 0.75m	26-Nov-00	18:28:40	5408	5 sec integrations, a nice run!
joy-016*	McDonald 82"	27-Nov-00	4:03:00	1956	clouds, ch1/ch2 division
no2700q1*	Hawaii 0.6m	27-Nov-00	6:38:00	2460	another nice run
sa-m0008*	SAAO 0.75m	27-Nov-00	18:27:50	5464	scattered on ends, but good signal
teiden13*	Teide 0.8m	26-Nov-00	21:50:30	316	a very short run, 5 sec integrations
jxj-0127*	BAO 0.85m	27-Nov-00	13:44:10	1733	beautiful!
teiden14*	Teide 0.8m	27-Nov-00	22:28:20	2910	Steve did this one...isn't it nice? :)
joy-020*	McDonald 82"	28-Nov-00	4:04:20	2315	clouds, non-standard reduction to bring out signal
no2800q1	Hawaii 0.6m	28-Nov-00	6:45:00	886	mostly clouds
sa-h-046*	SAAO 74"	28-Nov-00	18:54:30	2674	good run, about an hour trimmed from end
sso1127	SSO 0.6m	27-Nov-00	10:03:13	859	there's signal here!
jxj-0130*	BAO 0.85m	28-Nov-00	16:23:50	768	lots of clouds, but divided by channel 2 to get a signal
teiden15*	Tenerife 0.8 m	28-Nov-00	22:01:50	3976	large seeing but signal OK
joy-025*	McDonald 2.1 m	29-Nov-00	4:00:40	1895	middle part on clouds
no2900q1*	Hawaii 0.6m	29-Nov-00	6:41:00	2479	single channel but beautifull !
sa-gh465*	SAAO 74"	29-Nov-00	20:30:30	1942	
teideN16*	Tenerife 0.8m	29-Nov-00	21:18:50	4092	first half clouds, second half gorgeous!
joy-028*	McDonald 2.1 m	30-Nov-00	3:54:20	1899	a dataset so good even a theorist can reduce it! :)
no3000q1*	Mauna Kea 24"	30-Nov-00	6:40:50	2461	single-channel
jxj-0131	BAO 0.85m	29-Nov-00	12:58:40	801	run through clouds - unusable
jxj-0134	BAO 0.85m	30-Nov-00	13:22:20	833	Too many clouds. Rejected.
sa-gh466*	SAAO 74"	30-Nov-00	19:30:20	618	first of four pieces of the night
sa-gh467*	SAAO 74"	30-Nov-00	21:19:50	311	second piece
sa-gh468*	SAAO 74"	30-Nov-00	22:15:20	848	third piece
sa-gh469*	SAAO 74"	1-Dec-00	0:39:00	560	last piece
teiden17*	Teide 0.8m	30-Nov-00	21:17:50	4276	middle part missing because

continued on next page

Table A.1: *continued*

Run Name	Telescope	Date (UT)	Start Time (UT)	# of Points	Observer Comments
					mirror loose
sso1201	SSO 0.6m	1-Dec-00	9:47:57	1938	needed lots of low-f filtering
sa-gh470*	SAAO 74"	1-Dec-00	18:57:20	1259	first part of night
sa-gh471*	SAAO 74"	1-Dec-00	22:30:00	1348	second part of night
joy-031	McDonald 82"	1-Dec-00	3:48:50	1591	too many clouds dangit!
teiden18*	Tenerife	1-Dec-00	22:04:00	2780	target not centered
sa-gh472*	SAAO 74"	2-Dec-00	18:46:50	1020	
sa-gh473*	SAAO 74"	2-Dec	21:38:30	1600	
teiden19*	Teide 0.8m	2-Dec	21:46:50	3631	not useable
sa-gh474*	SAAO 74"	3-Dec	18:35:20	2713	good run, amplitude is decreaseing
sa-gh475*	SAAO 74"	4-Dec-00	21:51:00	1530	clouds, transparency variations
tsm-0087*	McDonald 82"	5-Dec-00	5:50:40	1100	electronics problems, no signal :(
tsm-0089*	McDonald 2.1m	6-Dec-00	3:47:00	1448	observer never did sky in ch1 at all
r00-022*	Nainital 40in.	6-Dec-00	18:55:00	859	
r00-025*	UPSO 1m	7-Dec-00	16:53:20	842	short run of reasonable quality
teiden22*	Teide 0.8m	8-Dec-00	21:37:40	3788	poor conditions to start, then cloud
teiden24*	Teide 0.8m	9-Dec-00	21:01:50	1386	5 sec. good short run
teiden27*	Teide 0.8m	11-Dec-00	0:20:40	1741	5 sec. good short run

Appendix B

A Listing of the Evolutionary Models

This appendix provides a listing of parameters for the 569 models that fell within the error box defined by the Hipparcos luminosity of 7.8 $\pm$ 0.7 $L_{\odot}$ and the effective temperature of $T_{eff} = 7400^{+100}_{-200}$ K. A discussion of these parameters may be found in Section 3.1.1.

Table B.1: A listing of the models that fall within the Hipparcos luminosity errorbars. The table lists the Mass in Solar units, the effective temperature in degrees Kelvin, the logarithm of the luminosity in Solar units, the age in units of 10^9 years, the large spacing in μHz, the hydrogen and heavy metal mass fractions, and the mixing length parameter for each model.

$M_{\odot}$	Log(T_{eff})	Log(L/$L_{\odot}$)	Age(Gyrs)	$\Delta\nu(\mu Hz)$	X	Z	α
1.3	3.85765	0.928366	2.15	57.6018	0.7	0.008	1.8
1.3	3.86255	0.916046	2.1	60.6058	0.7	0.008	1.8
1.3	3.86822	0.897114	2.05	64.8293	0.7	0.008	1.8
1.3	3.85737	0.928035	2.15	57.4146	0.7	0.008	1.6
1.3	3.86241	0.91588	2.1	60.4919	0.7	0.008	1.6
1.3	3.86815	0.897607	2.05	64.6873	0.7	0.008	1.6
1.3	3.85733	0.927571	2.15	57.3839	0.7	0.008	1.4
1.3	3.86238	0.915361	2.1	60.4818	0.7	0.008	1.4
1.3	3.868	0.897284	2.05	64.6136	0.7	0.008	1.4
1.4	3.8575	0.875949	1.6	64.9489	0.72	0.008	1.8
1.4	3.86122	0.871991	1.55	66.8804	0.72	0.008	1.8
1.4	3.86471	0.867916	1.5	68.8062	0.72	0.008	1.8
1.4	3.86798	0.863722	1.45	70.7379	0.72	0.008	1.8

continued on next page

Table B.1: *continued*

$M_\odot$	**Log(T_{eff})**	**Log(L/$L_\odot$)**	**Age(Gyrs)**	$\Delta\nu(\mu Hz)$	**X**	**Z**	α
1.4	3.87098	0.859405	1.4	72.6281	0.72	0.008	1.8
1.4	3.87374	0.855005	1.35	74.4692	0.72	0.008	1.8
1.4	3.85702	0.875949	1.6	64.5369	0.72	0.008	1.6
1.4	3.86092	0.871991	1.55	66.5959	0.72	0.008	1.6
1.4	3.86451	0.867916	1.5	68.6111	0.72	0.008	1.6
1.4	3.86783	0.863722	1.45	70.5892	0.72	0.008	1.6
1.4	3.87087	0.859405	1.4	72.5052	0.72	0.008	1.6
1.4	3.87364	0.855005	1.35	74.3607	0.72	0.008	1.6
1.4	3.86077	0.871985	1.55	66.4611	0.72	0.008	1.4
1.4	3.8644	0.867917	1.5	68.5018	0.72	0.008	1.4
1.4	3.86774	0.863723	1.45	70.4938	0.72	0.008	1.4
1.4	3.87079	0.859405	1.4	72.4196	0.72	0.008	1.4
1.4	3.87357	0.855005	1.35	74.2826	0.72	0.008	1.4
1.4	3.85757	0.851844	1.4	67.8035	0.7	0.01	1.8
1.4	3.85985	0.922619	1.5	60.8632	0.7	0.008	1.8
1.4	3.86449	0.917968	1.45	63.1424	0.7	0.008	1.8
1.4	3.86899	0.913406	1.4	65.4752	0.7	0.008	1.8
1.4	3.87314	0.908921	1.35	67.7485	0.7	0.008	1.8
1.4	3.85958	0.922623	1.5	60.6338	0.7	0.008	1.6
1.4	3.86432	0.917972	1.45	62.9949	0.7	0.008	1.6
1.4	3.86887	0.913409	1.4	65.3644	0.7	0.008	1.6
1.4	3.87304	0.908925	1.35	67.6572	0.7	0.008	1.6
1.4	3.85949	0.922435	1.5	60.5577	0.7	0.008	1.4
1.4	3.86426	0.91779	1.45	62.9375	0.7	0.008	1.4
1.4	3.86877	0.913329	1.4	65.2847	0.7	0.008	1.4
1.4	3.87298	0.908855	1.35	67.5987	0.7	0.008	1.4
1.45	3.85783	0.896504	1.6	63.8919	0.74	0.008	1.8
1.45	3.86165	0.892743	1.55	65.8174	0.74	0.008	1.8
1.45	3.86524	0.888781	1.5	67.7605	0.74	0.008	1.8
1.45	3.86857	0.884659	1.45	69.6902	0.74	0.008	1.8
1.45	3.87162	0.880411	1.4	71.5685	0.74	0.008	1.8
1.45	3.87441	0.876023	1.35	73.4015	0.74	0.008	1.8
1.45	3.85743	0.896512	1.6	63.543	0.74	0.008	1.6
1.45	3.8614	0.892746	1.55	65.5866	0.74	0.008	1.6
1.45	3.86507	0.888784	1.5	67.5971	0.74	0.008	1.6
1.45	3.86844	0.884662	1.45	69.56	0.74	0.008	1.6
1.45	3.87151	0.880414	1.4	71.4574	0.74	0.008	1.6
1.45	3.87432	0.876023	1.35	73.3052	0.74	0.008	1.6
1.45	3.85727	0.896504	1.6	63.3988	0.74	0.008	1.4
1.45	3.86128	0.892743	1.55	65.47	0.74	0.008	1.4

continued on next page

Table B.1: *continued*

$M_\odot$	**Log(T_{eff})**	**Log(L/$L_\odot$)**	**Age(Gyrs)**	$\Delta\nu(\mu Hz)$	**X**	**Z**	α
1.45	3.86497	0.888781	1.5	67.4989	0.74	0.008	1.4
1.45	3.86836	0.884659	1.45	69.4738	0.74	0.008	1.4
1.45	3.87144	0.880411	1.4	71.3801	0.74	0.008	1.4
1.45	3.87426	0.876023	1.35	73.233	0.74	0.008	1.4
1.45	3.85793	0.8708	1.4	66.8921	0.72	0.01	1.8
1.45	3.86091	0.86701	1.35	68.55	0.72	0.01	1.8
1.45	3.86366	0.863251	1.3	70.1623	0.72	0.01	1.8
1.45	3.86612	0.858976	1.25	71.7555	0.72	0.01	1.8
1.45	3.86856	0.854837	1.2	73.3787	0.72	0.01	1.8
1.45	3.85746	0.8708	1.4	66.4672	0.72	0.01	1.6
1.45	3.86058	0.86701	1.35	68.228	0.72	0.01	1.6
1.45	3.86343	0.863251	1.3	69.9228	0.72	0.01	1.6
1.45	3.86594	0.858976	1.25	71.5686	0.72	0.01	1.6
1.45	3.86841	0.854837	1.2	73.2248	0.72	0.01	1.6
1.45	3.85728	0.8708	1.4	66.2956	0.72	0.01	1.4
1.45	3.86043	0.86701	1.35	68.0886	0.72	0.01	1.4
1.45	3.86331	0.863251	1.3	69.8024	0.72	0.01	1.4
1.45	3.86583	0.858976	1.25	71.4594	0.72	0.01	1.4
1.45	3.86833	0.854837	1.2	73.1265	0.72	0.01	1.4
1.45	3.87396	0.928899	1.35	66.9595	0.72	0.008	1.8
1.45	3.87388	0.928899	1.35	66.8791	0.72	0.008	1.6
1.45	3.87382	0.928899	1.35	66.8173	0.72	0.008	1.4
1.45	3.85888	0.869731	1.25	67.4304	0.7	0.012	1.8
1.45	3.86176	0.865865	1.2	69.0743	0.7	0.012	1.8
1.45	3.86449	0.86184	1.15	70.7197	0.7	0.012	1.8
1.45	3.86705	0.85774	1.1	72.36	0.7	0.012	1.8
1.45	3.86945	0.853583	1.05	73.9823	0.7	0.012	1.8
1.45	3.85844	0.869731	1.25	67.0264	0.7	0.012	1.6
1.45	3.86145	0.865865	1.2	68.7697	0.7	0.012	1.6
1.45	3.86426	0.86184	1.15	70.4924	0.7	0.012	1.6
1.45	3.86688	0.85774	1.1	72.1824	0.7	0.012	1.6
1.45	3.86931	0.853583	1.05	73.8338	0.7	0.012	1.6
1.45	3.85827	0.869731	1.25	66.8639	0.7	0.012	1.4
1.45	3.86132	0.865865	1.2	68.6354	0.7	0.012	1.4
1.45	3.86415	0.86184	1.15	70.3754	0.7	0.012	1.4
1.45	3.86678	0.85774	1.1	72.0775	0.7	0.012	1.4
1.45	3.86922	0.853583	1.05	73.738	0.7	0.012	1.4
1.45	3.85832	0.919151	1.35	61.7557	0.7	0.01	1.8
1.45	3.86254	0.915222	1.3	63.8007	0.7	0.01	1.8
1.45	3.86648	0.911116	1.25	65.8569	0.7	0.01	1.8

continued on next page

Table B.1: *continued*

$M_\odot$	**Log(T_{eff})**	**Log(L/$L_\odot$)**	**Age(Gyrs)**	$\Delta\nu(\mu Hz)$	**X**	**Z**	α
1.45	3.87003	0.906915	1.2	67.8436	0.7	0.01	1.8
1.45	3.87337	0.902535	1.15	69.8247	0.7	0.01	1.8
1.45	3.85797	0.919152	1.35	61.4599	0.7	0.01	1.6
1.45	3.86233	0.915223	1.3	63.6147	0.7	0.01	1.6
1.45	3.86633	0.911118	1.25	65.7233	0.7	0.01	1.6
1.45	3.86991	0.906916	1.2	67.7348	0.7	0.01	1.6
1.45	3.87327	0.902536	1.15	69.7304	0.7	0.01	1.6
1.45	3.85782	0.919151	1.35	61.3306	0.7	0.01	1.4
1.45	3.86222	0.915222	1.3	63.5119	0.7	0.01	1.4
1.45	3.86624	0.911116	1.25	65.636	0.7	0.01	1.4
1.45	3.86984	0.906915	1.2	67.657	0.7	0.01	1.4
1.45	3.87321	0.902535	1.15	69.6618	0.7	0.01	1.4
1.5	3.8587	0.888643	1.4	66.2434	0.74	0.01	1.8
1.5	3.86171	0.884874	1.35	67.9063	0.74	0.01	1.8
1.5	3.86452	0.880972	1.3	69.5574	0.74	0.01	1.8
1.5	3.86715	0.876985	1.25	71.1936	0.74	0.01	1.8
1.5	3.86951	0.872786	1.2	72.7824	0.74	0.01	1.8
1.5	3.87177	0.868646	1.15	74.3589	0.74	0.01	1.8
1.5	3.87383	0.864429	1.1	75.884	0.74	0.01	1.8
1.5	3.85831	0.888656	1.4	65.8896	0.74	0.01	1.6
1.5	3.86145	0.884881	1.35	67.6495	0.74	0.01	1.6
1.5	3.86433	0.880979	1.3	69.3654	0.74	0.01	1.6
1.5	3.867	0.876993	1.25	71.0392	0.74	0.01	1.6
1.5	3.86938	0.872792	1.2	72.6488	0.74	0.01	1.6
1.5	3.87166	0.868652	1.15	74.2391	0.74	0.01	1.6
1.5	3.87374	0.864435	1.1	75.7747	0.74	0.01	1.6
1.5	3.85817	0.888663	1.4	65.7509	0.74	0.01	1.4
1.5	3.86132	0.884879	1.35	67.5261	0.74	0.01	1.4
1.5	3.86423	0.880977	1.3	69.2558	0.74	0.01	1.4
1.5	3.86691	0.876992	1.25	70.941	0.74	0.01	1.4
1.5	3.8693	0.872788	1.2	72.5581	0.74	0.01	1.4
1.5	3.87159	0.868649	1.15	74.1561	0.74	0.01	1.4
1.5	3.87367	0.864432	1.1	75.6969	0.74	0.01	1.4
1.5	3.85727	0.890614	1.3	65.4885	0.72	0.012	1.8
1.5	3.86035	0.8869	1.25	67.1448	0.72	0.012	1.8
1.5	3.86318	0.883	1.2	68.7772	0.72	0.012	1.8
1.5	3.86586	0.879004	1.15	70.4083	0.72	0.012	1.8
1.5	3.86832	0.875007	1.1	71.9974	0.72	0.012	1.8
1.5	3.87064	0.870876	1.05	73.5765	0.72	0.012	1.8
1.5	3.87279	0.86665	1	75.13	0.72	0.012	1.8

continued on next page

Table B.1: *continued*

$M_\odot$	**Log(T_{eff})**	**Log(L/$L_\odot$)**	**Age(Gyrs)**	$\Delta\nu(\mu Hz)$	**X**	**Z**	α
1.5	3.8748	0.862408	0.95	76.6515	0.72	0.012	1.8
1.5	3.86003	0.886835	1.25	66.8467	0.72	0.012	1.6
1.5	3.86299	0.882919	1.2	68.5757	0.72	0.012	1.6
1.5	3.86573	0.878904	1.15	70.2628	0.72	0.012	1.6
1.5	3.86817	0.875035	1.1	71.8421	0.72	0.012	1.6
1.5	3.87051	0.870867	1.05	73.4485	0.72	0.012	1.6
1.5	3.87269	0.866648	1	75.0159	0.72	0.012	1.6
1.5	3.87471	0.862395	0.95	76.5461	0.72	0.012	1.6
1.5	3.85988	0.886847	1.25	66.7075	0.72	0.012	1.4
1.5	3.86287	0.882933	1.2	68.4562	0.72	0.012	1.4
1.5	3.86563	0.878914	1.15	70.1577	0.72	0.012	1.4
1.5	3.86809	0.875035	1.1	71.7493	0.72	0.012	1.4
1.5	3.87044	0.87087	1.05	73.3627	0.72	0.012	1.4
1.5	3.87262	0.866654	1	74.9362	0.72	0.012	1.4
1.5	3.87465	0.862396	0.95	76.4702	0.72	0.012	1.4
1.5	3.86851	0.928683	1.25	65.8202	0.72	0.01	1.8
1.5	3.87204	0.92441	1.2	67.8106	0.72	0.01	1.8
1.5	3.86839	0.928683	1.25	65.7117	0.72	0.01	1.6
1.5	3.87194	0.92441	1.2	67.7188	0.72	0.01	1.6
1.5	3.86832	0.928683	1.25	65.6342	0.72	0.01	1.4
1.5	3.87188	0.92441	1.2	67.6512	0.72	0.01	1.4
1.5	3.85908	0.890462	1.15	66.2585	0.7	0.014	1.8
1.5	3.86202	0.886593	1.1	67.9038	0.7	0.014	1.8
1.5	3.86479	0.882576	1.05	69.5472	0.7	0.014	1.8
1.5	3.86736	0.878627	1	71.1523	0.7	0.014	1.8
1.5	3.86972	0.874471	0.95	72.7368	0.7	0.014	1.8
1.5	3.87197	0.870235	0.9	74.3154	0.7	0.014	1.8
1.5	3.87406	0.865959	0.85	75.865	0.7	0.014	1.8
1.5	3.8587	0.890515	1.15	65.9006	0.7	0.014	1.6
1.5	3.86176	0.886648	1.1	67.6398	0.7	0.014	1.6
1.5	3.86459	0.882608	1.05	69.3468	0.7	0.014	1.6
1.5	3.8672	0.878653	1	70.9899	0.7	0.014	1.6
1.5	3.8696	0.874471	0.95	72.6039	0.7	0.014	1.6
1.5	3.87186	0.870235	0.9	74.1976	0.7	0.014	1.6
1.5	3.87397	0.865959	0.85	75.7569	0.7	0.014	1.6
1.5	3.85854	0.890462	1.15	65.7599	0.7	0.014	1.4
1.5	3.86164	0.886593	1.1	67.5215	0.7	0.014	1.4
1.5	3.86449	0.882576	1.05	69.2466	0.7	0.014	1.4
1.5	3.86712	0.878627	1	70.899	0.7	0.014	1.4
1.5	3.86952	0.874471	0.95	72.5136	0.7	0.014	1.4

continued on next page

Table B.1: *continued*

$M_\odot$	**Log(T_{eff})**	**Log(L/$L_\odot$)**	**Age(Gyrs)**	$\Delta\nu(\mu Hz)$	**X**	**Z**	α
1.5	3.87179	0.870235	0.9	74.1147	0.7	0.014	1.4
1.5	3.8739	0.865959	0.85	75.6791	0.7	0.014	1.4
1.5	3.87091	0.926943	1.1	67.065	0.7	0.012	1.8
1.5	3.87416	0.922573	1.05	68.986	0.7	0.012	1.8
1.5	3.87081	0.926943	1.1	66.9671	0.7	0.012	1.6
1.5	3.87408	0.922573	1.05	68.9015	0.7	0.012	1.6
1.5	3.87074	0.926943	1.1	66.8963	0.7	0.012	1.4
1.5	3.87402	0.922573	1.05	68.838	0.7	0.012	1.4
1.55	3.85746	0.855907	1.15	70.6776	0.74	0.014	1.8
1.55	3.85949	0.852278	1.1	71.9939	0.74	0.014	1.8
1.55	3.85906	0.852278	1.1	71.5591	0.74	0.014	1.6
1.55	3.85891	0.852254	1.1	71.3906	0.74	0.014	1.4
1.55	3.85814	0.906712	1.3	65.0552	0.74	0.012	1.8
1.55	3.86115	0.90298	1.25	66.6864	0.74	0.012	1.8
1.55	3.86399	0.899172	1.2	68.3096	0.74	0.012	1.8
1.55	3.86665	0.895184	1.15	69.931	0.74	0.012	1.8
1.55	3.8691	0.891157	1.1	71.5133	0.74	0.012	1.8
1.55	3.87137	0.887073	1.05	73.0606	0.74	0.012	1.8
1.55	3.87349	0.882926	1	74.5796	0.74	0.012	1.8
1.55	3.85777	0.906712	1.3	64.7198	0.74	0.012	1.6
1.55	3.8609	0.90298	1.25	66.4415	0.74	0.012	1.6
1.55	3.86381	0.899172	1.2	68.1254	0.74	0.012	1.6
1.55	3.8665	0.895184	1.15	69.7831	0.74	0.012	1.6
1.55	3.86898	0.891157	1.1	71.3852	0.74	0.012	1.6
1.55	3.87127	0.887073	1.05	72.9476	0.74	0.012	1.6
1.55	3.8734	0.882926	1	74.4758	0.74	0.012	1.6
1.55	3.85763	0.906686	1.3	64.5847	0.74	0.012	1.4
1.55	3.86079	0.902952	1.25	66.3279	0.74	0.012	1.4
1.55	3.86371	0.899143	1.2	68.0274	0.74	0.012	1.4
1.55	3.86641	0.895184	1.15	69.6886	0.74	0.012	1.4
1.55	3.8689	0.891157	1.1	71.2988	0.74	0.012	1.4
1.55	3.8712	0.887073	1.05	72.8676	0.74	0.012	1.4
1.55	3.87334	0.882926	1	74.401	0.74	0.012	1.4
1.55	3.85714	0.859941	1.05	70.0967	0.72	0.016	1.8
1.55	3.85922	0.85626	1	71.4261	0.72	0.016	1.8
1.55	3.86118	0.852536	0.95	72.7393	0.72	0.016	1.8
1.55	3.85877	0.85626	1	70.981	0.72	0.016	1.6
1.55	3.86081	0.852535	0.95	72.3597	0.72	0.016	1.6
1.55	3.8586	0.85626	1	70.8024	0.72	0.016	1.4
1.55	3.86067	0.852536	0.95	72.2031	0.72	0.016	1.4

continued on next page

Table B.1: *continued*

$M_\odot$	**Log(T_{eff})**	**Log(L/$L_\odot$)**	**Age(Gyrs)**	$\Delta\nu(\mu Hz)$	**X**	**Z**	α
1.55	3.85723	0.909133	1.2	64.4636	0.72	0.014	1.8
1.55	3.86026	0.90557	1.15	66.0613	0.72	0.014	1.8
1.55	3.86309	0.901847	1.1	67.6516	0.72	0.014	1.8
1.55	3.86577	0.897882	1.05	69.2581	0.72	0.014	1.8
1.55	3.86828	0.893962	1	70.8379	0.72	0.014	1.8
1.55	3.87059	0.889845	0.95	72.3882	0.72	0.014	1.8
1.55	3.87277	0.885666	0.9	73.9256	0.72	0.014	1.8
1.55	3.87481	0.881453	0.85	75.4312	0.72	0.014	1.8
1.55	3.85997	0.905564	1.15	65.7864	0.72	0.014	1.6
1.55	3.86289	0.901845	1.1	67.4478	0.72	0.014	1.6
1.55	3.86561	0.897882	1.05	69.0986	0.72	0.014	1.6
1.55	3.86816	0.893962	1	70.7027	0.72	0.014	1.6
1.55	3.87048	0.889845	0.95	72.2691	0.72	0.014	1.6
1.55	3.87268	0.885666	0.9	73.8191	0.72	0.014	1.6
1.55	3.87472	0.881453	0.85	75.3334	0.72	0.014	1.6
1.55	3.85983	0.905596	1.15	65.6521	0.72	0.014	1.4
1.55	3.86277	0.901884	1.1	67.3287	0.72	0.014	1.4
1.55	3.86551	0.897918	1.05	68.9925	0.72	0.014	1.4
1.55	3.86807	0.893995	1	70.6058	0.72	0.014	1.4
1.55	3.87041	0.889845	0.95	72.1866	0.72	0.014	1.4
1.55	3.87261	0.885666	0.9	73.7422	0.72	0.014	1.4
1.55	3.87466	0.881453	0.85	75.2612	0.72	0.014	1.4
1.55	3.85718	0.865042	0.95	69.5384	0.7	0.018	1.8
1.55	3.85935	0.861363	0.9	70.8981	0.7	0.018	1.8
1.55	3.86138	0.857611	0.85	72.2392	0.7	0.018	1.8
1.55	3.86327	0.853773	0.8	73.5562	0.7	0.018	1.8
1.55	3.8589	0.861363	0.9	70.4601	0.7	0.018	1.6
1.55	3.86103	0.857611	0.85	71.8715	0.7	0.018	1.6
1.55	3.86299	0.853773	0.8	73.249	0.7	0.018	1.6
1.55	3.85874	0.861363	0.9	70.288	0.7	0.018	1.4
1.55	3.86089	0.857611	0.85	71.7202	0.7	0.018	1.4
1.55	3.86287	0.853773	0.8	73.1135	0.7	0.018	1.4
1.55	3.85994	0.909967	1.05	65.472	0.7	0.016	1.8
1.55	3.86286	0.906075	1	67.1018	0.7	0.016	1.8
1.55	3.86562	0.902089	0.95	68.7333	0.7	0.016	1.8
1.55	3.86821	0.89794	0.9	70.3609	0.7	0.016	1.8
1.55	3.87061	0.893779	0.85	71.9499	0.7	0.016	1.8
1.55	3.87285	0.889562	0.8	73.5117	0.7	0.016	1.8
1.55	3.85963	0.909967	1.05	65.1873	0.7	0.016	1.6
1.55	3.86265	0.906075	1	66.8935	0.7	0.016	1.6

continued on next page

Table B.1: *continued*

$M_\odot$	**Log(T_{eff})**	**Log(L/$L_\odot$)**	**Age(Gyrs)**	$\Delta\nu(\mu Hz)$	**X**	**Z**	α
1.55	3.86546	0.902089	0.95	68.5729	0.7	0.016	1.6
1.55	3.86808	0.89794	0.9	70.226	0.7	0.016	1.6
1.55	3.8705	0.893779	0.85	71.8318	0.7	0.016	1.6
1.55	3.87276	0.889562	0.8	73.4064	0.7	0.016	1.6
1.55	3.8595	0.909967	1.05	65.0596	0.7	0.016	1.4
1.55	3.86254	0.906075	1	66.784	0.7	0.016	1.4
1.55	3.86537	0.902089	0.95	68.4745	0.7	0.016	1.4
1.55	3.868	0.89794	0.9	70.1374	0.7	0.016	1.4
1.55	3.87043	0.893779	0.85	71.7501	0.7	0.016	1.4
1.55	3.87269	0.889562	0.8	73.3303	0.7	0.016	1.4
1.6	3.85784	0.873785	1.05	69.7927	0.74	0.016	1.8
1.6	3.85988	0.870186	1	71.0932	0.74	0.016	1.8
1.6	3.86179	0.866522	0.95	72.3761	0.74	0.016	1.8
1.6	3.8636	0.862854	0.9	73.6413	0.74	0.016	1.8
1.6	3.86531	0.859104	0.85	74.8966	0.74	0.016	1.8
1.6	3.86641	0.854883	0.8	75.9517	0.74	0.016	1.8
1.6	3.85738	0.873785	1.05	69.3439	0.74	0.016	1.6
1.6	3.8595	0.870186	1	70.7117	0.74	0.016	1.6
1.6	3.86149	0.866522	0.95	72.0553	0.74	0.016	1.6
1.6	3.86336	0.862854	0.9	73.3726	0.74	0.016	1.6
1.6	3.86511	0.859104	0.85	74.6695	0.74	0.016	1.6
1.6	3.86623	0.854883	0.8	75.7441	0.74	0.016	1.6
1.6	3.8572	0.873785	1.05	69.1632	0.74	0.016	1.4
1.6	3.85936	0.870186	1	70.5541	0.74	0.016	1.4
1.6	3.86136	0.866522	0.95	71.9153	0.74	0.016	1.4
1.6	3.86324	0.862854	0.9	73.2447	0.74	0.016	1.4
1.6	3.865	0.859104	0.85	74.5509	0.74	0.016	1.4
1.6	3.86614	0.854883	0.8	75.6298	0.74	0.016	1.4
1.6	3.85849	0.923694	1.2	64.3305	0.74	0.014	1.8
1.6	3.86144	0.920105	1.15	65.9082	0.74	0.014	1.8
1.6	3.86421	0.916358	1.1	67.4857	0.74	0.014	1.8
1.6	3.86683	0.912452	1.05	69.065	0.74	0.014	1.8
1.6	3.86928	0.908516	1	70.6182	0.74	0.014	1.8
1.6	3.87155	0.904496	0.95	72.1435	0.74	0.014	1.8
1.6	3.87367	0.900453	0.9	73.6316	0.74	0.014	1.8
1.6	3.85817	0.923694	1.2	64.0363	0.74	0.014	1.6
1.6	3.86122	0.920105	1.15	65.693	0.74	0.014	1.6
1.6	3.86405	0.916358	1.1	67.3201	0.74	0.014	1.6
1.6	3.86669	0.912452	1.05	68.9279	0.74	0.014	1.6
1.6	3.86916	0.908516	1	70.4989	0.74	0.014	1.6

continued on next page

Table B.1: *continued*

$M_\odot$	**Log(T_{eff})**	**Log(L/$L_\odot$)**	**Age(Gyrs)**	$\Delta\nu(\mu Hz)$	**X**	**Z**	α
1.6	3.87146	0.904496	0.95	72.0366	0.74	0.014	1.6
1.6	3.87359	0.900453	0.9	73.5351	0.74	0.014	1.6
1.6	3.85803	0.923694	1.2	63.9062	0.74	0.014	1.4
1.6	3.8611	0.920105	1.15	65.5815	0.74	0.014	1.4
1.6	3.86395	0.916358	1.1	67.2213	0.74	0.014	1.4
1.6	3.86661	0.912452	1.05	68.8386	0.74	0.014	1.4
1.6	3.86909	0.908516	1	70.417	0.74	0.014	1.4
1.6	3.87139	0.904496	0.95	71.9607	0.74	0.014	1.4
1.6	3.87353	0.900453	0.9	73.4632	0.74	0.014	1.4
1.6	3.85767	0.878412	0.95	69.2064	0.72	0.018	1.8
1.6	3.85975	0.874753	0.9	70.5244	0.72	0.018	1.8
1.6	3.86172	0.871049	0.85	71.8266	0.72	0.018	1.8
1.6	3.86358	0.867309	0.8	73.1143	0.72	0.018	1.8
1.6	3.85719	0.878412	0.95	68.7535	0.72	0.018	1.6
1.6	3.85937	0.874753	0.9	70.139	0.72	0.018	1.6
1.6	3.86142	0.871049	0.85	71.5049	0.72	0.018	1.6
1.6	3.86334	0.867309	0.8	72.8471	0.72	0.018	1.6
1.6	3.85702	0.878412	0.95	68.5725	0.72	0.018	1.4
1.6	3.85922	0.874753	0.9	69.9831	0.72	0.018	1.4
1.6	3.86129	0.871049	0.85	71.3663	0.72	0.018	1.4
1.6	3.86323	0.867309	0.8	72.7208	0.72	0.018	1.4
1.6	3.85802	0.926903	1.1	63.8287	0.72	0.016	1.8
1.6	3.86104	0.923197	1.05	65.4296	0.72	0.016	1.8
1.6	3.86387	0.919343	1	67.0315	0.72	0.016	1.8
1.6	3.86655	0.915407	0.95	68.6281	0.72	0.016	1.8
1.6	3.86904	0.911376	0.9	70.2034	0.72	0.016	1.8
1.6	3.87136	0.907276	0.85	71.7458	0.72	0.016	1.8
1.6	3.87352	0.903129	0.8	73.2589	0.72	0.016	1.8
1.6	3.85768	0.926903	1.1	63.5175	0.72	0.016	1.6
1.6	3.8608	0.923197	1.05	65.2041	0.72	0.016	1.6
1.6	3.8637	0.919343	1	66.8601	0.72	0.016	1.6
1.6	3.86641	0.915407	0.95	68.4883	0.72	0.016	1.6
1.6	3.86893	0.911376	0.9	70.0826	0.72	0.016	1.6
1.6	3.87126	0.907276	0.85	71.638	0.72	0.016	1.6
1.6	3.87344	0.903129	0.8	73.1617	0.72	0.016	1.6
1.6	3.85753	0.926903	1.1	63.3833	0.72	0.016	1.4
1.6	3.86068	0.923197	1.05	65.0899	0.72	0.016	1.4
1.6	3.8636	0.919343	1	66.7603	0.72	0.016	1.4
1.6	3.86633	0.915407	0.95	68.3984	0.72	0.016	1.4
1.6	3.86886	0.911376	0.9	70.0002	0.72	0.016	1.4

continued on next page

Table B.1: *continued*

$M_\odot$	**Log(T_{eff})**	**Log(L/$L_\odot$)**	**Age(Gyrs)**	$\Delta\nu(\mu Hz)$	**X**	**Z**	α
1.6	3.8712	0.907276	0.85	71.5616	0.72	0.016	1.4
1.6	3.87338	0.903129	0.8	73.0904	0.72	0.016	1.4
1.6	3.85828	0.883976	0.85	68.841	0.7	0.02	1.8
1.6	3.86042	0.880244	0.8	70.1876	0.7	0.02	1.8
1.6	3.85783	0.883993	0.85	68.4121	0.7	0.02	1.6
1.6	3.86007	0.880261	0.8	69.8307	0.7	0.02	1.6
1.6	3.85767	0.883976	0.85	68.2481	0.7	0.02	1.4
1.6	3.85993	0.880244	0.8	69.6879	0.7	0.02	1.4
1.6	3.86179	0.928187	0.95	65.2113	0.7	0.018	1.8
1.6	3.86466	0.924254	0.9	66.8359	0.7	0.018	1.8
1.6	3.86734	0.920222	0.85	68.4449	0.7	0.018	1.8
1.6	3.86986	0.916113	0.8	70.0399	0.7	0.018	1.8
1.6	3.86158	0.928187	0.95	65.0071	0.7	0.018	1.6
1.6	3.8645	0.924254	0.9	66.6799	0.7	0.018	1.6
1.6	3.86721	0.920222	0.85	68.3156	0.7	0.018	1.6
1.6	3.86975	0.916113	0.8	69.9274	0.7	0.018	1.6
1.6	3.86147	0.928187	0.95	64.9001	0.7	0.018	1.4
1.6	3.86441	0.924254	0.9	66.5841	0.7	0.018	1.4
1.6	3.86713	0.920222	0.85	68.2287	0.7	0.018	1.4
1.6	3.86968	0.916113	0.8	69.8485	0.7	0.018	1.4
1.65	3.85826	0.890965	0.95	68.9859	0.74	0.018	1.8
1.65	3.8602	0.887234	0.9	70.2487	0.74	0.018	1.8
1.65	3.86213	0.883633	0.85	71.5199	0.74	0.018	1.8
1.65	3.8639	0.880199	0.8	72.7274	0.74	0.018	1.8
1.65	3.86678	0.871864	0.7	75.0978	0.74	0.018	1.8
1.65	3.86517	0.875609	0.75	73.8728	0.74	0.018	1.8
1.65	3.86829	0.868118	0.65	76.2971	0.74	0.018	1.8
1.65	3.86954	0.86402	0.6	77.4363	0.74	0.018	1.8
1.65	3.87208	0.856272	0.5	79.7346	0.74	0.018	1.8
1.65	3.87086	0.860187	0.55	78.5947	0.74	0.018	1.8
1.65	3.87302	0.852268	0.45	80.758	0.74	0.018	1.8
1.65	3.85785	0.890965	0.95	68.59	0.74	0.018	1.6
1.65	3.86187	0.883633	0.85	71.241	0.74	0.018	1.6
1.65	3.85987	0.887234	0.9	69.9142	0.74	0.018	1.6
1.65	3.86369	0.880199	0.8	72.4954	0.74	0.018	1.6
1.65	3.86499	0.875609	0.75	73.6627	0.74	0.018	1.6
1.65	3.86663	0.871864	0.7	74.9147	0.74	0.018	1.6
1.65	3.86815	0.868118	0.65	76.1343	0.74	0.018	1.6
1.65	3.86941	0.86402	0.6	77.2841	0.74	0.018	1.6
1.65	3.87074	0.860187	0.55	78.4532	0.74	0.018	1.6

continued on next page

Table B.1: *continued*

$M_\odot$	**Log(T_{eff})**	**Log(L/$L_\odot$)**	**Age(Gyrs)**	$\Delta\nu(\mu Hz)$	**X**	**Z**	α
1.65	3.87197	0.856272	0.5	79.6023	0.74	0.018	1.6
1.65	3.87292	0.852268	0.45	80.6305	0.74	0.018	1.6
1.65	3.8577	0.890965	0.95	68.4283	0.74	0.018	1.4
1.65	3.85974	0.887234	0.9	69.7705	0.74	0.018	1.4
1.65	3.86358	0.880199	0.8	72.3759	0.74	0.018	1.4
1.65	3.86175	0.883633	0.85	71.1122	0.74	0.018	1.4
1.65	3.86489	0.875609	0.75	73.5494	0.74	0.018	1.4
1.65	3.86653	0.871864	0.7	74.8082	0.74	0.018	1.4
1.65	3.86934	0.86402	0.6	77.1869	0.74	0.018	1.4
1.65	3.86807	0.868118	0.65	76.0334	0.74	0.018	1.4
1.65	3.87067	0.860187	0.55	78.3599	0.74	0.018	1.4
1.65	3.87191	0.856272	0.5	79.5123	0.74	0.018	1.4
1.65	3.87286	0.852268	0.45	80.5424	0.74	0.018	1.4
1.65	3.86754	0.928044	0.95	68.6027	0.74	0.016	1.8
1.65	3.86992	0.924115	0.9	70.1192	0.74	0.016	1.8
1.65	3.87426	0.916134	0.8	73.0762	0.74	0.016	1.8
1.65	3.87216	0.920137	0.85	71.6134	0.74	0.016	1.8
1.65	3.86742	0.928044	0.95	68.48	0.74	0.016	1.6
1.65	3.86982	0.924115	0.9	70.0109	0.74	0.016	1.6
1.65	3.87208	0.920137	0.85	71.5155	0.74	0.016	1.6
1.65	3.87418	0.916134	0.8	72.9862	0.74	0.016	1.6
1.65	3.86734	0.928044	0.95	68.3969	0.74	0.016	1.4
1.65	3.86975	0.924115	0.9	69.9344	0.74	0.016	1.4
1.65	3.87202	0.920137	0.85	71.4434	0.74	0.016	1.4
1.65	3.87413	0.916134	0.8	72.9198	0.74	0.016	1.4
1.65	3.85753	0.858615	0.7	72.6221	0.72	0.022	1.8
1.65	3.85909	0.855098	0.65	73.7511	0.72	0.022	1.8
1.65	3.86039	0.851173	0.6	74.8307	0.72	0.022	1.8
1.65	3.857	0.858615	0.7	72.0963	0.72	0.022	1.6
1.65	3.85863	0.855098	0.65	73.2726	0.72	0.022	1.6
1.65	3.85998	0.851173	0.6	74.3905	0.72	0.022	1.6
1.65	3.85846	0.855098	0.65	73.0813	0.72	0.022	1.4
1.65	3.85983	0.851173	0.6	74.215	0.72	0.022	1.4
1.65	3.8585	0.895305	0.85	68.6089	0.72	0.02	1.8
1.65	3.86053	0.89167	0.8	69.8964	0.72	0.02	1.8
1.65	3.86248	0.887946	0.75	71.1833	0.72	0.02	1.8
1.65	3.86432	0.884185	0.7	72.4607	0.72	0.02	1.8
1.65	3.86607	0.880392	0.65	73.7256	0.72	0.02	1.8
1.65	3.86771	0.876596	0.6	74.9731	0.72	0.02	1.8
1.65	3.86893	0.872333	0.55	76.0978	0.72	0.02	1.8

continued on next page

Table B.1: *continued*

$M_\odot$	**Log(T_{eff})**	**Log(L/$L_\odot$)**	**Age(Gyrs)**	$\Delta\nu(\mu Hz)$	**X**	**Z**	α
1.65	3.87169	0.864517	0.45	78.4759	0.72	0.02	1.8
1.65	3.87041	0.868548	0.5	77.3078	0.72	0.02	1.8
1.65	3.87298	0.860641	0.4	79.6426	0.72	0.02	1.8
1.65	3.85809	0.89533	0.85	68.2174	0.72	0.02	1.6
1.65	3.86022	0.89167	0.8	69.5744	0.72	0.02	1.6
1.65	3.86223	0.887946	0.75	70.9184	0.72	0.02	1.6
1.65	3.86412	0.884185	0.7	72.2395	0.72	0.02	1.6
1.65	3.8659	0.880392	0.65	73.537	0.72	0.02	1.6
1.65	3.86757	0.876596	0.6	74.8072	0.72	0.02	1.6
1.65	3.8688	0.872333	0.55	75.9447	0.72	0.02	1.6
1.65	3.87029	0.868548	0.5	77.1676	0.72	0.02	1.6
1.65	3.87159	0.864517	0.45	78.3445	0.72	0.02	1.6
1.65	3.87288	0.860641	0.4	79.5188	0.72	0.02	1.6
1.65	3.85794	0.89533	0.85	68.0606	0.72	0.02	1.4
1.65	3.86009	0.89167	0.8	69.4358	0.72	0.02	1.4
1.65	3.86212	0.887946	0.75	70.7929	0.72	0.02	1.4
1.65	3.86402	0.884185	0.7	72.1248	0.72	0.02	1.4
1.65	3.86581	0.880392	0.65	73.43	0.72	0.02	1.4
1.65	3.86748	0.876596	0.6	74.7065	0.72	0.02	1.4
1.65	3.86872	0.872333	0.55	75.8465	0.72	0.02	1.4
1.65	3.87022	0.868548	0.5	77.075	0.72	0.02	1.4
1.65	3.87281	0.860641	0.4	79.4327	0.72	0.02	1.4
1.65	3.87152	0.864517	0.45	78.2553	0.72	0.02	1.4
1.65	3.87007	0.92741	0.8	69.8258	0.72	0.018	1.8
1.65	3.87234	0.923318	0.75	71.3384	0.72	0.018	1.8
1.65	3.87446	0.919198	0.7	72.8226	0.72	0.018	1.8
1.65	3.86997	0.92741	0.8	69.7189	0.72	0.018	1.6
1.65	3.87225	0.923318	0.75	71.2417	0.72	0.018	1.6
1.65	3.87438	0.919198	0.7	72.7338	0.72	0.018	1.6
1.65	3.86991	0.92741	0.8	69.6431	0.72	0.018	1.4
1.65	3.87219	0.923318	0.75	71.1713	0.72	0.018	1.4
1.65	3.87433	0.919198	0.7	72.6679	0.72	0.018	1.4
1.65	3.85819	0.918735	0.85	65.8182	0.7	0.022	1.8
1.65	3.86064	0.915033	0.8	67.2334	0.7	0.022	1.8
1.65	3.86298	0.9113	0.75	68.6429	0.7	0.022	1.8
1.65	3.86446	0.906274	0.7	69.8677	0.7	0.022	1.8
1.65	3.86856	0.89851	0.6	72.6495	0.7	0.022	1.8
1.65	3.86657	0.902398	0.65	71.2674	0.7	0.022	1.8
1.65	3.87044	0.894579	0.55	74.0153	0.7	0.022	1.8
1.65	3.87203	0.89035	0.5	75.3075	0.7	0.022	1.8

continued on next page

Table B.1: *continued*

$M_\odot$	**Log(T_{eff})**	**Log(L/$L_\odot$)**	**Age(Gyrs)**	$\Delta\nu(\mu Hz)$	**X**	**Z**	α
1.65	3.87371	0.886314	0.45	76.6406	0.7	0.022	1.8
1.65	3.85783	0.918735	0.85	65.4753	0.7	0.022	1.6
1.65	3.86037	0.915033	0.8	66.9652	0.7	0.022	1.6
1.65	3.86278	0.9113	0.75	68.4332	0.7	0.022	1.6
1.65	3.86429	0.906274	0.7	69.6819	0.7	0.022	1.6
1.65	3.86642	0.902398	0.65	71.1103	0.7	0.022	1.6
1.65	3.87033	0.894579	0.55	73.8921	0.7	0.022	1.6
1.65	3.86844	0.89851	0.6	72.5128	0.7	0.022	1.6
1.65	3.87193	0.89035	0.5	75.1921	0.7	0.022	1.6
1.65	3.87362	0.886314	0.45	76.5342	0.7	0.022	1.6
1.65	3.86025	0.915033	0.8	66.8418	0.7	0.022	1.4
1.65	3.85768	0.918735	0.85	65.3347	0.7	0.022	1.4
1.65	3.86267	0.9113	0.75	68.3235	0.7	0.022	1.4
1.65	3.86419	0.906274	0.7	69.5776	0.7	0.022	1.4
1.65	3.86836	0.89851	0.6	72.4232	0.7	0.022	1.4
1.65	3.86634	0.902398	0.65	71.0142	0.7	0.022	1.4
1.65	3.87026	0.894579	0.55	73.8067	0.7	0.022	1.4
1.65	3.87187	0.89035	0.5	75.1115	0.7	0.022	1.4
1.65	3.87356	0.886314	0.45	76.4574	0.7	0.022	1.4
1.65	3.87358	0.928031	0.65	71.3719	0.7	0.02	1.8
1.65	3.8735	0.928031	0.65	71.2819	0.7	0.02	1.6
1.65	3.87344	0.928031	0.65	71.2143	0.7	0.02	1.4
1.7	3.87422	0.893294	0.4	76.9724	0.72	0.022	1.4
1.7	3.87133	0.90147	0.5	74.5169	0.72	0.022	1.4
1.7	3.87295	0.897583	0.45	75.7939	0.72	0.022	1.4
1.7	3.86962	0.905362	0.55	73.2113	0.72	0.022	1.4
1.7	3.8678	0.909232	0.6	71.8816	0.72	0.022	1.4
1.7	3.86586	0.913075	0.65	70.5273	0.72	0.022	1.4
1.7	3.8638	0.916886	0.7	69.1476	0.72	0.022	1.4
1.7	3.86161	0.920658	0.75	67.7426	0.72	0.022	1.4
1.7	3.85928	0.924385	0.8	66.3148	0.72	0.022	1.4
1.7	3.87427	0.893294	0.4	77.0461	0.72	0.022	1.6
1.7	3.8714	0.90147	0.5	74.5966	0.72	0.022	1.6
1.7	3.873	0.897583	0.45	75.87	0.72	0.022	1.6
1.7	3.86969	0.905362	0.55	73.2953	0.72	0.022	1.6
1.7	3.86787	0.909232	0.6	71.9716	0.72	0.022	1.6
1.7	3.86594	0.913075	0.65	70.6225	0.72	0.022	1.6
1.7	3.86389	0.916886	0.7	69.2505	0.72	0.022	1.6
1.7	3.86171	0.920658	0.75	67.8562	0.72	0.022	1.6
1.7	3.8594	0.924385	0.8	66.4404	0.72	0.022	1.6

continued on next page

Table B.1: *continued*

$M_\odot$	Log(T_{eff})	Log(L/$L_\odot$)	Age(Gyrs)	$\Delta\nu(\mu Hz)$	X	Z	α
1.7	3.87435	0.893294	0.4	77.1483	0.72	0.022	1.8
1.7	3.8715	0.90147	0.5	74.71	0.72	0.022	1.8
1.7	3.87309	0.897583	0.45	75.9758	0.72	0.022	1.8
1.7	3.8698	0.905362	0.55	73.4184	0.72	0.022	1.8
1.7	3.868	0.909232	0.6	72.1076	0.72	0.022	1.8
1.7	3.86609	0.913075	0.65	70.7766	0.72	0.022	1.8
1.7	3.86193	0.920658	0.75	68.0785	0.72	0.022	1.8
1.7	3.86406	0.916886	0.7	69.4326	0.72	0.022	1.8
1.7	3.85969	0.924385	0.8	66.721	0.72	0.022	1.8
1.7	3.85732	0.928007	0.85	65.3619	0.72	0.022	1.8
1.7	3.87081	0.876273	0.45	77.4638	0.74	0.02	1.4
1.7	3.87206	0.872455	0.4	78.5961	0.74	0.02	1.4
1.7	3.86957	0.880248	0.5	76.3344	0.74	0.02	1.4
1.7	3.86694	0.888114	0.6	74.0574	0.74	0.02	1.4
1.7	3.86813	0.883961	0.55	75.1525	0.74	0.02	1.4
1.7	3.86532	0.891834	0.65	72.827	0.74	0.02	1.4
1.7	3.86359	0.895551	0.7	71.5678	0.74	0.02	1.4
1.7	3.85978	0.902875	0.8	68.9728	0.74	0.02	1.4
1.7	3.86174	0.899232	0.75	70.2833	0.74	0.02	1.4
1.7	3.85769	0.906474	0.85	67.6378	0.74	0.02	1.4
1.7	3.87212	0.872455	0.4	78.6818	0.74	0.02	1.6
1.7	3.87088	0.876273	0.45	77.5526	0.74	0.02	1.6
1.7	3.86965	0.880248	0.5	76.4263	0.74	0.02	1.6
1.7	3.86702	0.888114	0.6	74.1571	0.74	0.02	1.6
1.7	3.86821	0.883961	0.55	75.2498	0.74	0.02	1.6
1.7	3.86541	0.891834	0.65	72.9326	0.74	0.02	1.6
1.7	3.86185	0.899232	0.75	70.4055	0.74	0.02	1.6
1.7	3.86369	0.895551	0.7	71.6808	0.74	0.02	1.6
1.7	3.8599	0.902875	0.8	69.1072	0.74	0.02	1.6
1.7	3.85783	0.906474	0.85	67.7887	0.74	0.02	1.6
1.7	3.87099	0.876273	0.45	77.6848	0.74	0.02	1.8
1.7	3.87222	0.872455	0.4	78.8056	0.74	0.02	1.8
1.7	3.86976	0.880248	0.5	76.5656	0.74	0.02	1.8
1.7	3.86834	0.883961	0.55	75.4013	0.74	0.02	1.8
1.7	3.86716	0.888114	0.6	74.3194	0.74	0.02	1.8
1.7	3.86557	0.891834	0.65	73.1171	0.74	0.02	1.8
1.7	3.86388	0.895551	0.7	71.8951	0.74	0.02	1.8
1.7	3.86209	0.899232	0.75	70.661	0.74	0.02	1.8
1.7	3.8602	0.902875	0.8	69.4141	0.74	0.02	1.8
1.7	3.85821	0.906474	0.85	68.1559	0.74	0.02	1.8

continued on next page

Table B.1: *continued*

$M_{\odot}$	**Log(T_{eff})**	**Log(L/$L_{\odot}$)**	**Age(Gyrs)**	$\Delta\nu(\mu Hz)$	**X**	**Z**	α
1.7	3.86313	0.852096	0.45	76.7749	0.74	0.022	1.4
1.7	3.86192	0.855628	0.5	75.7297	0.74	0.022	1.4
1.7	3.8606	0.859189	0.55	74.637	0.74	0.022	1.4
1.7	3.85931	0.862978	0.6	73.5504	0.74	0.022	1.4
1.7	3.85782	0.866448	0.65	72.4199	0.74	0.022	1.4
1.7	3.86324	0.852096	0.45	76.9168	0.74	0.022	1.6
1.7	3.86205	0.855628	0.5	75.8786	0.74	0.022	1.6
1.7	3.85946	0.862978	0.6	73.7227	0.74	0.022	1.6
1.7	3.86074	0.859189	0.55	74.7964	0.74	0.022	1.6
1.7	3.85798	0.866448	0.65	72.6091	0.74	0.022	1.6
1.7	3.86351	0.852096	0.45	77.2376	0.74	0.022	1.8
1.7	3.86236	0.855628	0.5	76.2322	0.74	0.022	1.8
1.7	3.86109	0.859189	0.55	75.1875	0.74	0.022	1.8
1.7	3.85844	0.866448	0.65	73.08	0.74	0.022	1.8
1.7	3.85986	0.862978	0.6	74.1491	0.74	0.022	1.8
1.75	3.87365	0.903068	0.4	76.4893	0.74	0.022	1.4
1.75	3.87078	0.910972	0.5	74.0836	0.74	0.022	1.4
1.75	3.8722	0.906883	0.45	75.2845	0.74	0.022	1.4
1.75	3.86737	0.918494	0.6	71.5552	0.74	0.022	1.4
1.75	3.86914	0.914748	0.55	72.8352	0.74	0.022	1.4
1.75	3.86408	0.926875	0.7	69.0688	0.74	0.022	1.4
1.75	3.8655	0.922215	0.65	70.2498	0.74	0.022	1.4
1.75	3.87226	0.906883	0.45	75.3618	0.74	0.022	1.6
1.75	3.87371	0.903068	0.4	76.5625	0.74	0.022	1.6
1.75	3.86921	0.914748	0.55	72.9197	0.74	0.022	1.6
1.75	3.87084	0.910972	0.5	74.1629	0.74	0.022	1.6
1.75	3.86558	0.922215	0.65	70.3442	0.74	0.022	1.6
1.75	3.86745	0.918494	0.6	71.6436	0.74	0.022	1.6
1.75	3.86417	0.926875	0.7	69.1673	0.74	0.022	1.6
1.75	3.87235	0.906883	0.45	75.4687	0.74	0.022	1.8
1.75	3.87379	0.903068	0.4	76.6634	0.74	0.022	1.8
1.75	3.86931	0.914748	0.55	73.0422	0.74	0.022	1.8
1.75	3.87094	0.910972	0.5	74.2772	0.74	0.022	1.8
1.75	3.86433	0.926875	0.7	69.3334	0.74	0.022	1.8
1.75	3.86572	0.922215	0.65	70.4959	0.74	0.022	1.8
1.75	3.86757	0.918494	0.6	71.7794	0.74	0.022	1.8

Appendix C

Tables of the Weighted Data Results

The results from the weighted data analysis are presented in Tables C.1, C.2, C.3, and C.4 for the four models with the lowest χ^2_{comp} statistic. Each of the model are identified by number in the table caption while a description of how each model was reduced is described in Section 2.6 and Table 2.3.

Tables C.5, C.6, C.7, C.8, C.9, and C.10 present the average frequency, amplitude and phase for models with the same identified frequencies, but with different weighting parameters. The standard error of the mean for each of the frequencies, amplitudes and phases are denoted as $\overline{\sigma}$. Models are identified by number in the table caption and reduction descriptions may be found in Section 2.6 and Table 2.3.

Table C.1: Weighted model number 14.

ν_n	ν (mHz)	Amp.(mma)	ϕ	$\delta\nu$(mHz)	$\Delta\nu$(mHz)
-	2.61858507	0.070913352	0.910846	0.00094979	
ν_1	2.61953486	0.24294598	0.0675517		
+	2.62054495	0.095604089	0.192343	0.00101009	
					ν_2-ν_1
- -	2.65118266	0.049705656	0.499794	0.00078301	0.03341159
-	2.65196567	0.227132022	0.0337749	0.00098078	
ν_2	2.65294645	0.785205032	0.136531		
+	2.65389001	0.198684201	0.305039	0.00094356	
++	2.65491013	0.036362386	0.295139	0.00102012	
					ν_3-ν_2
-	2.68645653	0.316776759	0.182504	0.00103671	0.03454679
ν_3	2.68749324	0.554052254	0.100974		
+	2.68840557	0.202862201	0.373698	0.00091233	
					ν_4-ν_3
- -	2.71912802	0.050704868	0.24473	0.0009345	0.03343382

continued on next page

Table C.1: *continued*

ν_n	ν (mHz)	Amp.(mma)	ϕ	$\delta\nu$(mHz)	$\Delta\nu$(mHz)
-	2.72006252	0.382050618	0.518275	0.00086454	
ν_4	2.72092706	1.16528474	0.7818		
+	2.72182564	0.411449615	0.0173451	0.00089858	
++	2.7227747	0.095959262	0.204671	0.00094906	
					ν_5-ν_4
-	2.75431902	0.206336308	0.111059	0.00101107	0.03440303
ν_5	2.75533009	0.273609593	0.2087		
+	2.75623487	0.122168294	0.499628	0.00090478	
					ν_6 **(new)**-ν_5
-	2.78801304	0.06013802	0.351141	0.00091362	0.03359657
ν_6**(new)**	2.78892666	0.103978465	0.648353		
+	2.79001282	0.096200533	0.417312	0.00108616	
					ν_6 **(old)**-ν_6 **(new)**
-	2.79059069	0.131995516	0.25712	0.00093511	
ν_6**(old)**	2.7915258	0.210137403	0.42461		0.00259914
+	2.79250869	0.085426427	0.612155	0.00098289	
					ν_7-ν_6 **(old)**
-	2.80563375	0.18459977	0.430217	0.00094644	0.01505439
ν_7	2.80658019	0.129121204	0.486159		
+	2.80739686	0.034644142	0.762129	0.00081667	

Table C.2: Weighted model number 18.

ν_n	ν (mHz)	Amp.(mma)	ϕ	$\delta\nu$(mHz)	$\Delta\nu$(mHz)
-	2.61856429	0.071942551	0.964752	0.0009714	
ν_1	2.61953569	0.229725434	0.06479		
+	2.62053759	0.093576944	0.185547	0.0010019	ν_2-ν_1
					0.03341124
-	2.65197721	0.237377855	0.006794	0.00096972	
ν_2	2.65294693	0.778877511	0.138822		
+	2.65388537	0.194361604	0.316978	0.00093844	ν_3-ν_2
					0.03454832
-	2.68644101	0.326210402	0.208817	0.00105424	
ν_3	2.68749525	0.55849757	0.100642		
+	2.68839972	0.207372074	0.384754	0.00090447	ν_4-ν_3
					0.03343165
-	2.72006234	0.383081687	0.513257	0.00086456	

continued on next page

Table C.2: *continued*

ν_n	ν (mHz)	Amp.(mma)	ϕ	$\delta\nu$(mHz)	$\Delta\nu$(mHz)
ν_4	2.7209269	1.16752688	0.781976		
+	2.72182919	0.421655594	0.014391	0.00090229	ν_5-ν_4
					0.03439753
-	2.75431064	0.208573433	0.117343	0.00101379	
ν_5	2.75532443	0.272340984	0.225663		
+	2.75623806	0.113454944	0.478726	0.00091363	
					ν_6 (new)-ν_5
-	2.78800841	0.051362814	0.372008	0.00092015	0.03360413
ν_6 (new)	2.78892856	0.116984091	0.642873		
+	2.79002184	0.098770964	0.396236	0.00109328	
					ν_6 (old)-ν_6 (new)
-	2.79063517	0.123071617	0.17611	0.00089349	0.0026001
ν_6 (old)	2.79152866	0.213303151	0.423763		
+	2.79251626	0.081582989	0.606488	0.0009876	
					ν_7-ν_6 (old)
-	2.80563794	0.187002768	0.423267	0.00092045	0.01502973
ν_7	2.80655839	0.127268129	0.526702		
+	2.807416	0.028527146	0.740054	0.00085761	

Table C.3: Weighted model number 27.

ν_n	ν (mHz)	Amp.(mma)	ϕ	$\delta\nu$(mHz)	$\Delta\nu$(mHz)
ν_1	2.61952756	0.250389276	0.075044	0.001022	
+	2.62055003	0.097967802	0.188145		ν_2-ν_1
					0.03341767
-	2.65197412	0.236102849	0.010989	0.000971	
ν_2	2.65294523	0.779581638	0.13877		
+	2.65389634	0.198998402	0.293861	0.000951	ν_3-ν_2
					0.03454714
-	2.6864492	0.318197961	0.196758	0.001043	
ν_3	2.68749237	0.554835233	0.105008		
+	2.68840277	0.204518648	0.377414	0.00091	ν_4-ν_3
					0.03343572
-	2.72005924	0.387951466	0.52163	0.000869	
ν_4	2.72092809	1.16502003	0.780566		
+	2.72182907	0.425400013	0.014838	0.000901	ν_5-ν_4
					0.03440585

continued on next page

Table C.3: *continued*

ν_n	ν (mHz)	Amp.(mma)	ϕ	$\delta\nu$(mHz)	$\Delta\nu$(mHz)
-	2.75431424	0.202921595	0.121033	0.00102	
ν_5	2.75533394	0.27371851	0.207484		
+	2.75623869	0.120983186	0.480159	0.000905	ν_6 (new)-ν_5
					0.03360725
ν_6 (new)	2.78894119	0.110023328	0.610227	0.000952	
+	2.78989309	0.089420136	0.629435		
-	2.79062019	0.133141748	0.20376	0.000905	ν_6 (old)-ν_6 (new)
ν_6 (old)	2.79152475	0.206709227	0.420454		0.00258356
+	2.79244265	0.09004229	0.718838	0.000918	
					ν_7-ν_6 (old)
-	2.80563819	0.182137724	0.428567	0.00094	0.0150535
ν_7	2.80657825	0.135530035	0.482141		

Table C.4: Weighted model number 32.

ν_n	ν (mHz)	Amp.(mma)	ϕ	$\delta\nu$(mHz)	$\Delta\nu$(mHz)
-	2.61862362	0.073309533	0.832223	0.00091106	
ν_1	2.61953468	0.239755041	0.069636		
+	2.62048027	0.095932955	0.245718	0.00094559	
++	2.62118363	0.080067584	0.011993	0.00070336	ν_2-ν_1
					0.03341106
–	2.6511999	0.051266074	0.460183	0.00079055	
-	2.65199045	0.229358057	0.990978	0.00095529	
ν_2	2.65294574	0.781589995	0.138796		
+	2.65389168	0.197025132	0.305247	0.00094594	
++	2.65493441	0.039233571	0.275253	0.00104273	ν_3-ν_2
					0.03454477
–	2.68558661	0.082521756	0.099311	0.0008698	
-	2.68645641	0.304507647	0.17997	0.0010341	
ν_3	2.68749051	0.556092148	0.10715		
+	2.68841601	0.201709362	0.351061	0.0009255	ν_4-ν_3
					0.03343682
-	2.72005692	0.378040442	0.523409	0.00087041	
ν_4	2.72092733	1.16704816	0.78134		
+	2.72182519	0.412164347	0.017549	0.00089786	
++	2.72280218	0.09867953	0.143867	0.00097699	ν_5-ν_4

continued on next page

Table C.4: *continued*

ν_n	ν (mHz)	Amp.(mma)	ϕ	$\delta\nu$(mHz)	$\Delta\nu$(mHz)
					0.03441038
-	2.75431941	0.205991964	0.113945	0.0010183	
ν_5	2.75533771	0.270062018	0.19682		
+	2.75623916	0.121934717	0.491413	0.00090145	ν_6 **(new)**-ν_5
					0.03360677
ν_6 **(new)**	2.78894448	0.110591288	0.599474		
+	2.78997949	0.095712189	0.48221	0.00103501	ν_6 **(old)**-ν_6 **(new)**
					0.00258473
-	2.79058457	0.134939722	0.261878	0.00094464	
ν_6 **(old)**	2.79152921	0.212994084	0.416727		
+	2.79247997	0.083587537	0.67673	0.00095076	ν_7-ν_6 **(old)**
					0.01505025
-	2.80563634	0.183135677	0.431134	0.00094312	
ν_7	2.80657946	0.13235342	0.483335		

Table C.5: Average values for weighted reduction models 1 through 11. Also Shown are the standard errors on the average, $\overline{\sigma}$, for each of the frequencies, amplitudes and phases.

ν (mHz)	$\overline{\sigma}_\nu$	Amplitude (mma)	$\overline{\sigma}_{Amp}$	ϕ	$\overline{\sigma}_\phi$
2.61953545	7.900E-07	0.24601249	7.373E-04	0.0633009	1.051E-03
2.62052083	1.070E-06	0.10171523	1.705E-03	0.19650982	1.356E-03
2.65198565	7.500E-07	0.24279207	5.547E-04	0.9961617	1.035E-03
2.65294337	2.400E-07	0.79240263	6.705E-04	0.14624444	4.458E-04
2.65389228	3.400E-07	0.18579648	5.661E-04	0.30279192	5.390E-04
2.68644238	1.140E-06	0.330598	1.029E-03	0.20020376	1.827E-03
2.68749022	3.700E-07	0.56121862	7.310E-04	0.11432059	6.970E-04
2.68841076	8.400E-07	0.21633655	5.988E-04	0.35386428	1.600E-03
2.72006512	2.700E-07	0.4069277	1.241E-03	0.50648844	4.798E-04
2.72092748	8.000E-08	1.14889014	1.484E-03	0.78240085	1.675E-04
2.72182369	5.500E-07	0.43446591	3.040E-04	0.01875269	5.798E-04
2.75431871	6.400E-07	0.21439223	6.065E-04	0.11760015	1.002E-03
2.7553339	5.900E-07	0.27781844	5.303E-04	0.21567683	1.273E-03
2.75623393	1.330E-06	0.11794064	6.995E-04	0.4960227	2.322E-03
2.78893447	4.400E-07	0.12777089	3.318E-04	0.61323953	8.992E-04

Table C.5: *continued*

ν (mHz)	$\overline{\sigma}_\nu$	Amplitude (mma)	$\overline{\sigma}_{Amp}$	ϕ	$\overline{\sigma}_\phi$
2.78996491	2.890E-06	0.09356487	6.730E-04	0.50497055	5.201E-03
2.79062867	1.100E-06	0.13355158	6.760E-04	0.19025911	1.706E-03
2.79156089	1.230E-06	0.20052089	6.845E-04	0.38543555	1.287E-03
2.7921505	2.400E-06	0.07815215	1.272E-03	0.09016077	3.053E-03
2.80562377	7.200E-07	0.19279967	8.135E-04	0.44659683	1.029E-03
2.80656481	6.400E-07	0.12456012	9.508E-04	0.48891917	1.161E-03

Table C.6: Average values for weighted reduction models 12 through 15. Also Shown are the standard errors on the average, $\overline{\sigma}$, for each of the frequencies, amplitudes and phases.

ν (mHz)	$\overline{\sigma}_\nu$	Amplitude (mma)	$\overline{\sigma}_{Amp}$	ϕ	$\overline{\sigma}_\phi$
2.6185801	5.46E-06	0.0715267	0.001161	0.91292524	0.0068766
2.619539	3.92E-06	0.2424247	0.002655	0.06225838	0.006325
2.6205368	9.79E-06	0.0976105	0.001203	0.19342275	0.0057129
2.6511872	6.01E-06	0.0647797	0.012309	0.494468	0.007732
2.6519675	1.86E-06	0.226293	0.0012	0.03131885	0.0015268
2.6529458	5.2E-07	0.7874028	0.002408	0.13963825	0.0025338
2.653890	6.7E-07	0.1903922	0.008158	0.30810699	0.0033934
2.6549232	8.68E-06	0.0481614	0.008691	0.28563949	0.0040056
2.6864514	6.72E-06	0.3262788	0.006929	0.187787	0.0091915
2.6874924	1.34E-06	0.5533767	0.001739	0.10520358	0.0040416
2.6884134	6.67E-06	0.2080756	0.003902	0.35549724	0.0135296
2.719132	3.29E-06	0.050237	0.001858	0.20023625	0.0308297
2.7200642	1.49E-06	0.390004	0.006373	0.51269579	0.0043499
2.7209268	4.1E-07	1.156417	0.007015	0.78290647	0.0009107
2.7218266	5.4E-07	0.4154691	0.003349	0.01652785	0.0004565
2.7227788	5.79E-06	0.0916642	0.003555	0.19412225	0.015008
2.7543182	2.23E-06	0.2086525	0.002428	0.1121475	0.0025403
2.7553289	2.6E-06	0.2761036	0.001343	0.21627975	0.0083184
2.7562337	1.61E-06	0.120785	0.001266	0.50185174	0.0029707
2.788000	1.24E-05	0.0534726	0.004968	0.3860465	0.029895
2.7889254	1.37E-06	0.1096075	0.005586	0.64184302	0.0052977
2.7900126	2.77E-06	0.0961226	0.001073	0.42164949	0.0084355
2.7905953	5.41E-06	0.1327671	0.001003	0.25295049	0.0077471
2.7915325	7.71E-06	0.2017605	0.006026	0.41866401	0.0086059
2.7925239	1.52E-05	0.0771367	0.007067	0.58520973	0.0246078

Table C.6: *continued*

ν (mHz)	$\overline{\sigma}_\nu$	Amplitude (mma)	$\overline{\sigma}_{Amp}$	ϕ	$\overline{\sigma}_\phi$
2.8056314	3.1E-06	0.1854348	0.001802	0.43582401	0.0061031
2.8065777	3.34E-06	0.1242794	0.003883	0.48549101	0.0051416
2.807390	1.03E-05	0.0377643	0.002778	0.77594125	0.0130536

Table C.7: Average values for weighted reduction models 16 through 19. Also Shown are the standard errors on the average, $\overline{\sigma}$, for each of the frequencies, amplitudes and phases.

ν (mHz)	$\overline{\sigma}_\nu$	Amplitude (mma)	$\overline{\sigma}_{Amp}$	ϕ	$\overline{\sigma}_\phi$
2.61856365	2.610E-06	0.07097502	1.044E-03	0.95333153	4.762E-03
2.61953688	3.200E-06	0.2359844	2.497E-03	0.06417342	4.773E-03
2.62054586	3.710E-06	0.0981698	1.705E-03	0.17652375	3.844E-03
2.65197802	2.260E-06	0.23576348	1.570E-03	0.00600668	2.442E-03
2.65294647	5.800E-07	0.78556252	3.354E-03	0.13977875	2.047E-03
2.65388799	9.100E-07	0.19226289	3.603E-03	0.31249276	1.947E-03
2.68644285	4.650E-06	0.32979065	5.685E-03	0.20419475	6.233E-03
2.68749428	9.300E-07	0.55675828	1.288E-03	0.10356157	3.047E-03
2.68840957	8.020E-06	0.20968853	3.247E-03	0.36267751	1.678E-02
2.72006321	1.410E-06	0.39359266	6.682E-03	0.51109952	3.760E-03
2.720927	3.000E-07	1.15567088	7.099E-03	0.78218025	7.558E-04
2.72182894	3.500E-07	0.42885065	4.093E-03	0.0144197	5.332E-04
2.75431371	1.730E-06	0.21081457	2.863E-03	0.11894425	2.114E-03
2.75532389	2.540E-06	0.27500349	2.543E-03	0.22870174	7.207E-03
2.75623894	5.500E-07	0.11634202	1.571E-03	0.48223901	1.813E-03
2.78798771	1.421E-05	0.05151148	2.720E-03	0.41204751	2.952E-02
2.78892875	1.030E-06	0.11496046	3.801E-03	0.63687551	4.427E-03
2.79001665	3.120E-06	0.09732255	1.377E-03	0.40953773	8.861E-03
2.79062533	4.330E-06	0.12959906	2.632E-03	0.19501725	7.734E-03
2.79153204	6.010E-06	0.20236254	6.278E-03	0.42214176	5.745E-03
2.79252291	1.587E-05	0.07779086	6.570E-03	0.58961576	2.539E-02
2.80563474	2.750E-06	0.18785006	1.122E-03	0.42921099	5.395E-03
2.80656528	3.320E-06	0.1226374	3.468E-03	0.50999427	7.254E-03
2.80740094	7.880E-06	0.03561373	3.603E-03	0.765073	1.064E-02

Table C.8: Average values for weighted reduction models 21 through 24. Also Shown are the standard errors on the average, $\overline{\sigma}$, for each of the frequencies, amplitudes and phases.

ν (mHz)	$\overline{\sigma}_\nu$	Amplitude (mma)	$\overline{\sigma}_{Amp}$	ϕ	$\overline{\sigma}_\phi$
2.61856	3.32E-06	0.071109	0.000871	0.952817	0.003281
2.619539	2.51E-06	0.236962	0.001243	0.061373	0.004041
2.620543	3.93E-06	0.100365	0.000319	0.178258	0.000697
2.651981	1.83E-06	0.23488	0.001981	0.502181	0.287136
2.652946	3.1E-07	0.790163	0.003414	0.14174	0.001667
2.653889	3.4E-07	0.189002	0.003843	0.310469	0.002024
2.686444	3.6E-06	0.330803	0.004905	0.200294	0.004694
2.687494	6.9E-07	0.557191	0.001435	0.105834	0.002632
2.688414	5.52E-06	0.211807	0.002841	0.351072	0.011941
2.720066	7.3E-07	0.399857	0.005238	0.505701	0.002535
2.720927	4E-07	1.148638	0.005753	0.782802	0.000868
2.721828	3.6E-07	0.434166	0.003309	0.016203	0.00082
2.754317	1.19E-06	0.213565	0.002504	0.119555	0.001758
2.755326	2.17E-06	0.277703	0.001866	0.225756	0.006226
2.756234	1.59E-06	0.119914	0.001552	0.495347	0.000796
2.787999	1.22E-05	0.05118	0.004149	0.379469	0.026376
2.788923	1.42E-06	0.115093	0.003382	0.649199	0.007537
2.789982	4.66E-06	0.097075	0.001393	0.48186	0.008765
2.790619	2.82E-06	0.131418	0.001352	0.20935	0.004125
2.791539	5.39E-06	0.202949	0.005398	0.421275	0.006661
2.805624	1.49E-06	0.19008	0.002272	0.447171	0.003409
2.806567	2.06E-06	0.118159	0.004019	0.50231	0.005409
2.807406	1.43E-05	0.034288	0.003765	0.740786	0.026875

Table C.9: Average values for weighted reduction models 25 through 28. Also Shown are the standard errors on the average, $\overline{\sigma}$, for each of the frequencies, amplitudes and phases.

ν (mHz)	$\overline{\sigma}_\nu$	Amplitude (mma)	$\overline{\sigma}_{Amp}$	ϕ	$\overline{\sigma}_\phi$
2.619531	4.11E-06	0.249794	0.002486	0.070423	0.005858
2.620545	5.16E-06	0.099087	0.001556	0.184552	0.001297
2.651977	2.73E-06	0.23728	0.002204	0.007028	0.002996

Table C.9: *continued*

ν (mHz)	$\overline{\sigma}_\nu$	Amplitude (mma)	$\overline{\sigma}_{Amp}$	ϕ	$\overline{\sigma}_\phi$
2.652945	5.7E-07	0.78296	0.00294	0.141938	0.002486
2.653896	1.24E-06	0.1935	0.005232	0.295626	0.003961
2.686445	6.26E-06	0.325477	0.006056	0.200329	0.008523
2.687492	9.6E-07	0.554609	0.001527	0.108359	0.003112
2.688411	7.1E-06	0.209002	0.004507	0.357545	0.014579
2.720061	1.39E-06	0.396077	0.005775	0.516621	0.003966
2.720928	3.8E-07	1.156686	0.006538	0.781549	0.000724
2.721829	6E-07	0.428799	0.003657	0.014375	0.000309
2.754314	1.04E-06	0.206781	0.003963	0.120556	0.000893
2.75533	4.96E-06	0.276679	0.001751	0.218244	0.011929
2.756242	1.27E-06	0.118345	0.002162	0.477665	0.001553
2.788937	5.03E-06	0.115846	0.006419	0.615988	0.007687
2.78995	2.91E-05	0.091216	0.001361	0.530571	0.051962
2.790627	4.29E-06	0.13455	0.001285	0.193457	0.00707
2.79153	6.63E-06	0.201207	0.004239	0.417806	0.005454
2.792489	2.34E-05	0.07973	0.008848	0.64849	0.035226
2.805636	3.07E-06	0.183588	0.001291	0.42937	0.003845
2.806574	4.47E-06	0.129968	0.003565	0.487405	0.00602

Table C.10: Average values for weighted reduction models 30 through 32. Also Shown are the standard errors on the average, $\overline{\sigma}$, for each of the frequencies, amplitudes and phases.

ν (mHz)	$\overline{\sigma}_\nu$	Amplitude (mma)	$\overline{\sigma}_{Amp}$	ϕ	$\overline{\sigma}_\phi$
2.618615	4.53E-06	0.072739	0.000822	0.842523	0.007433
2.619542	3.75E-06	0.237434	0.001716	0.057926	0.005873
2.620466	7.51E-06	0.096504	0.000338	0.259676	0.007361
2.621176	3.76E-06	0.089528	0.004765	0.021728	0.00491
2.651208	3.9E-06	0.074912	0.012117	0.448473	0.006704
2.651994	1.71E-06	0.229328	0.000249	0.988625	0.001177
2.652945	4.1E-07	0.785146	0.003256	0.142981	0.0021
2.653892	2.8E-07	0.185178	0.006099	0.308044	0.001411
2.654934	1.94E-06	0.057818	0.009549	0.296519	0.0109
2.685572	7.32E-06	0.083156	0.002637	0.107762	0.005915
2.686444	6.4E-06	0.321998	0.008771	0.195068	0.00815
2.687489	9.7E-07	0.557244	0.001609	0.113338	0.00335
2.68843	6.9E-06	0.212632	0.005463	0.321584	0.015154

Table C.10: *continued*

ν (mHz)	$\overline{\sigma}_\nu$	Amplitude (mma)	$\overline{\sigma}_{Amp}$	ϕ	$\overline{\sigma}_\phi$
2.72006	1.62E-06	0.390504	0.006558	0.515212	0.004099
2.720927	4.2E-07	1.153283	0.007155	0.783116	0.000936
2.721827	9.2E-07	0.417881	0.003188	0.015499	0.001042
2.722815	6.16E-06	0.091935	0.003758	0.114753	0.014753
2.754318	8.5E-07	0.211407	0.003885	0.114906	0.001496
2.755333	2.55E-06	0.27421	0.002233	0.212606	0.008042
2.756236	1.83E-06	0.120356	0.001713	0.498439	0.003515
2.788935	4.66E-06	0.120502	0.004973	0.612645	0.006893
2.789984	4.04E-06	0.096761	0.001691	0.471863	0.011191
2.790598	6.85E-06	0.133643	0.001462	0.246016	0.008433
2.791538	4.43E-06	0.202389	0.006484	0.410531	0.003102
2.792518	1.99E-05	0.069908	0.008051	0.61472	0.032057
2.805631	2.67E-06	0.185083	0.001732	0.438911	0.004142
2.806572	3.75E-06	0.124083	0.004466	0.487065	0.004595